

# Orthogonal vs. Biorthogonal Wavelets for Image Compression

Satyabrata Rout

Thesis submitted to the Faculty of the  
Virginia Polytechnic Institute and State University  
(Virginia Tech)  
in partial fulfillment of the requirements for the degree of

Master of Science  
in  
Electrical Engineering

Dr. A. E. Bell, Chair

Dr. A. L. Abbott

Dr. B. D. Woerner

August 21, 2003  
Blacksburg, Virginia

**KEYWORDS:** Image compression, Wavelets, Symmetric extension, Periodic extension, DWT, Orthogonal wavelets, Biorthogonal wavelets.

Copyright 2003, Satyabrata Rout

# Orthogonal vs. Biorthogonal Wavelets for Image Compression

Satyabrata Rout

(ABSTRACT)

Effective image compression requires a non-expansive discrete wavelet transform (DWT) be employed; consequently, image border extension is a critical issue. Ideally, the image border extension method should not introduce distortion under compression. It has been shown in literature that symmetric extension performs better than periodic extension. However, the non-expansive, symmetric extension using fast Fourier transform and circular convolution DWT methods require symmetric filters. This precludes orthogonal wavelets for image compression since they cannot simultaneously possess the desirable properties of orthogonality and symmetry. Thus, biorthogonal wavelets have been the de facto standard for image compression applications. The viability of symmetric extension with biorthogonal wavelets is the primary reason cited for their superior performance.

Recent matrix-based techniques for computing a non-expansive DWT have suggested the possibility of implementing symmetric extension with orthogonal wavelets. For the first time, this thesis analyzes and compares orthogonal and biorthogonal wavelets with symmetric extension.

Our results indicate a significant performance improvement for orthogonal wavelets when they employ symmetric extension. Furthermore, our analysis also identifies that linear (or near-linear) phase filters are critical to compression performance—an issue that has not been recognized to date.

We also demonstrate that biorthogonal and orthogonal wavelets generate similar compression performance when they have similar filter properties and both employ symmetric extension. The biorthogonal wavelets indicate a slight performance advantage for low frequency images; however, this advantage is significantly smaller than recently published results and is explained in terms of wavelet properties not previously considered.

# Acknowledgments

I express my sincere gratitude to my advisor Dr. Amy Bell for her technical and financial support which made this thesis possible. Her constant encouragement, suggestions and ideas have been invaluable to this work. I immensely appreciate the time she devoted reviewing my writing and vastly improving my technical writing skills. Her thoroughness, discipline and work ethic are laudable and worthy of emulation.

I would like to thank Dr. Brian Woerner and Dr. Lynn Abbott for reviewing my work and agreeing to serve on my committee. I am also grateful to Dr. Karen Duca in VBI for her financial support and the opportunity to work on some interesting biomedical signal processing problems.

I am thankful to my fellow DSPCL colleagues Kishore Kotteri and Krishnaraj Varma for their technical help and insightful suggestions that went a long way in shaping this thesis. My interactions with them greatly improved my technical knowledge and research skills. I am also grateful to my friends Ajit, Sajid, Venkat, Gautam and Savyasachi for making my stay at Virginia Tech, a memorable one.

Lastly, I shall always be indebted to my family for their unconditional love, support and trust on my judgments during good and bad times. The dedication and sacrifices by my parents to provide the best of educational opportunities to me, my brother and sisters have been extraordinary. They imbued in us the importance of education, hard work and perseverance in attaining one's goals.

# Contents

<b>1</b>	<b>Introduction</b>	<b>1</b>
1.1	Motivation . . . . .	1
1.2	Previous work . . . . .	3
1.3	Significance of this work . . . . .	5
1.4	Organization of this thesis . . . . .	6
<b>2</b>	<b>Background</b>	<b>7</b>
2.1	Overview of wavelet based image compression system . . . . .	7
2.2	One and two dimensional discrete wavelet transform . . . . .	8
2.2.1	Perfect reconstruction filter bank . . . . .	8
2.2.2	One dimensional discrete wavelet transform . . . . .	10
2.2.3	Fast wavelet transform . . . . .	11
2.2.4	Two dimensional discrete wavelet transform . . . . .	12
2.2.5	Wavelet decomposition structure . . . . .	14
2.3	Extension techniques . . . . .	16
2.3.1	Expansive and non-expansive discrete wavelet transform . . . . .	16
2.3.2	Periodic extension . . . . .	18

2.3.3	Symmetric extension . . . . .	22
2.4	DWT implementation methods . . . . .	26
2.4.1	Fast fourier transform method . . . . .	26
2.4.2	Time domain convolution method . . . . .	28
2.4.3	Time domain matrix method . . . . .	34
2.4.4	Comparison of FFT, TDC and TDM methods . . . . .	39
2.5	Quantization . . . . .	41
2.5.1	SPIHT coder . . . . .	41
<b>3</b>	<b>Wavelet properties</b>	<b>44</b>
3.1	Orthonormality . . . . .	44
3.2	Filter length . . . . .	45
3.3	Vanishing order, smoothness and magnitude response . . . . .	46
3.3.1	Vanishing order . . . . .	46
3.3.2	Smoothness . . . . .	47
3.3.3	Magnitude response . . . . .	49
3.4	Group delay difference . . . . .	52
<b>4</b>	<b>Performance analysis and results</b>	<b>55</b>
4.1	Choice of wavelets and images . . . . .	56
4.2	Test conditions . . . . .	56
4.3	PSNR results . . . . .	57
4.3.1	Results for periodic extension . . . . .	57
4.3.1.1	Low frequency images . . . . .	58
4.3.1.2	Medium frequency images . . . . .	59

4.3.1.3	High frequency images . . . . .	59
4.3.2	Results for symmetric extension . . . . .	59
4.3.2.1	Low frequency images . . . . .	60
4.3.2.2	Medium frequency images . . . . .	60
4.3.2.3	High frequency images . . . . .	60
4.4	Analysis of PSNR results . . . . .	61
4.4.1	Least asymmetric wavelets vs. asymmetric wavelets . . . . .	61
4.4.2	Periodic extension vs. symmetric extension . . . . .	65
4.4.3	Orthogonal vs. biorthogonal . . . . .	72
4.5	Subjective results and analysis . . . . .	75
4.5.1	Periodic extension . . . . .	75
4.5.2	Symmetric extension . . . . .	76
<b>5</b>	<b>Conclusions and future work</b>	<b>78</b>
5.1	Conclusions . . . . .	78
5.2	Future work . . . . .	79
<b>A</b>	<b>Periodic extension results</b>	<b>85</b>
<b>B</b>	<b>Symmetric extension results</b>	<b>92</b>
<b>C</b>	<b>Subjective results for periodic extension</b>	<b>96</b>
<b>D</b>	<b>Subjective results for symmetric extension</b>	<b>103</b>
<b>E</b>	<b>Test images</b>	<b>107</b>

# List of Figures

2.1	Block diagram of a wavelet based lossy compression system. . . . .	8
2.2	1-D, 1 level PR filter bank . . . . .	9
2.3	One level filter bank for computation of 2-D DWT. . . . .	12
2.4	Output of 1-level 2-D decomposition . . . . .	14
2.5	3-level 2-D decomposition . . . . .	15
2.6	2-Level wavelet decomposition of <i>Lighthouse</i> image . . . . .	16
2.7	Illustration of expansive DWT transform . . . . .	17
2.8	Block diagram for periodic extension . . . . .	19
2.9	Periodic extension example. . . . .	21
2.10	Block diagram for symmetric extension . . . . .	24
2.11	Symmetric extension example. . . . .	25
2.12	Block diagram of the FFT method with periodic extension . . . . .	27
2.13	Block diagram of the FFT method with symmetric extension . . . . .	28
2.14	Block diagram of TDC method with periodic extension . . . . .	29
2.15	TDC method periodic extension example. . . . .	30
2.16	Block diagram of TDC method with symmetric extension . . . . .	32
2.17	TDC method symmetric extension example. . . . .	33

2.18	TDM method symmetric extension example. . . . .	37
2.19	Block diagram of TDM method with symmetric extension . . . . .	38
2.20	Block diagram of TDM method with periodic extension . . . . .	39
2.21	Parent-child relationships for a 3-level wavelet decomposition. . . . .	42
3.1	Scaling Function, $\phi(t)$ , $D_{4LA}$ , $VO = 4$ , $S_{max} = 1.77$ . . . . .	48
3.2	Wavelet Function, $\psi(t)$ , $D_{4LA}$ , $VO = 4$ , $S_{max} = 1.77$ . . . . .	48
3.3	Scaling Function, $\phi(t)$ , $D_{10LA}$ , $VO = 10$ , $S_{max} = 3.40$ . . . . .	48
3.4	Wavelet Function, $\psi(t)$ , $D_{10LA}$ , $VO = 10$ , $S_{max} = 3.40$ . . . . .	48
3.5	Magnitude response of $D_{10LA}$ vs. $D_{4LA}$ . . . . .	50
3.6	Magnitude response of $D_{9/7}$ vs. $D_{5LA}$ . . . . .	51
3.7	Magnitude response of $D_{22/14}$ vs. $D_{9LA}$ . . . . .	51
3.8	Original Image . . . . .	53
3.9	1-level, 2D DWT of original image using $D_{9LA}$ . . . . .	53
3.10	1-level, 2D DWT of original image using $D_A$ . . . . .	53
3.11	1-level, 2D DWT of original image using $B_{22/14}$ . . . . .	53
3.12	Group delay plot for $D_{9LA}$ & $D_{9A}$ LP filters. . . . .	54
3.13	Group delay plot for $D_{9LA}$ & $D_{9A}$ HP filters. . . . .	54
4.1	Original image <i>House256</i> . . . . .	66
4.2	<i>House256</i> , Symmetric extension, 32:1, PSNR = 27.37 dB. . . . .	66
4.3	<i>House256</i> , Periodic extension, 32:1, PSNR = 26.89 dB. . . . .	66
4.4	Mean-squared-error (MSE) plots: periodic vs. symmetric extension. . . . .	70
4.5	MSE plots no. 2: periodic vs. symmetric extension. . . . .	71
4.6	MSE plots: orthogonal vs. biorthogonal wavelets. . . . .	74

C.1	Original image <i>Lena</i> . . . . .	97
C.2	<i>Lena</i> , Periodic extension, $D_{4A}$ , 32:1, PSNR = 32.77 dB. . . . .	97
C.3	<i>Lena</i> , Periodic extension, $D_{4LA}$ , 32:1, PSNR = 32.81 dB. . . . .	97
C.4	<i>Lena</i> , Periodic extension, $D_{10A}$ , 32:1, PSNR = 32.72 dB. . . . .	98
C.5	<i>Lena</i> , Periodic extension, $D_{10LA}$ , 32:1, PSNR = 33.16 dB. . . . .	98
C.6	<i>Lena</i> , Periodic extension, $B_{9/7}$ , 32:1, PSNR = 33.27 dB. . . . .	98
C.7	<i>Lena</i> , Periodic extension, $B_{22/14}$ , 32:1, PSNR = 33.37 dB. . . . .	98
C.8	Original image, <i>Lighthouse</i> . . . . .	99
C.9	<i>Lighthouse</i> , Periodic extension, $D_{4A}$ , 32:1, PSNR = 26.62 dB. . . . .	99
C.10	<i>Lighthouse</i> , Periodic extension, $D_{4LA}$ , 32:1, PSNR = 26.62 dB. . . . .	99
C.11	<i>Lighthouse</i> , Periodic extension, $D_{10A}$ , 32:1, PSNR = 26.34 dB. . . . .	100
C.12	<i>Lighthouse</i> , Periodic extension, $D_{10LA}$ , 32:1, PSNR = 26.62 dB. . . . .	100
C.13	<i>Lighthouse</i> , Periodic extension, $B_{9/7}$ , 32:1, PSNR = 26.64 dB. . . . .	100
C.14	<i>Lighthouse</i> , Periodic extension, $B_{22/14}$ , 32:1, PSNR = 26.68 dB. . . . .	100
C.15	Original image, <i>Mandrill</i> . . . . .	101
C.16	<i>Mandrill</i> , Periodic extension, $D_{4A}$ , 32:1, PSNR = 22.69 dB. . . . .	101
C.17	<i>Mandrill</i> , Periodic extension, $D_{4LA}$ , 32:1, PSNR = 22.70 dB. . . . .	101
C.18	<i>Mandrill</i> , Periodic extension, $D_{10A}$ , 32:1, PSNR = 22.66 dB. . . . .	102
C.19	<i>Mandrill</i> , Periodic extension, $D_{10LA}$ , 32:1, PSNR = 22.80 dB. . . . .	102
C.20	<i>Mandrill</i> , Periodic extension, $B_{9/7}$ , 32:1, PSNR = 22.77 dB. . . . .	102
C.21	<i>Mandrill</i> , Periodic extension, $B_{22/14}$ , 32:1, PSNR = 22.86 dB. . . . .	102
D.1	<i>Lena</i> , Symmetric extension, $D_{5LA}$ , 64:1, PSNR = 30.54 dB. . . . .	104
D.2	<i>Lena</i> , Symmetric extension, $B_{9/7}$ , 64:1, PSNR = 30.47 dB. . . . .	104

D.3	<i>Lena</i> , Symmetric extension, $D_{9LA}$ , 64:1, PSNR = 30.60 dB. . . . .	104
D.4	<i>Lena</i> , Symmetric extension, $B_{22/14}$ , 64:1, PSNR = 30.81 dB. . . . .	104
D.5	<i>Barbara</i> , Symmetric extension, $D_{5LA}$ , 64:1, PSNR = 24.29 dB. . . . .	105
D.6	<i>Barbara</i> , Symmetric extension, $B_{9/7}$ , 64:1, PSNR = 24.30 dB. . . . .	105
D.7	<i>Barbara</i> , Symmetric extension, $D_{9LA}$ , 64:1, PSNR = 24.27 dB. . . . .	105
D.8	<i>Barbara</i> , Symmetric extension, $B_{22/14}$ , 64:1, PSNR = 24.29 dB. . . . .	105
D.9	<i>SanDiego</i> , Symmetric extension, $D_{5LA}$ , 32:1, PSNR = 21.55 dB. . . . .	106
D.10	<i>SanDiego</i> , Symmetric extension, $B_{9/7}$ , 32:1, PSNR = 21.56 dB. . . . .	106
D.11	<i>SanDiego</i> , Symmetric extension, $B_{9/7}$ , 32:1, PSNR = 21.64 dB. . . . .	106
D.12	<i>SanDiego</i> , Symmetric extension, $B_{22/14}$ , 32:1, PSNR = 21.64 dB. . . . .	106
E.1	<i>Lena</i> . . . . .	108
E.2	<i>Peppers</i> . . . . .	108
E.3	<i>Boat</i> . . . . .	108
E.4	<i>Goldhill</i> . . . . .	108
E.5	<i>Barbara</i> . . . . .	109
E.6	<i>Lighthouse</i> . . . . .	109
E.7	<i>House</i> . . . . .	109
E.8	<i>Nitf7</i> . . . . .	109
E.9	<i>Satellite</i> . . . . .	110
E.10	<i>Mandrill</i> . . . . .	110
E.11	<i>Grass</i> . . . . .	110
E.12	<i>SanDiego</i> . . . . .	110

# List of Tables

2.1	DWT based on linear convolution . . . . .	17
2.2	Condition numbers for LA $\perp$ , bi $\perp$ and A $\perp$ filters. . . . .	41
3.1	Comparison of wavelet properties. . . . .	46
4.1	Energy distribution table for compared images. . . . .	57
4.2	SPIHT MSE for different CRs using a test image. . . . .	58
4.3	PSNR difference: LA $\perp$ vs. A $\perp$ wavelet. . . . .	63
4.4	SPIHT MSE Comparison . . . . .	64
4.5	PSNR improvement: bi $\perp$ over $\perp$ wavelets. . . . .	67
4.6	Energy distribution for lowest frequency subband after a 5-level decomposition. . . . .	68
4.7	Wavelet properties: biorthogonal vs. orthogonal. . . . .	73
4.8	PSNR improvement: bi $\perp$ over corresponding LA $\perp$ wavelet. . . . .	73
A.1	Periodic extension PSNR values for LF images: <i>Lena</i> and <i>Peppers</i> . . . . .	86
A.2	Periodic extension PSNR values for LF images: <i>Boat</i> and <i>Goldhill</i> . . . . .	87
A.3	Periodic extension PSNR values for MF images: <i>Barbara</i> and <i>Lighthouse</i> . . . . .	88
A.4	Periodic extension PSNR values for MF images: <i>House</i> and <i>Nitf7</i> . . . . .	89
A.5	Periodic extension PSNR values for HF images: <i>Satellite</i> and <i>Mandrill</i> . . . . .	90

A.6	Periodic extension PSNR values for HF images: <i>Grass</i> and <i>SanDiego</i> . . . . .	91
B.1	Symmetric extension PSNR values for LF images. . . . .	93
B.2	Symmetric extension PSNR values for MF images. . . . .	94
B.3	Symmetric extension PSNR values for HF images. . . . .	95

# Chapter 1

## Introduction

### 1.1 Motivation

The phenomenal growth of the Internet, along with the ubiquitous use of digital cameras, scanners and camera phones have made the capture, display, storage and transmission of images, a routine experience. In addition, imaging is extensively used in medicine, law enforcement, Internet gaming and data collected by satellites. Despite rapid improvements in data storage, processing speeds, and digital communication system performance, this proliferation of digital media often outstrips the amount of data storage and transmission capacities. Thus, the compression of such signals has assumed great importance in the use, storage and transmission of digital images.

For still images, the JPEG and the GIF standards have been the prevailing norms for lossy and lossless compression [21]. Lossless compression achieves a moderate amount of compression (3:1 - 4:1) whereas lossy compression schemes exploit the human visual system to achieve higher compression ratios (*leq* 0.25 bits per pixel (bpp)). Recently, wavelet-based lossy compression schemes have been gaining popularity over discrete cosine transform (DCT) due to their lower complexity and better image quality vis-a-vis compression ratio. This prompted

the new JPEG2000 standard to adopt a wavelet-based compression scheme.

For image compression applications, it is vital that a non-expansive (i.e. the total number of input samples is equal to the total number of wavelet coefficients at any point during the decomposition process) discrete wavelet transform (DWT) be employed; this, in turn, makes image border extension critical. The goal of the extension technique is two-fold: (1) no distortion should be introduced by the extension technique; and, (2) the subband decomposition process should be non-expansive. There are two types of extension techniques that are widely used in image compression: periodic and symmetric extension. Both extension techniques meet the second goal. However, only symmetric extension satisfies the first goal. Periodic extension may introduce discontinuities at the image boundaries that generate spurious high frequencies during the decomposition process.

It has been also shown that biorthogonal wavelets outperform orthogonal wavelets [12, 13]. This is because time domain convolution (TDC) or fast Fourier transform (FFT) based non-expansive DWT methods require symmetric filters to implement symmetric extension. Hence, this excludes the implementation of symmetric extension with orthogonal wavelets that do not have symmetric filters. However, it is possible to implement symmetric extension with orthogonal wavelets using recently developed matrix based DWT implementation methods. Thus, the question remains whether biorthogonal wavelets outperform orthogonal wavelets in image compression applications due to the use of symmetric extension or due to the linear phase property of the symmetric biorthogonal filters. If orthogonal wavelets were able to employ symmetric extension, then perhaps their unique advantages (energy preserving, decorrelating, simple inverse) would outweigh advantages of the biorthogonal wavelets (linear phase).

For the first time, orthogonal wavelets would be able to compete with the biorthogonal wavelets an equal footing with regard to the type of border extension. Thus, some unresolved questions may now be addressed. This thesis presents and compares different DWT implementation techniques as well as compares the performance of orthogonal and biorthog-

onal wavelets with symmetric extension.

## 1.2 Previous work

An early introduction to wavelet theory was presented by Ingrid Daubechies with the construction of compactly supported orthogonal wavelets [3]. Subsequently, the development of multiresolution analysis and the fast wavelet transform by Mallat led to extensive research in image coding using wavelets [14]. The success of wavelet-based image coding can be evidenced by JPEG2000’s adoption of the biorthogonal (9,7) wavelet for image compression.

Discontinuity at the boundaries for finite length signals (images) generates undesirable artifacts under compression. Hence, signal extension is performed at the boundaries to overcome this finite signal length problem. Smith and Eddins first demonstrated the advantages of symmetric extension over periodic extension [23]. They illustrated that the symmetric extension technique outperforms the periodic extension in terms of both PSNR and image quality; their result comparing the symmetric and periodic extension technique for the *building* image (with dissimilar borders) shows an improvement of 0.4 - 0.5 dB for compression ratios from 0.4 bpp - 1.6 bpp. Their symmetric extension method was further developed to include all combinations of filter lengths and symmetry types [2, 9, 17]. However, their DFT based symmetric extension method—which requires symmetric filters to produce symmetric subbands—precludes the use of orthogonal wavelets. Consequently, it has been widely accepted that symmetric extension cannot be employed with orthogonal wavelets in the implementation of a non-expansive DWT [13, 23]. Additionally, the available results has been limited to a very few images.

Extensive studies have been done comparing the performance of scalar wavelets for image compression. It has been shown that biorthogonal wavelets outperform orthogonal wavelets both subjectively and quantitatively in terms of PSNR [12, 13]. These results show that the PSNR advantage of the biorthogonal wavelet  $B_{9/7}$  over the orthogonal  $D_{8A}$  wavelet ranged

from about 0.6dB at 8:1 to 0.4dB at 64:1 for a low frequency image (*Lena*). The authors explained the performance differences between biorthogonal and orthogonal wavelets in terms of several wavelet properties—with coding gain cited as the primary factor; unfortunately, many results did not fit easily into this explanation. The attribute most often cited as the primary explanation for orthogonal wavelet’s poor performance is the absence of the superior symmetric image border extension technique for non-symmetric filters. The inability of scalar wavelets to combine orthogonality and symmetry motivated the development of balanced multiwavelets [11]. Unfortunately, the performance of balanced multiwavelets also falls short of the biorthogonal scalar wavelets in compression [10, 18].

While the symmetric extension details were being perfected for the biorthogonal wavelets, matrix methods were developed as an alternative for computing the non-expansive DWT [4, 1, 22]. The time domain matrix (TDM) method introduced by Silva and Sa works for both biorthogonal and orthogonal wavelets irrespective of the extension type. The matrix based methods regenerate the expansive transform coefficients (truncated during decomposition process) from the transmitted non-expansive coefficients. Subsequently, inverse DWT is computed using this extended signal.

Approximation order, regularity, smoothness, orthonormality and magnitude response of the filters have been identified as some of the wavelet properties important for image compression. Approximation power of the wavelet corresponds to the vanishing moment of the wavelet [24, 25]. An asymptotic error formula for the approximation error is presented in [26]. Sobolev and Holder definitions of regularity that quantify the degree of smoothness are given in [16]. Villasenor et.al proposed a way to measure the accuracy of reconstruction by evaluating the impulse and step response of the filter associated with the low frequency subband [5]. Orthonormal filters preserve energy in the transform domain. The orthonormality parameter measures the deviation of biorthogonal wavelets from orthonormality [13]. However, the published literature to date have not discussed the effect of linear phase on compression performance. Our results indicate that biorthogonal wavelets enjoy a performance advantage over orthogonal due to their linear phase property.

### 1.3 Significance of this work

Matrix based methods have demonstrated a technique for a DWT implementation with symmetric extension using orthogonal wavelets. However, these methods have not been evaluated in the literature. Also, in the past, the performance results of orthogonal wavelets using periodic extension has been compared to biorthogonal wavelets with symmetric extension. The comparison of subjective and objective performance of similar orthogonal and biorthogonal wavelets employing symmetric extension for different image types has also not been reported in the literature. This thesis implements the TDM method and presents performance results for orthogonal and biorthogonal wavelets using both periodic and symmetric extension techniques. Our results for symmetric extension indicate a slight performance advantage for biorthogonal wavelets (particularly for low frequency images); this advantage is significantly smaller than recently published results. Our analysis also demonstrates the importance of linear phase filters on image compression performance. The contributions of this thesis are as follows.

1. Extensive analysis of periodic and symmetric extension techniques for different image types for both orthogonal and biorthogonal wavelets.
2. Comparison of subjective and objective performance of similar orthogonal and biorthogonal wavelets when both employ symmetric signal extension. This comparison is also done for different image types for a wide range of compression ratios.
3. Evaluation of the impact of linear and non-linear wavelet filters on image compression performance.
4. Performance analysis and side by side evaluation of the advantages and disadvantages of the three different DWT implementation techniques.

## 1.4 Organization of this thesis

This thesis is organized as follows. Chapter 2 begins with a brief introduction to a wavelet-based image compression system. This is followed by the description of extension types and different DWT implementation methods. Chapter 2 concludes with a pertinent description of the set partitioning in hierarchical trees (SPIHT) quantization scheme. Chapter 3 analyzes these wavelet properties that are important to image compression. It also discusses the effect of filter properties on SPIHT quantization. Chapter 4 presents and discusses both the objective and subjective performance results for the TDM DWT method. This is done for orthogonal and biorthogonal wavelets using both periodic and symmetric extension techniques. Chapter 5 summarizes our results and concludes this thesis with suggestions for future work.

# Chapter 2

## Background

### 2.1 Overview of wavelet based image compression system

The primary goal of any image compression technique is to reduce the number of bits needed to represent the image with little perceptible distortion. Subband coding using wavelets is one of the best performing techniques among different transform based image compression techniques. Figure 2.1 shows the block diagram of a wavelet based image compression system [24]. The first three blocks (DWT, quantizer and entropy coder) compress the image data whereas the last two blocks (entropy decoder, inverse discrete wavelet transform (IDWT)) reconstruct the image from the compressed data.

The DWT performs an octave frequency subband decomposition of the image information. In its subband representation, an image is more compactly represented since most of its energy is concentrated in relatively few DWT coefficients.

The quantizer then performs quantization by representing the transform coefficients with a limited number of bits. Quantization represents lossy compression—some image information

is irretrievably lost. A quantizer in a DWT-based coder exploits the spatial correlation in a wavelet-based, hierarchical scale-space decomposition.

The entropy coder follows the quantization stage in a wavelet based image compression system. Entropy coding is lossless; it removes the redundancy from the compressed bitstream. However, the typical performance improvement of 0.4-0.6 dB [19] achieved by entropy coding is accompanied by higher computational complexity. We concentrate on the DWT and quantizer blocks and do not consider entropy coding for the results in this thesis. A detailed description of widely used entropy coding schemes is presented in [28].

The channel is the stored or transmitted compressed bitstream. We consider the channel to be noiseless—the received DWT coefficients are free from errors. The synthesis stage reconstructs the image from the compressed data. The entropy decoder and IDWT invert the operations performed by the entropy encoder and DWT, respectively.

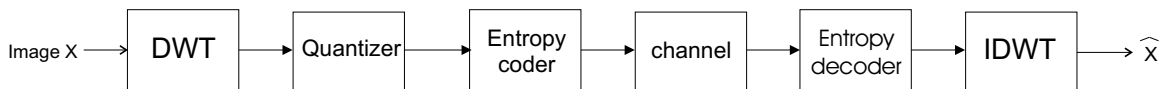


Figure 2.1: Block diagram of a wavelet based lossy compression system.

## 2.2 One and two dimensional discrete wavelet transform

### 2.2.1 Perfect reconstruction filter bank

A perfect reconstruction (PR) filter bank consists of filters that divide the input signal into subbands; the synthesis part of a PR filter bank reconstructs the original signal by recombining the subbands. The structure of a one dimensional (1-D), two channel PR filter bank is shown in Figure 2.2.  $X(z)$  is the 1-D input signal.  $H(z)$  and  $G(z)$  are the  $z$ -

transforms of the analysis lowpass and highpass filters;  $F(z)$  and  $J(z)$  are the z-transforms of the synthesis lowpass and highpass filters.

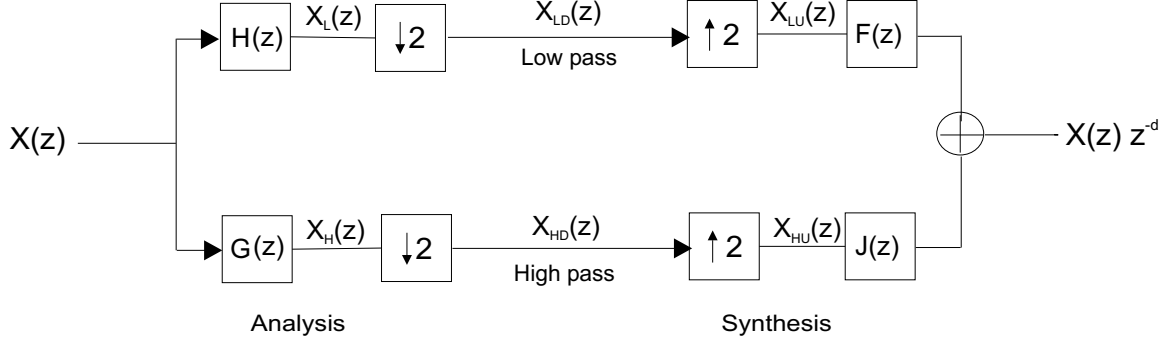


Figure 2.2: 1-D, 1 level PR filter bank

$H(z)$  and  $G(z)$  split the input signal  $X(z)$  into two subbands: lowpass ( $X_L(z)$ ) and highpass ( $X_H(z)$ ). The lowpass and highpass subbands are then downsampled generating  $X_{LD}(z)$  and  $X_{HD}(z)$  respectively. The upsampled signals,  $X_{LU}(z)$  and  $X_{HU}(z)$  are filtered by the corresponding synthesis lowpass ( $F(z)$ ) and highpass ( $J(z)$ ) filters and then added to reconstruct the original signal  $X(z)$  that has an overall delay of  $d$ .

Although downsampling preserves the original sampling rate, it introduces aliasing since the magnitude response of the analysis filters are not ideal brickwall responses (they extend beyond their  $\pi/2$  symmetry point). Apart from aliasing distortion, there are amplitude and phase distortions associated with the analysis filters. The synthesis filters are chosen to cancel the errors introduced by the analysis filters and the relation between the analysis and synthesis is given by the two PR conditions:

$$F(z)H(z) + J(z)G(z) = 2z^{-d}, \quad (2.1)$$

$$F(z)H(-z) + J(z)G(-z) = 0. \quad (2.2)$$

Equation (2.1) is called the ‘no distortion’ condition while Equation (2.2) is called the ‘anti-aliasing’ condition. The relation between the analysis and synthesis filters changes slightly for orthogonal and biorthogonal PR filter banks.

In the case of an orthogonal PR filter bank, the synthesis filters are time reversed versions of the analysis filters:  $F(z) = H(z^{-1})$  and  $J(z) = G(z^{-1})$ . Moreover, the highpass filter is the alternating flip of the lowpass filter,  $G(z) = -z^{-N}H(-z^{-1})$ , where  $N$  is the length of the filter. Thus, the entire filter bank is defined by just one filter—the lowpass analysis filter  $H(z)$ .

In the case of a biorthogonal PR filter bank, the PR conditions are satisfied by choosing  $G(z) = F(-z)$  and  $J(z) = -H(-z)$ . Thus, the biorthogonal filter bank is defined by two filters  $H(z)$  and  $F(z)$ . It is possible to obtain linear phase filters for biorthogonal wavelets unlike the case for orthogonal wavelets, where all the filters are derived from one filter  $H(z)$ .

## 2.2.2 One dimensional discrete wavelet transform

For any signal  $x(t) \in L^2(\mathcal{R})$ , the orthogonal discrete wavelet transform (DWT) analysis and synthesis equations are given by:

$$a_{j,k} = \int x(t)2^{j/2}\phi(2^j t - k)dt \quad b_{j,k} = \int x(t)2^{j/2}\psi(2^j t - k)dt \quad (2.3)$$

$$x(t) = 2^{N/2} \sum_k a_{N,k} \phi(2^N t - k) + \sum_{j=N}^{M-1} 2^{j/2} \sum_k b_{j,k} \psi(2^j t - k). \quad (2.4)$$

and the biorthogonal discrete wavelet transform analysis and synthesis equations are given by:

$$\tilde{a}_{j,k} = \int x(t)2^{j/2}\tilde{\phi}(2^j t - k)dt \quad \tilde{b}_{j,k} = \int x(t)2^{j/2}\tilde{\psi}(2^j t - k)dt \quad (2.5)$$

$$x(t) = 2^{N/2} \sum_k \tilde{a}_{N,k} \phi(2^N t - k) + \sum_{j=N}^{M-1} 2^{j/2} \sum_k \tilde{b}_{j,k} \psi(2^j t - k). \quad (2.6)$$

Equations (2.3) and (2.5) are the orthogonal and biorthogonal analysis (DWT) equations; equations (2.4) and (2.6) are the orthogonal and biorthogonal synthesis (IDWT) equations.

$\phi(t)$  and  $\psi(t)$  in equations (2.3) and (2.4) are the orthogonal scaling and wavelet functions;  $a_{j,k}$  and  $b_{j,k}$  are the corresponding scaling and wavelet coefficients. Biorthogonal wavelets have two sets of scaling and wavelet functions.  $\phi(t)$  and  $\psi(t)$  are the synthesis scaling and wavelet functions and  $\tilde{\phi}(t)$  and  $\tilde{\psi}(t)$  are the analysis scaling and wavelet functions.  $\tilde{a}_{j,k}$  and  $\tilde{b}_{j,k}$  are the scaling and wavelet coefficients respectively; together they form the biorthogonal DWT coefficients of  $x(t)$ .

A DWT is a representation of the signal  $x(t)$  in terms of scale ( $j$ ) and shift ( $k$ ). The lower limit,  $j = N$ , indicates that the DWT captures all the coarse(lowpass) information; the upper limit, ( $j = M - 1$ ), indicates that the DWT must stop at some finest scale.  $M - N$  gives the number of decomposition levels in the DWT of  $x(t)$ .

### 2.2.3 Fast wavelet transform

Mallat's fast wavelet transform (FWT) gives a complete discrete time algorithm for deriving the DWT coefficients for some coarse scale from the coefficients at the next finer scale. Thus, the FWT avoids calculating the inner products as in equations (2.3) and (2.5). The PR bank as shown in Figure 2.2 is used to compute the FWT and IFWT (inverse fast wavelet transform).  $H(z)$  corresponds to the scaling function;  $G(z)$  corresponds to the wavelet function. The orthogonal FWT and IFWT are given by equations (2.7) and (2.8); the corresponding biorthogonal FWT and IFWT are given by equations (2.9) and (2.10).

$$a_{j,k} = \sum_l h(l - 2k)a_{j+1,l} \quad b_{j,k} = \sum_l g(l - 2k)a_{j+1,l} \quad (2.7)$$

$$a_{j+1,l} = \sum_k [h(2k - l)a_{j,k} + g(2k - l)b_{j,k}] \quad (2.8)$$

$$\tilde{a}_{j,k} = \sum_l h(l - 2k)\tilde{a}_{j+1,l} \quad b_{j,k} = \sum_l g(l - 2k)\tilde{a}_{j+1,l} \quad (2.9)$$

$$\tilde{a}_{j+1,l} = \sum_k [f(l-2k)\tilde{a}_{j,k} + j(l-2k)\tilde{b}_{j,k}] \quad (2.10)$$

It can be noted from equations (2.7) and (2.9) that the filter coefficients employed are the time reversed versions of the lowpass and highpass filters in the PR filter bank.

The FWT begins with the computations of the scaling coefficients ( $a_{j+1}$ ) at the finest scale. This is done by either calculating the inner products or setting the coefficients equal to the sampled values of the input. After passing  $a_{j+1,l}$  through one analysis level in the filter bank we get scaling coefficients  $a_{j,k}$  are obtained on the lowpass output branch and the wavelet coefficients  $b_{j,k}$  are obtained on the highpass output branch. For scaling and wavelet coefficients at scales lower than  $j$ , we iterate the analysis stage on  $a_{j,k}$  only. The synthesis stage recovers scaling coefficients at scale  $j+1$  from the scaling and wavelet coefficients at scale  $j$ .

### 2.2.4 Two dimensional discrete wavelet transform

The DWT described in the previous section is for one dimensional (1-D) signals. Images are 2-D and are analyzed using a separable 2-D wavelet transform. A 2-D separable transform is equivalent to two 1-D transforms in series. It is implemented as a 1-D row transform followed by a 1-D column transform on the data obtained from the row transform. Figure 2.3 shows the filter bank structure for computation of a 2-D DWT and IDWT.

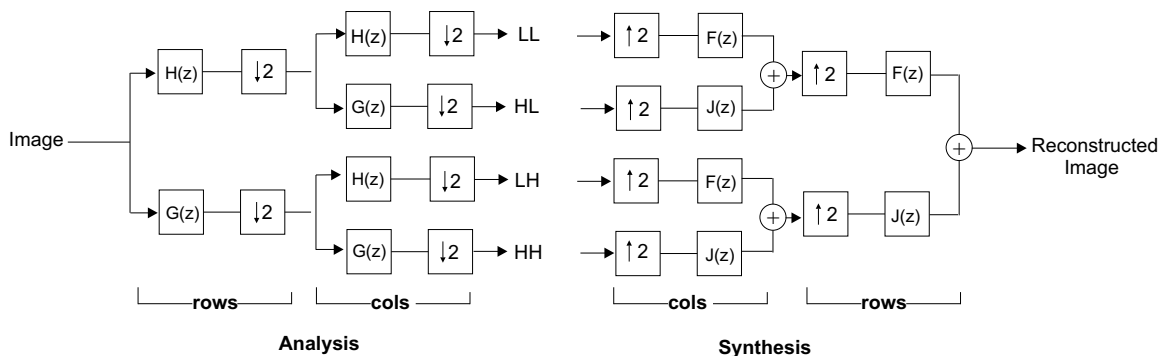


Figure 2.3: One level filter bank for computation of 2-D DWT.

Transform coefficients are obtained by projecting the 2-D input signal onto 2-D basis functions. The separable 2-D basis functions can be expressed as the product of two 1-D basis functions. Unlike two basis functions for 1-D signals at a given scale, there are four basis functions for 2-D signals as given in equation (2.11).

$$\begin{aligned}
\phi(u, v) &= \phi(u)\phi(v) \\
\psi_1(u, v) &= \psi(u)\phi(v) \\
\psi_2(u, v) &= \phi(u)\psi(v) \\
\psi_3(u, v) &= \psi(u)\psi(v)
\end{aligned} \tag{2.11}$$

$\phi(u, v)$  can be thought of as the 2-D scaling function;  $\psi_1(u, v)$ ,  $\psi_2(u, v)$  and  $\psi_3(u, v)$  are the three 2-D wavelet functions. For a 2-D input signal  $x(u, v)$ , the transform coefficients are obtained by projecting the input onto the four basis functions given in equation (2.11). This results in four different subbands in the decomposition corresponding to the four types of transform coefficients ( $X(N, j, m)$ ,  $X^{(1)}(i, j, m)$ ,  $X^{(2)}(i, j, m)$  and  $X^{(3)}(i, j, m)$ ).  $X(N, j, m)$  is the coarse approximation of the 2-D signal  $x(u, v)$  and corresponds to the *LL* band.  $X^{(1)}(i, j, m)$  coefficients contain the vertical details and correspond to the *LH* sub-band.  $X^{(2)}(i, j, m)$  coefficients contain the horizontal details and correspond to the *HL* sub-band.  $X^{(3)}(i, j, m)$  coefficients represent the diagonal details in the image and constitute the *HH* sub-band. The four subbands for one level of decomposition are shown in Figure 2.4.

Thus, the 2-D DWT can be expressed as four inner products given by equation (2.12). As shown in Figure 2.3, it is computed by filtering each row in the image followed by filtering each column of the output obtained from the row filtering .

$$\begin{aligned}
X(N, j, m) &= \int \int x(u, v) 2^N \phi(2^N u - j) \phi(2^N v - m) du dv \Rightarrow LL \\
X^{(1)}(i, j, m) &= \int \int x(u, v) 2^i \psi(2^i u - j) \phi(2^i v - m) du dv \Rightarrow LH \\
X^{(2)}(i, j, m) &= \int \int x(u, v) 2^i \phi(2^i u - j) \psi(2^i v - m) du dv \Rightarrow HL \\
X^{(3)}(i, j, m) &= \int \int x(u, v) 2^i \psi(2^i u - j) \psi(2^i v - m) du dv \Rightarrow HH
\end{aligned} \tag{2.12}$$

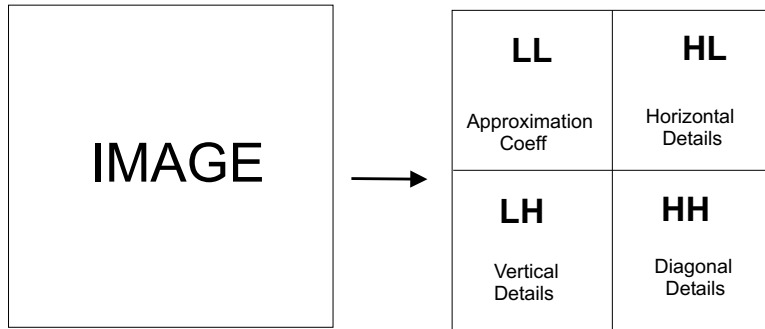


Figure 2.4: Output of 1-level 2-D decomposition

The synthesis stage corresponds to the 2-D IDWT and is given by equation (2.13). The synthesis stage performs upsampling and filtering in the reverse order (column followed by row filtering) to reconstruct the input image  $x(u, v)$ .

$$\begin{aligned}
 x(u, v) = & \sum_j \sum_m X(N, j, m) \cdot 2^N \phi(2^N u - j) \phi(2^N v - m) \\
 & + \sum_{i=-\infty}^{-\infty} \sum_j \sum_m [X^{(1)}(i, j, m) \cdot 2^i \psi(2^i u - j) \phi(2^i v - m) \\
 & + X^{(2)}(i, j, m) \cdot 2^i \phi(2^i u - j) \psi(2^i v - m) \\
 & + X^{(3)}(i, j, m) \cdot 2^i \psi(2^i u - j) \psi(2^i v - m)] \tag{2.13}
 \end{aligned}$$

Multiple level of decompositions achieve higher decorrelation and are generated by iterating the  $LL$  band output only as shown in Figure 2.5.

### 2.2.5 Wavelet decomposition structure

Figure 2.4 shows the structure of a 1-level 2-D wavelet decomposition of an image. For multiple levels of decomposition, the  $LL$  band is iteratively decomposed; this results in a pyramid structure for the subbands with the coarsest subband at the top and the finest subband at the bottom. Figure 2.6 illustrates the pyramid structure obtained after two-level

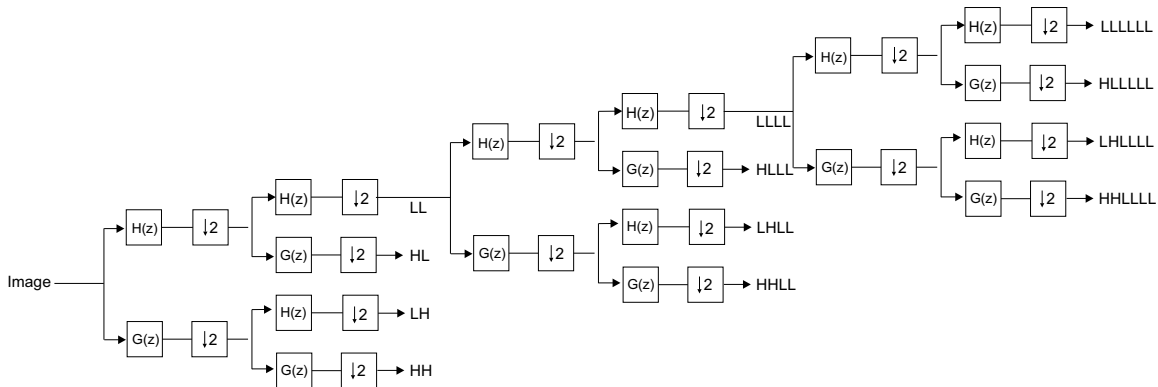


Figure 2.5: 3-level 2-D decomposition

decomposition of the *Lighthouse* image; notice that the LL subband from the first stage has been transformed into 4 subbands- the three other subbands remain unchanged. Color gray in the figure corresponds to the value zero.

The multiresolution nature of the wavelet decomposition compacts the energy in the signal into a small number of wavelet coefficients. For natural images, much of the image energy is concentrated in the LL band that corresponds to the coarsest scale. This can be noted in Figure 2.6. The LL band is not only a coarse approximation of the image but also contains most of the image's energy. In addition to this, it is also statistically observed that the energy in the finer subbands is also concentrated into a relatively small number of wavelet coefficients. The significant coefficients in the finer subbands do not occur at random, but rather tend to occur in clusters in the same relative spatial location in each of the higher frequency subbands. This self-similar, hierarchical nature of the wavelet transform can be used to make interband predictions; the location of the significant coefficients in the coarser bands is used to predict the location and magnitude of significant coefficients in finer subbands.

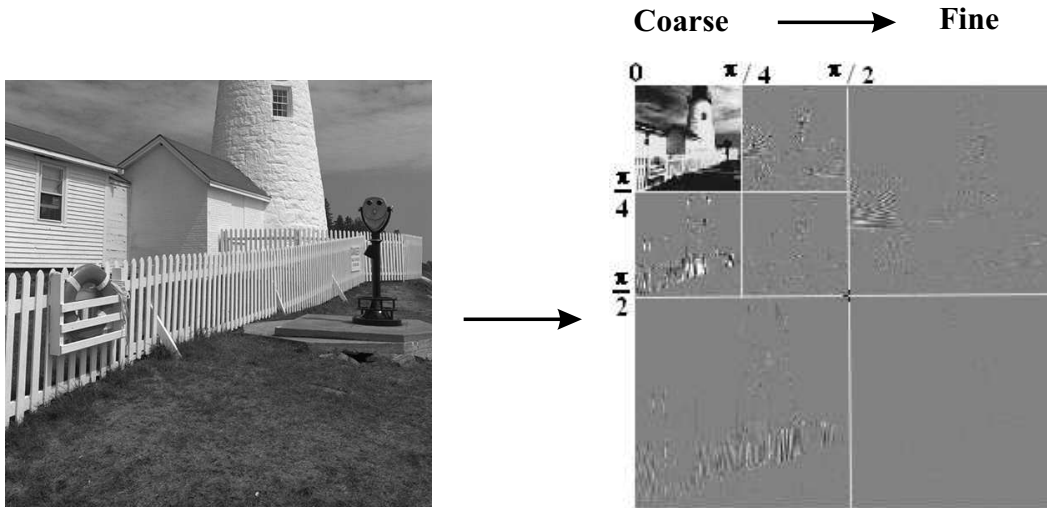


Figure 2.6: 2-Level wavelet decomposition of *Lighthouse* image

## 2.3 Extension techniques

### 2.3.1 Expansive and non-expansive discrete wavelet transform

The DWT is an expansive transform, i.e., the number of output samples is greater than the number of input samples. Figure 2.7 illustrates the expansive DWT for one level of decomposition. We consider a 1-D input of length  $N$  (even) and a set of orthogonal filters of length  $M$  (even). The length of the output for both lowpass and highpass branches combined is equal to  $N + M - 2$ ; this exceeds the number of input samples  $N$ . In general, for  $(N + M)$  that is even, there are  $N + M - 2$  output samples; for  $(N + M)$  that is odd, there are  $N + M - 1$  samples. All the output samples ( $N + M - 2$  or  $N + M - 1$ ) are required in the synthesis stage for reconstructing the original signal. This problem of extra number of output samples that are required for reconstruction worsens with multiple levels decomposition and with increase in filter length ( $M$ ). Table 2.1 shows the percentage increase in the number of DWT coefficients for 1-5 levels of decomposition for different image sizes. It is observed that the percentage increase in the number of DWT coefficients increases for higher levels of decomposition and longer filters. Thus, DWT based on linear convolution

is expansive; this is highly undesirable in image compression. This can be avoided by using circular convolution instead of linear convolution. Circular convolution is not expansive as the two signals, input (length  $N$ ) and filter ( $M$ ) are shifted modulo  $N$ . Hence, the number of samples from both the lowpass and highpass branch combined is equal to the number of input samples ( $N$ ). However, in circular convolution a total of  $M - 1$  (assuming  $N \gg M$ ) outputs samples suffer from aliasing. The original signal can still be reconstructed from the aliased non-expansive DWT since the filter bank is a PR system. However after quantization, circular convolution generates distortion at the boundaries of the image. Hence, to minimize the effect of this distortion, the input signal is extended at the borders. Two such standard extension techniques are discussed in the next two subsections.

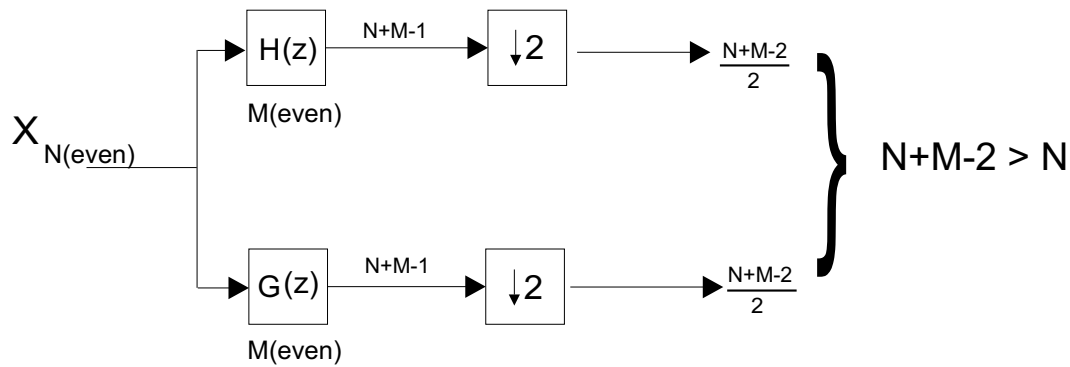


Figure 2.7: Illustration of expansive DWT transform

Table 2.1: DWT based on linear convolution

Image size	Filter length	Percent increase in the no. of DWT coefficients				
		1-Level	2-Level	3-Level	4-Level	5-Level
256 X 256	10	6.3	9.7	11.4	12.7	13.3
	18	12.9	19.9	24	26.7	28.7
512 X 512	10	3.1	4.8	5.6	6.1	6.4
	18	6.3	9.7	11.4	12.5	13.2

### 2.3.2 Periodic extension

Periodic extension is shown by the block diagram in Figure 2.8. Signal extension is accomplished by periodically replicating the entire finite length signal  $X$ ; i.e.  $X = \hat{X}(n \text{ modulo } N)$ . We illustrate each step in Figure 2.8 through an example (refer Figure 2.9). The following notation is used:

- $X$ : input sequence of length 32 samples
- $\hat{X}$ : periodically extended version of  $X$
- $lp_n$ : signals in the lowpass branch of a one-level filter bank
- $hp_n$ : signals in the highpass branch of a one-level filter bank

The step-wise procedure for computation of DWT and IDWT using periodic extension is as follows:

- **Analysis:**
  1.  $lp_1$  and  $hp_1$  correspond to the lowpass and highpass filter outputs. They are obtained by filtering the periodically extended input signal  $\hat{X}$  with the lowpass/highpass filters ( $H(z)/G(z)$ ). It is to be noted that both  $lp_1$  and  $hp_1$  are periodic with period equal to  $N = 32$ . One period of  $lp_1$  and  $hp_1$  is equivalent to the output obtained by  $N$ -point circular convolution of the original input signal  $X$  and the filter coefficients.
  2.  $lp_2$  and  $hp_2$  are the downsampled lowpass and highpass filter outputs.  $lp_2$  and  $hp_2$  are periodic with period equal to  $N = 16$ .
  3.  $lp_3$  and  $hp_3$  are the samples retained to be fed to the synthesis stage.  $lp_3$  and  $hp_3$  are 16 ( $N/2$ ) samples each. They are obtained by performing an  $N/2$  windowing operation.  $lp_3$  and  $hp_3$  would also correspond to the downsampling of the output obtained through circular convolution as discussed in (1).

- **Synthesis:**

1.  $lp_4$  and  $hp_4$  are formed by periodically replicating  $lp_3$  and  $hp_3$ . They are periodic with period equal to  $N = 16$ .
2.  $lp_5$  and  $hp_5$  are generated by upsampling  $lp_4$  and  $hp_4$ .  $lp_5$  and  $hp_5$  are periodic with period equal to  $N = 32$ .
3.  $lp_6$  and  $hp_6$  are the synthesis low and highpass filter outputs obtained by filtering the periodic input sequences ( $lp_5$  and  $hp_5$ ) using the filters ( $F(z)$  and  $G(z)$ ).  $lp_6$  and  $hp_6$  are periodic with period equal to  $N = 32$ . One period of  $lp_6$  and  $hp_6$  is equivalent to the output obtained by N-point circular convolution of the signals ( $lp_5$  and  $hp_5$ ) and the respective filter coefficients ( $F(z)$  and  $G(z)$ ).
4. The  $lp_6$  and  $hp_6$  outputs are combined to generate  $\hat{X}$  that is periodic with period equal to  $N = 32$ . The reconstructed signal  $X$  is obtained from  $\hat{X}$  by an N-point windowing operation.

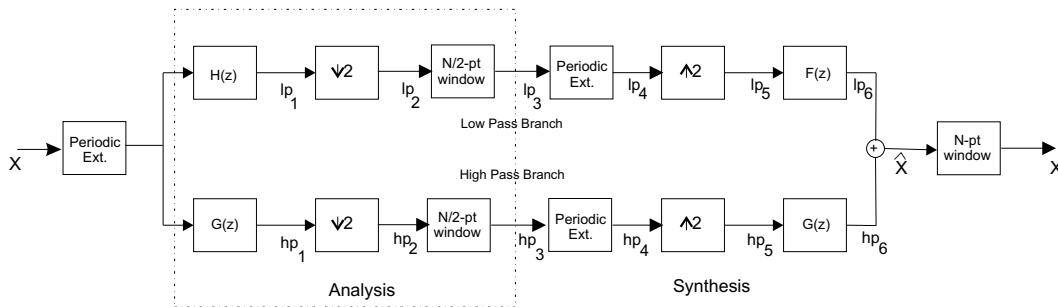


Figure 2.8: Block diagram for periodic extension

Periodic extension is implemented using circular convolution of the signal with the filter coefficients (equivalent to linear convolution of periodic signal with filter coefficients). It can be noted, from Figure 2.9(b), that periodic extension of the signal introduces jumps at the boundaries; this is because the start and the end of any signal are more likely to be different. This discontinuity generates high frequency artifacts in the transform domain.

The original signal can still be reconstructed from the transform coefficients provided there is no compression. However, for lossy compression, these artifacts are undesirable because:

1. these large coefficients corresponding to these artifacts occur in the high frequency subbands. The quantizer utilizes more bits to code these artifacts ; and,
2. these artifacts do not represent real information present in the input signal, instead they are spurious features resulting from the method used to do the transform.

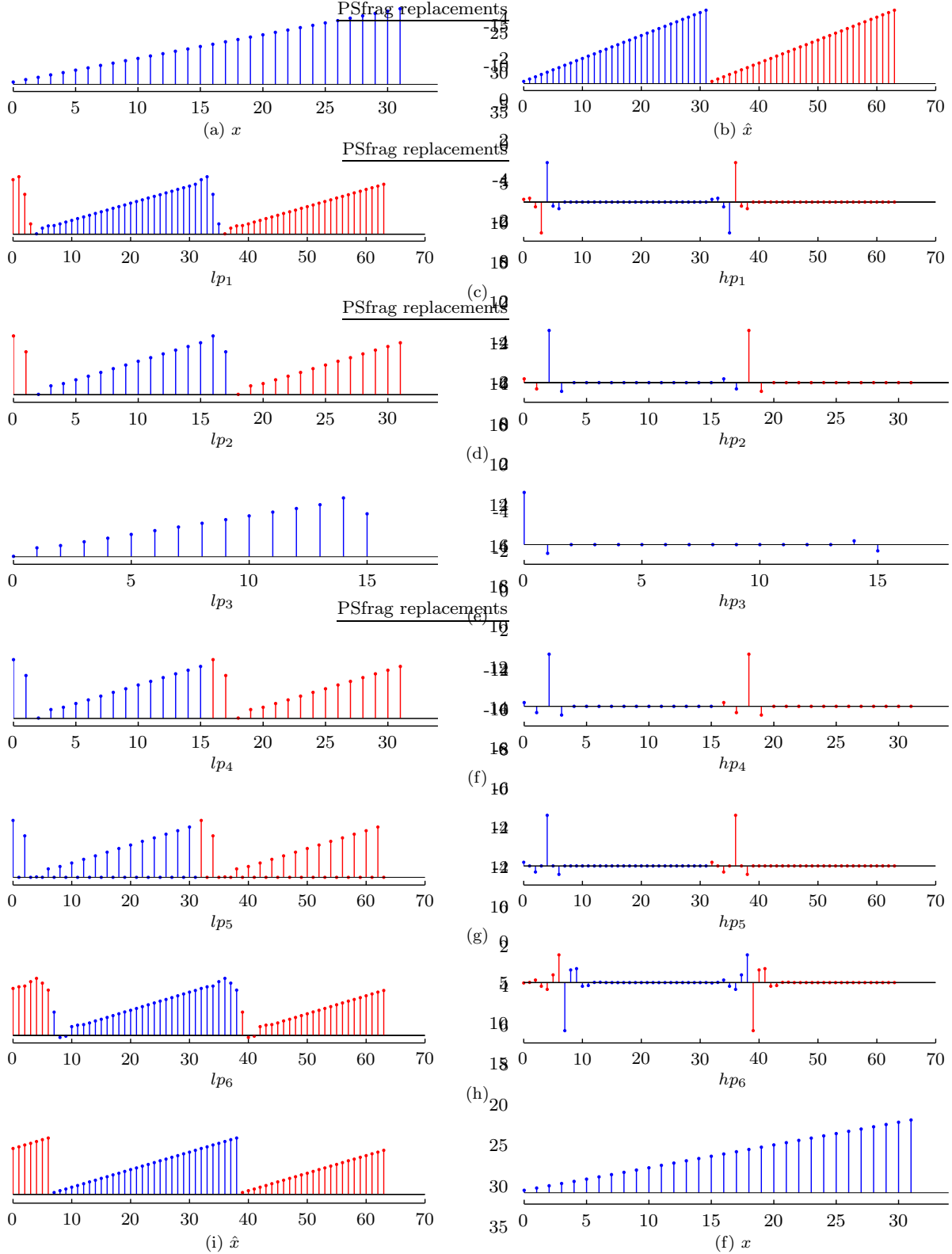


Figure 2.9: Periodic extension example. Signals in red represent the extended/discarded samples while signals in blue represent the input/preserved samples at each stage.

### 2.3.3 Symmetric extension

Symmetric extension is shown by the block diagram in Figure 2.10. Signal extension for symmetric extension is described below:

The input signal (length  $N$ ) is symmetrically extended. There are two ways of extending the sequence based on whether the length of the filter is odd or even. For an even length filter, the extended signal  $\hat{X}$ , has length  $2N$  and can be expressed by:

$$\hat{x}(n) = \begin{cases} x(n) & : 0 \leq n \leq N - 1 \\ x(2N - n - 1) & : N \leq n \leq 2N - 1 \\ 0 & : \textit{otherwise} \end{cases} \quad (2.14)$$

while for an odd length filter,  $\hat{X}$  has length  $2N - 2$  and can be expressed by:

$$\hat{x}(n) = \begin{cases} x(n) & : 0 \leq n \leq N - 1 \\ x(2N - n - 2) & : N \leq n \leq 2N - 3 \\ 0 & : \textit{otherwise} \end{cases} \quad (2.15)$$

We explain the operation of each block in Figure 2.10 by stepping through an example (refer Figure 2.11).  $H(z)$ ,  $G(z)$ ,  $F(z)$  and  $J(z)$  are the biorthogonal 9/7 symmetric filters. The notation used is as given below:

- $X$ : input sequence of length 32 samples
- $\hat{X}$ : symmetrically extended version of  $X$  (period  $N = 64$ )
- $lp_n$ : signals in the lowpass branch of a one-level filter bank
- $hp_n$ : signals in the highpass branch of a one-level filter bank

The step-wise procedure for computation of DWT and IDWT using periodic extension is as follows:

- **Analysis:**

1.  $lp_1$  and  $hp_1$  correspond to the lowpass and highpass filter outputs; they are obtained by circular convolution of the symmetrically extended input signal  $\hat{X}$  and the lowpass/highpass filters ( $H(z)/G(z)$ ). It is to be noted that both  $lp_1$  and  $hp_1$  obtained through circular convolution are symmetric-periodic with period equal to  $N = 64$ .
2.  $lp_2$  and  $hp_2$  are the downsampled lowpass and highpass filter outputs.  $lp_2$  and  $hp_2$  are also symmetric-periodic with period equal to  $N = 32$ .
3.  $lp_3$  and  $hp_3$  constitute the non-expansive DWT coefficients. We need to retain half the number of downsampled outputs ( $N = 16$ ) in each branch as the downsampled outputs ( $lp_2$  and  $hp_2$ ,  $N = 32$ ) are symmetric.

- **Synthesis:**

1.  $lp_4$  and  $hp_4$  are formed by symmetric extension of  $lp_3$  and  $hp_3$ . However, for odd length symmetric filters, (1,2)-extension (i.e. the start sample of the input sequence is repeated only once while the end sample is repeated twice. *Vice-versa* for (2,1) extension) is followed for the input signal to the lowpass filters and (2,1)-extension is followed for the input signal to the highpass filter. Thus,  $lp_4$  and  $hp_4$  are periodic with period  $N = 32$ .
2.  $lp_5$  and  $hp_5$  are generated by upsampling  $lp_4$  and  $hp_4$ .  $lp_5$  and  $hp_5$  are symmetric-periodic with period equal to  $N = 64$ .
3.  $lp_6$  and  $hp_6$  are the synthesis low and highpass filter outputs obtained by the circular convolution of the symmetric input sequences ( $lp_5$  and  $hp_5$ ) with the synthesis filters ( $F(z)$  and  $G(z)$ ).  $lp_6$  and  $hp_6$  are periodic with period equal to  $N = 64$ .
4. The  $lp_6$  and  $hp_6$  outputs are combined to generate  $\hat{X}$  that is symmetric-periodic with period equal to  $N = 64$ . The reconstructed signal  $X$  is obtained from  $\hat{X}$  by

an  $N$ -point windowing operation.

Symmetric extension is implemented using circular convolution of the symmetrically extended signal with the filter coefficients. It can be noted, from Figure 2.11(b), that symmetric extension unlike periodic extension does not introduce jumps at the boundaries as the signal boundaries are continuous.

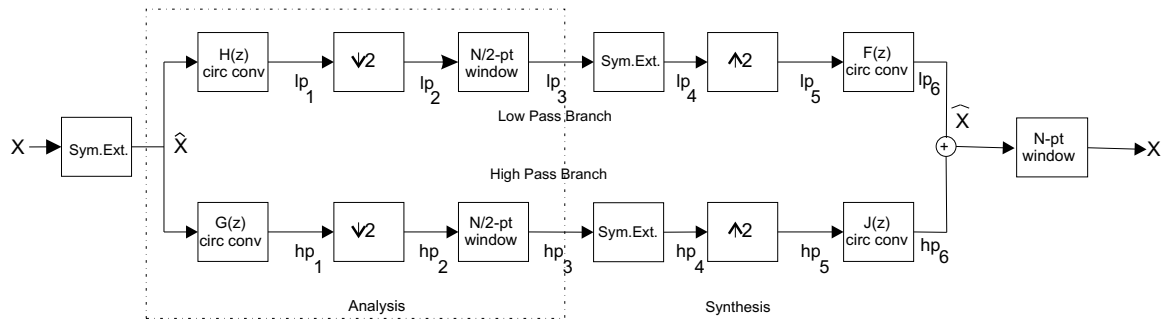


Figure 2.10: Block diagram for symmetric extension

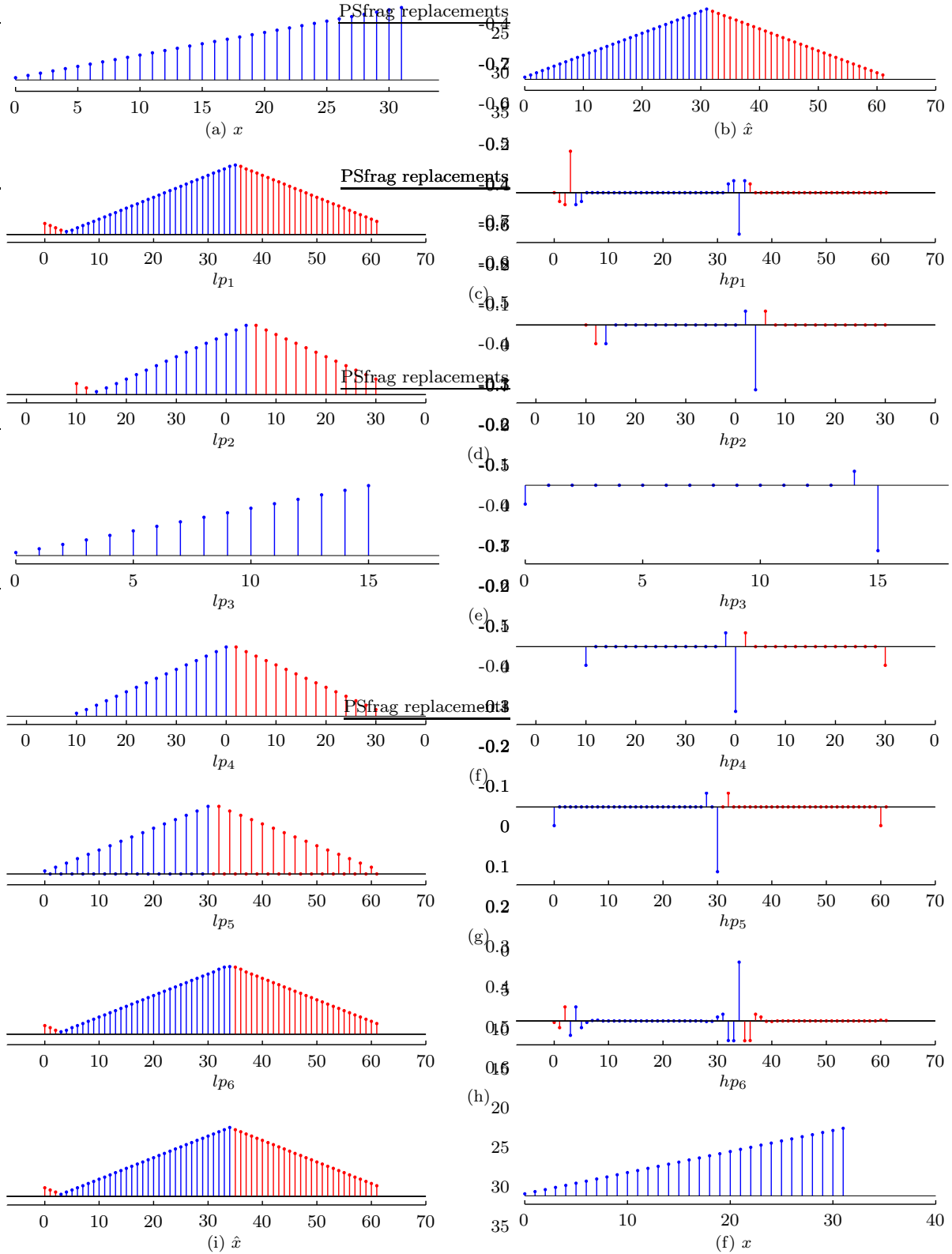


Figure 2.11: Symmetric extension example. Signals in red represent the extended/discarded samples while signals in blue represent the input/preserved samples at each stage.

## 2.4 DWT implementation methods

This section outlines three methods for computing the non-expansive DWT with either symmetric or periodic extension.

### 2.4.1 Fast fourier transform method

The fast Fourier transform (FFT) method computes the DWT by performing filtering operations in the frequency domain. This method allows the implementation of periodic extension technique for both biorthogonal and orthogonal wavelets. We discuss the method for both periodic and symmetric extension.

- **Periodic extension**

The block diagram in Figure 2.12 shows the computation of the non-expansive DWT coefficients with periodic extension. We use the example as shown in Figure 2.9 to illustrate the different intermediate signals. The simultaneous operations of signal extension and circular convolution is implemented by DFT and IDFT operations i.e. the output is obtained by the multiplication of 32 point DFTs of the input signal and the filters and subsequently taking a 32 point IDFT of the output. It is to be noted that multiplying DFTs correspond to circular convolution in time domain. The IDFT operation yields signals  $lp_1$  and  $hp_1$  each of length 32. Downsampling results in two 16 length DWT signals,  $lp_2$  and  $hp_2$  (correspond to signals  $lp_3$  and  $hp_3$  in Figure 2.9). The analysis stage is not connected directly to the synthesis stage to indicate that  $lp_2$  and  $hp_2$  can be stored and quantized to achieve compression before the signals are input into the synthesis stage. Frequency domain filtering of the upsampled signals ( $lp_3$  and  $hp_3$ ) and subsequent combining results in the reconstructed signal.

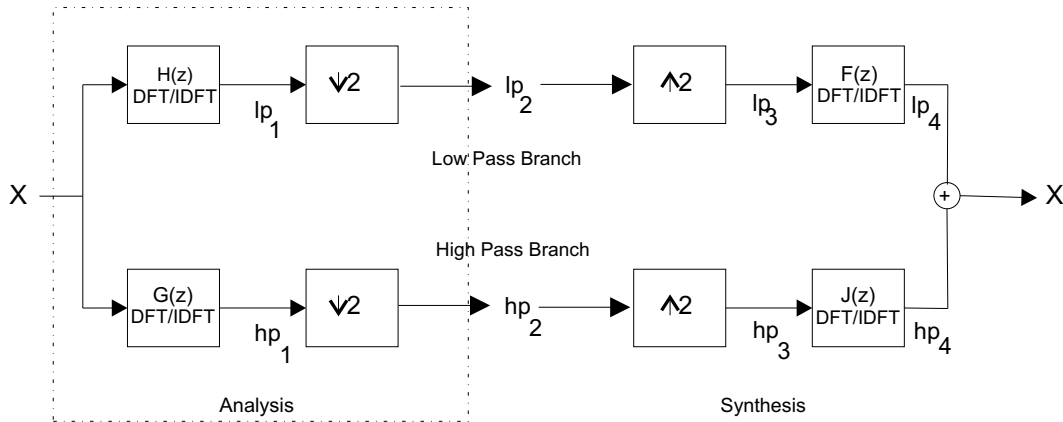


Figure 2.12: Block diagram of the FFT method with periodic extension

- **Symmetric extension**

Figure 2.13 shows the block diagram for computation of the non-expansive DWT coefficients with symmetric extension. We again use the example as shown in Figure 2.11 to illustrate the different intermediate signals. The input signal is initially extended according to equations (2.14) or (2.15). Frequency domain filtering of the extended signal  $\hat{X}$  (length  $2N/(2N-2)$ , in our case  $(2 \times 32) - 2 = 62$ ) is equivalent to circular convolution of a symmetrically extended signal; this yields two filtered outputs, each of length 62 in our case. Downsampling results in signals  $lp_2$  and  $hp_2$  of length 31 each. Thus, we observe that the total number of DWT samples (62) exceeds the input (32). However, for symmetric filters, the filtered output is also symmetric (refer Figure 2.11(d)). Hence, we can keep half the number of samples ( $lp_3$  and  $hp_3$ ) thus yielding a non-expansive DWT transform. The DWT coefficients from the analysis stage ( $lp_3$  and  $hp_3$ ) are symmetrically extended as follows:

- $lp_3$  undergoes (1,2) symmetric extension: the first sample is repeated once and the last sample is repeated twice to generate  $lp_4$ . (1,2) extension is required for odd length filters (in our case biorthogonal 9/7) while (2,2) extension is done for even length filters.

- $hp_3$  undergoes (2,1) symmetric extension: the first sample is repeated twice and the last sample is repeated only once  $hp_4$ . (2,1) extension is required for odd length filters whereas (2,2) extension is done for even length filters.

Frequency domain filtering of the upsampled signals ( $lp_4$  and  $hp_4$ ) and subsequent combining results in the symmetric output  $\hat{X}$ . N-point windowing results in the original signal  $X$ .

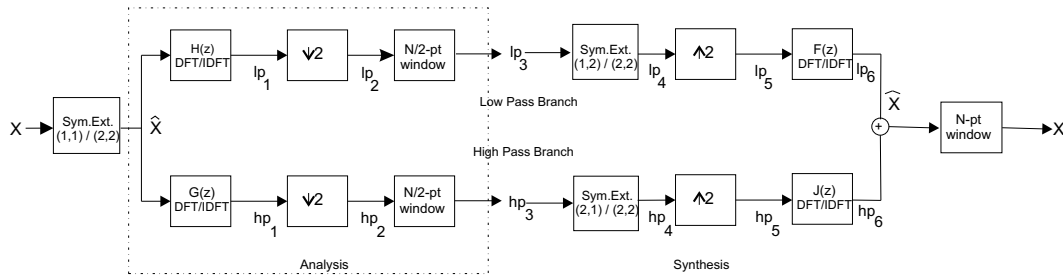


Figure 2.13: Block diagram of the FFT method with symmetric extension

## 2.4.2 Time domain convolution method

The time domain convolution (TDC) approach to compute the DWT uses linear convolution to compute the DWT coefficients. The wavelet and the extension technique combination that can be implemented using TDC is same as the FFT method: symmetric extension for biorthogonal filters and periodic extension for both orthogonal as well as biorthogonal filters. We illustrate both periodic and symmetric extension below through examples. We use  $D_4$  (length 8) least asymmetric orthogonal Daubechies filters for periodic extension and biorthogonal 9/7 for symmetric extension. The following notation is used throughout this section:

- $X$ : input sequence of length 32 samples
- $\hat{X}$ : periodically extended version of  $X$

- $lp_n$ : signals in the lowpass branch of a one-level filter bank
- $hp_n$ : signals in the highpass branch of a one-level filter bank
- **Periodic extension**

The block diagram for periodic extension is shown in Figure 2.14 and the corresponding example is shown in Figure 2.15. The input signal  $X$  is extended by 3 ( $M/2 - 1$  for even and  $(M - 1)/2$  for odd) samples on either side of the signal periodically as shown in Figure 2.15(b) yielding the extended signal  $\hat{X}$  of length 38.  $lp_1$  and  $hp_1$ , each of length 45, are obtained by linear convolution of the extended signal  $\hat{X}$  and the filters ( $H(z)$  and  $G(z)$ ). It is to be noted that the middle  $N$  filter outputs obtained by linear convolution of the extended signal are same as that obtained by circular convolution of the input signal  $X$ .  $lp_2$  and  $hp_2$  are the downsampled versions of  $lp_1$  or  $hp_1$ , each of length 22. Windowing operation yields the non-expansive DWT coefficients (length 16) for both lowpass and highpass branches. The DWT coefficients are again periodically extended by 3 samples on either side as before resulting in extended signals ( $lp_4$  and  $hp_4$ ). Linear convolution of the upsampled outputs ( $lp_5$  and  $hp_5$ ) result in final lowpass and highpass outputs ( $lp_6$  and  $hp_6$ ). The final reconstructed signal is obtained by combining  $lp_6$  and  $hp_6$  followed by a windowing operation.

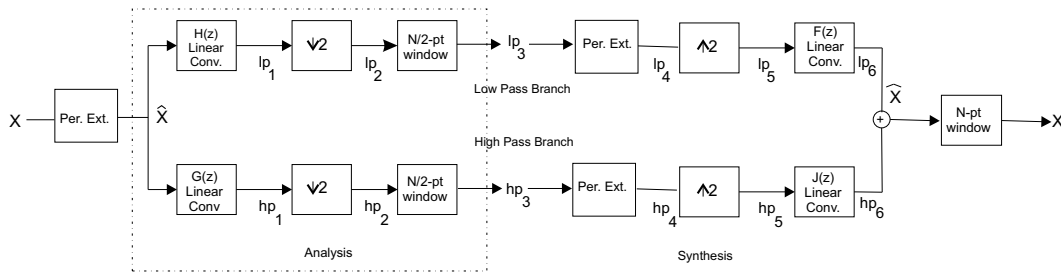


Figure 2.14: Block diagram of TDC method with periodic extension

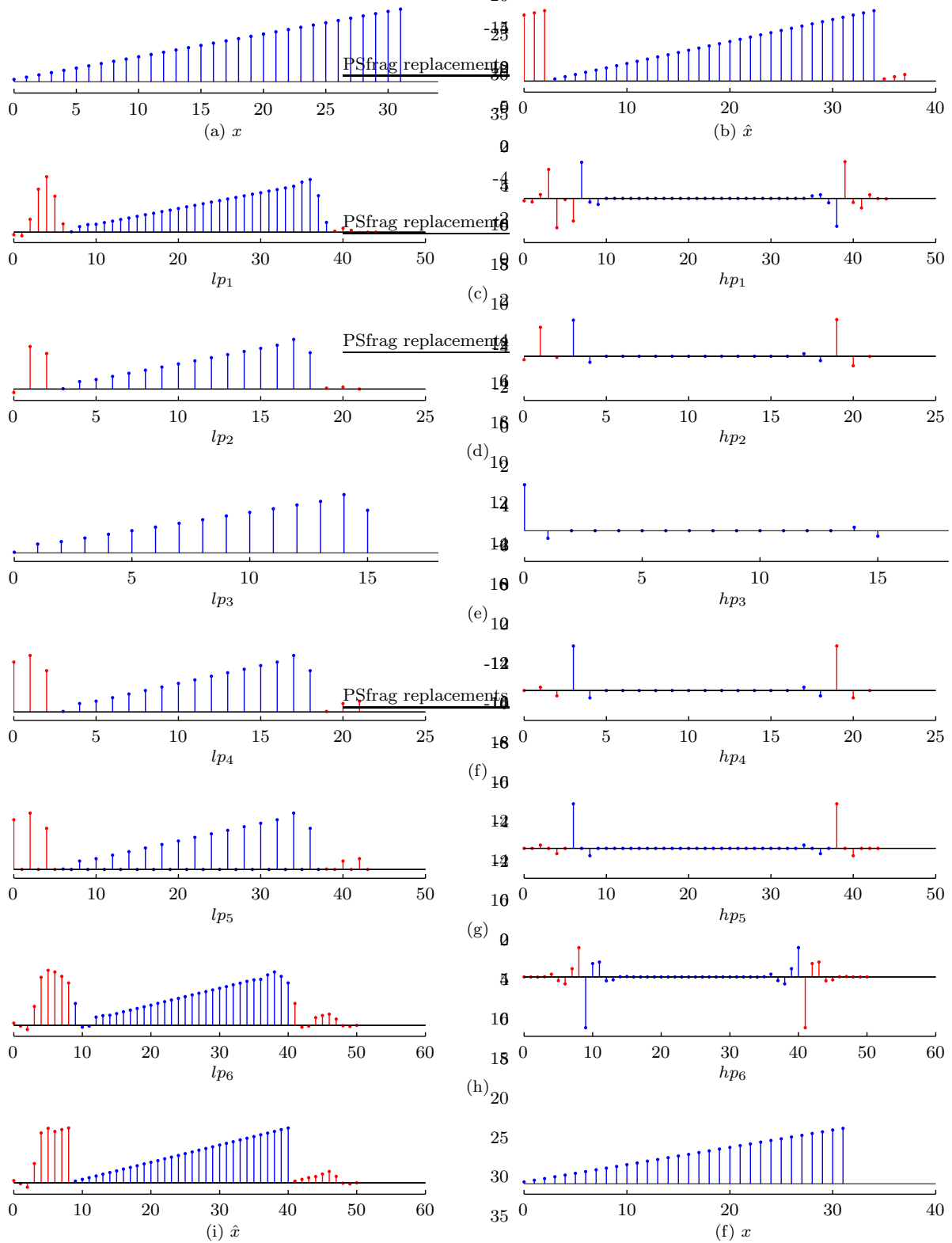


Figure 2.15: TDC method periodic extension example. Red represents the extended/discarded samples while blue represents the input/preserved samples at each stage.

- **Symmetric extension**

The block diagram for symmetric extension is shown in Figure 2.16; the corresponding example is shown in Figure 2.17. The input signal  $X$  is symmetrically extended by  $4 \left( \frac{M-1}{2} - B_{9/7} \right)$  samples on either side of the signal as shown in Figure 2.17(b) yielding the extended signal  $\hat{X}$  of length 40. The extended signal is either (1,1) for odd filters or (2,2) for even filters.  $lp_1$  and  $hp_1$ , each of length 48, are obtained by linear convolution of the extended signal  $\hat{X}$  and the filters ( $H(z)$  and  $G(z)$ ). The downsampled signals,  $lp_2$  and  $hp_2$  are each of length 24. Windowing operation yields the non-expansive DWT coefficients (length 16) for both lowpass and highpass branches. The DWT coefficients are again symmetrically extended by 4 samples on either side as before resulting in extended signals ( $lp_4$  and  $hp_4$ ). In our case,  $lp_3$  and  $hp_3$  undergo (1,2) and (2,1) extension. Linear convolution of the upsampled outputs ( $lp_5$  and  $hp_5$ ) with the synthesis filters ( $F(z)$  and  $G(z)$ ) result in final lowpass and highpass outputs ( $lp_6$  and  $hp_6$ ). The final reconstructed signal is obtained by combining  $lp_6$  and  $hp_6$  followed by a windowing operation.

The FFT and TDC methods with symmetric extension cannot be used with non-linear filters (i.e. orthogonal wavelets). The complication arises in the computation of the inverse transform. The convolution of two symmetric inputs yields a symmetric output (desired as half the number of samples needs to be retained). However, the convolution of a symmetric input with another non-symmetric input yields a non-symmetric output. Hence, the DWT coefficients for orthogonal wavelets do not show redundancy as in the case of linear phase filters. Thus, some (depends on filter length) DWT coefficients corresponding to the boundaries of the signals are discarded at the analysis stage to keep the process non-expansive. Recovering these discarded coefficients from the received coefficients is non trivial using TDC or FFT based implementation methods. The matrix based method discussed next provides a way to retrieve these truncated coefficients from the received coefficients.

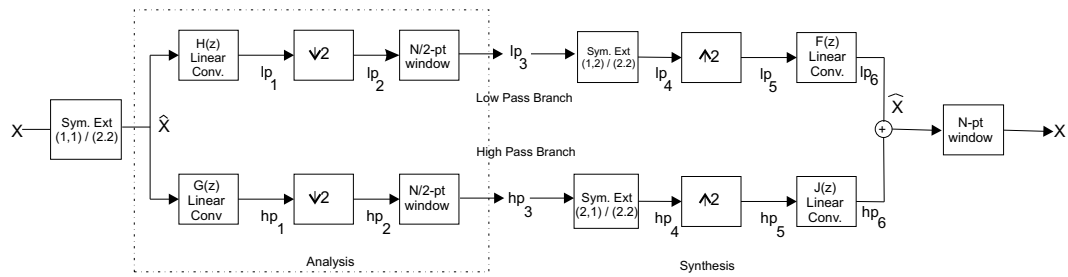


Figure 2.16: Block diagram of TDC method with symmetric extension

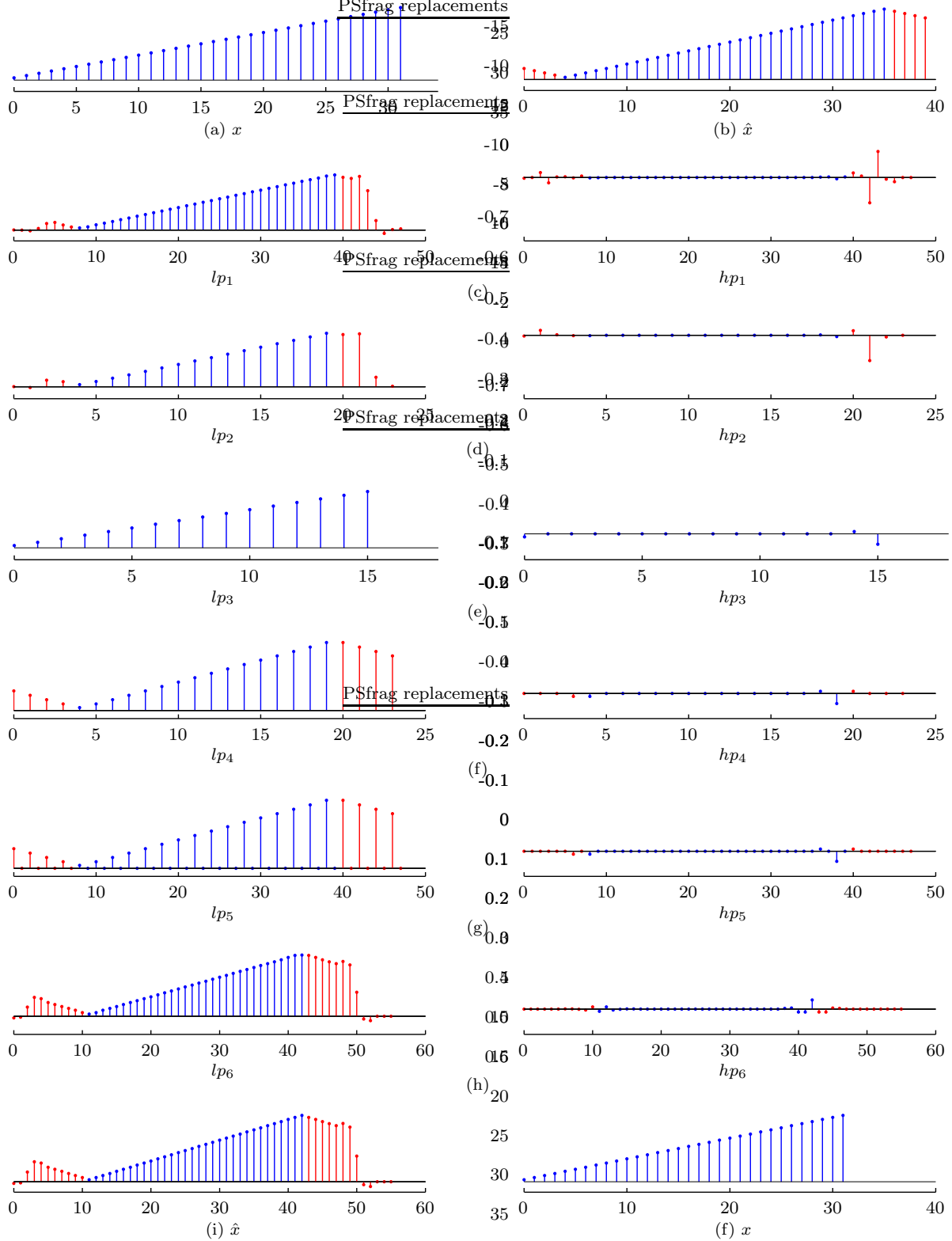


Figure 2.17: TDC method symmetric extension example. Red represents the extended/discarded samples while blue represents the input/preserved samples at each stage.

### 2.4.3 Time domain matrix method

The FFT and TDC methods cannot be used with non-linear phase filters. Recently developed matrix based methods provide an alternative for computing a non-expansive DWT [1, 4, 22]. These matrix methods operate in the time domain and regenerate transform coefficients truncated during the decomposition process; the inverse DWT is calculated using this extended signal. The time domain matrix (TDM) method introduced by Silva and Sa is used to implement the matrix method in this thesis [22]. We discuss the Silva and Sa method below; we also illustrate both types of extensions through examples.

- **Silva and Sa Method**

The signal extensions in TDM are described by linear combination of input signal samples. Thus, both symmetric and periodic extension techniques can be implemented for both biorthogonal and orthogonal wavelets. The TDM method for a two subband system is discussed below.

The input signal  $x$ , of length  $N$ , is extended by length  $Q = M - 2$  (even filters) or  $Q = M - 1$  (odd filters) to generate the extended signal  $\hat{x}$ . The appended signal  $x_{ex}$  and the extended signal  $\hat{x}$ , can be expressed by equations (2.16) and (2.17):

$$x_{ex} = Ex \tag{2.16}$$

$$\hat{x} = \begin{bmatrix} x \\ x_{ex} \end{bmatrix} \tag{2.17}$$

where  $E$  is the signal extension matrix of dimension  $Q \times N$ .  $E$  matrix for symmetric extension and periodic extension for a 10 length filter are shown in equations (2.4.3(a)) and (2.4.3(b)).

The analysis stage transform matrix ( $A$ ) of size  $(Q + N) \times (Q + N)$  operates on the extended input signal  $\hat{x}$ . Matrix  $A$  is shown in equation (2.18).  $h$  and  $g$  are analysis lowpass and highpass filters. Downsampling is achieved by dyadic circular shifts of rows.

$$E = \begin{bmatrix} 0 & 0 & 0 & 0 & \cdots & 0 & 0 & 0 & 0 & 0 & 1 \\ 0 & 0 & 0 & 0 & \cdots & 0 & 0 & 0 & 1 & 0 & 0 \\ 0 & 0 & 0 & 0 & \cdots & 0 & 0 & 1 & 0 & 0 & 0 \\ 0 & 0 & 0 & 0 & \cdots & 0 & 1 & 0 & 0 & 0 & 0 \\ 0 & 0 & 0 & 1 & \cdots & 0 & 0 & 0 & 0 & 0 & 0 \\ 0 & 0 & 1 & 0 & \cdots & 0 & 0 & 0 & 0 & 0 & 0 \\ 0 & 1 & 0 & 0 & \cdots & 0 & 0 & 0 & 0 & 0 & 0 \\ 1 & 0 & 0 & 0 & \cdots & 0 & 0 & 0 & 0 & 0 & 0 \end{bmatrix}_{Q \times N}$$

(a) Symmetric extension

$$E = \begin{bmatrix} 1 & 0 & 0 & 0 & \cdots & 0 & 0 & 0 & 0 & 0 & 0 \\ 0 & 1 & 0 & 0 & \cdots & 0 & 0 & 0 & 0 & 0 & 0 \\ 0 & 0 & 1 & 0 & \cdots & 0 & 0 & 0 & 0 & 0 & 0 \\ 0 & 0 & 0 & 1 & \cdots & 0 & 0 & 0 & 0 & 0 & 0 \\ 0 & 0 & 0 & 0 & \cdots & 0 & 1 & 0 & 0 & 0 & 0 \\ 0 & 0 & 0 & 0 & \cdots & 0 & 0 & 1 & 0 & 0 & 0 \\ 0 & 0 & 0 & 0 & \cdots & 0 & 0 & 0 & 1 & 0 & 0 \\ 0 & 0 & 0 & 0 & \cdots & 0 & 0 & 0 & 0 & 1 & 0 \\ 0 & 0 & 0 & 0 & \cdots & 0 & 0 & 0 & 0 & 0 & 1 \end{bmatrix}_{Q \times N}$$

(b) Periodic extension

$$A = \begin{bmatrix} h_{D-1} & \cdots & h_2 & h_1 & h_0 & 0 & 0 & 0 & 0 & \cdots & \cdots & 0 & 0 & h_{M-1} & \cdots & h_{D-3} & h_{D-2} \\ g_{D-1} & \cdots & g_2 & g_1 & g_0 & 0 & 0 & 0 & 0 & \cdots & \cdots & 0 & 0 & g_{M-1} & \cdots & g_{D-3} & g_{D-2} \\ h_{D-3} & h_{D-2} & h_{D-1} & \cdots & h_2 & h_1 & h_0 & 0 & 0 & 0 & 0 & \cdots & \cdots & 0 & 0 & h_{M-1} & \cdots \\ g_{D-3} & g_{D-2} & g_{D-1} & \cdots & g_2 & g_1 & g_0 & 0 & 0 & 0 & 0 & \cdots & \cdots & 0 & 0 & g_{M-1} & \cdots \\ \vdots & \vdots \\ \vdots & \vdots \\ h_0 & 0 & 0 & 0 & 0 & \cdots & \cdots & 0 & 0 & h_{M-1} & \cdots & h_{D-3} & h_{D-2} & h_{D-1} & \cdots & h_2 & h_1 \\ g_0 & 0 & 0 & 0 & 0 & \cdots & \cdots & 0 & 0 & g_{M-1} & \cdots & g_{D-3} & g_{D-2} & g_{D-1} & \cdots & g_2 & g_1 \\ h_2 & h_1 & h_0 & 0 & 0 & 0 & 0 & \cdots & \cdots & 0 & 0 & h_{M-1} & \cdots & h_{D-3} & h_{D-2} & h_{D-1} & \cdots \\ g_2 & g_1 & g_0 & 0 & 0 & 0 & 0 & \cdots & \cdots & 0 & 0 & g_{M-1} & \cdots & g_{D-3} & g_{D-2} & g_{D-1} & \cdots \end{bmatrix}$$

$$= \begin{bmatrix} \mathbf{A}_0 & \mathbf{A}_1 \\ \mathbf{A}_2 & \mathbf{A}_3 \end{bmatrix}_{(Q+N) \times (Q+N)} \quad (2.18)$$

where  $D = M - Q/2$  and the sizes of  $\mathbf{A}_0$ ,  $\mathbf{A}_1$ ,  $\mathbf{A}_2$  and  $\mathbf{A}_3$  are  $N \times N$ ,  $N \times Q$ ,  $Q \times N$  and  $Q \times Q$  respectively.

The DWT output  $\hat{y}$  can be split into two: the transmitted DWT coefficients,  $y$  and the extra samples,  $y_{ex}$  that needs to be truncated to keep the DWT process non-expansive (refer equation (2.19)).

$$\begin{bmatrix} \mathbf{y} \\ \mathbf{y}_{ex} \end{bmatrix} = \begin{bmatrix} \mathbf{A}_0 & \mathbf{A}_1 \\ \mathbf{A}_2 & \mathbf{A}_3 \end{bmatrix} \times \begin{bmatrix} \mathbf{x} \\ \mathbf{x}_{ex} \end{bmatrix} \quad (2.19)$$

The truncated expansive coefficients  $y_{ex}$  regenerated from the non-expansive coefficients  $y$ , are given by:

$$y_{ex} = (\mathbf{A}_2 + \mathbf{A}_3 \mathbf{E})(\mathbf{A}_0 + \mathbf{A}_1 \mathbf{E})^{-1} y \quad (2.20)$$

Periodic extension is implemented by modifying the  $E$  matrix given in Equation (2.4.3(b)).

- **Example:**

The block diagrams of TDM method with periodic and symmetric extension are shown in Figures 2.20 and 2.19. We use orthogonal wavelet ( $D_{5LA}$ ) and explain the intermediate signals for symmetric extension through an example as shown in Figure 2.18. The notation used is given as below:

- $X$ : input sequence of length 32 samples
- $\hat{X}$ : symmetrically extended version of  $X$
- $lp_n$ : signals in the lowpass branch of a one-level filter bank
- $hp_n$ : signals in the highpass branch of a one-level filter bank

The symmetrically extended signal  $\hat{X}$  is obtained using equations (2.16) and (2.17). The length of  $\hat{X}$  is 40 samples.

- **Analysis:**

1.  $lp_1$  and  $hp_1$  correspond to the lowpass and highpass filter outputs; they are obtained by circular convolution of the symmetrically extended input signal  $\hat{X}$  and the lowpass/highpass filters ( $H(z)/G(z)$ ). It is to be noted that both  $lp_1$  and  $hp_1$  are obtained through a 40-point circular convolution (32 unaliased and 8 aliased outputs).
2.  $lp_2$  and  $hp_2$  (20 samples each) are the downsampled versions of  $lp_1$  and  $hp_1$ . The simultaneous operations of circular convolution and downsampling is achieved by matrix A in equation (2.18); its output corresponds to  $lp_2$  and  $hp_2$ .
3.  $lp_3$  and  $hp_3$  constitute the non-expansive DWT coefficients and are obtained by a windowing operation that retains the unaliased samples in  $lp_2$  and  $hp_2$

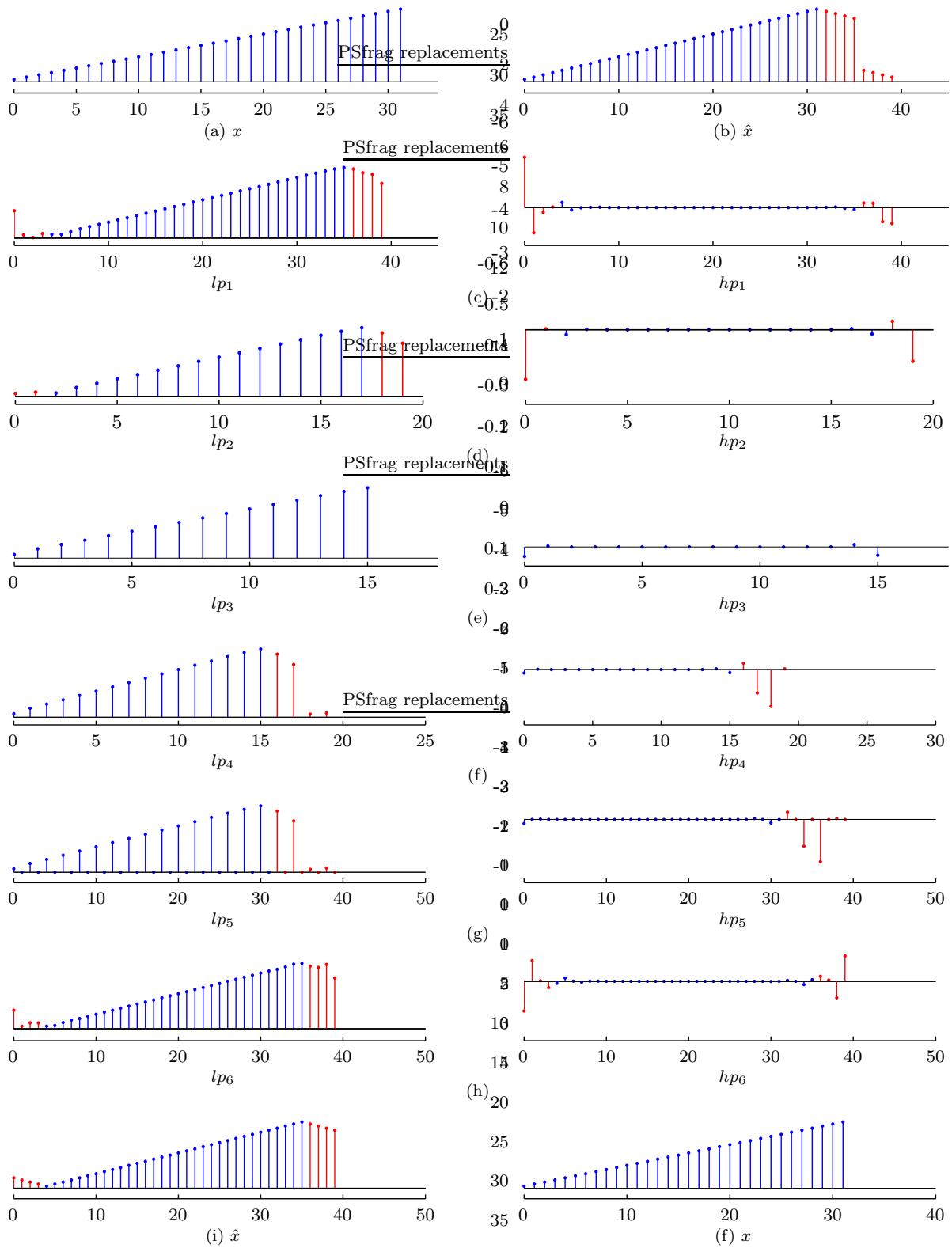


Figure 2.18: TDM method symmetric extension example. Red represents the extended/discarded samples while blue represents the input/preserved samples at each stage.

– **Synthesis:**

1.  $lp_3$  and  $hp_3$  are used to regenerate the truncated coefficients ( $y_{ex}$  as in equation (2.20)). The corresponding regenerated coefficients for lowpass and highpass branches are padded at the back of  $lp_3$  and  $hp_3$  to generate the expansive DWT:  $lp_4$  and  $hp_4$  (each of length 20 samples).
2.  $lp_5$  and  $hp_5$  are generated by upsampling  $lp_4$  and  $hp_4$ .  $lp_5$  and  $hp_5$  each correspond to 40 samples.
3.  $lp_6$  and  $hp_6$  are the synthesis low and highpass filter outputs obtained by performing a 40-point circular convolution of the upsampled sequences ( $lp_5$  and  $hp_5$ ) and the synthesis filters ( $F(z)$  and  $G(z)$ ).
4. The  $lp_6$  and  $hp_6$  outputs are combined to generate  $\hat{X}$  that is *symmetric-periodic* of length 40. The unaliased samples of  $\hat{X}$  correspond to the original signal  $X$  and is obtained by a  $N$ -point windowing operation.

Periodic extension implementation as shown in Figure 2.20 follows the same procedure as the symmetric extension described above. However, we need not compute the regenerated coefficients since circular convolution operations in analysis and synthesis are equivalent to performing a periodic extension on the input signal.

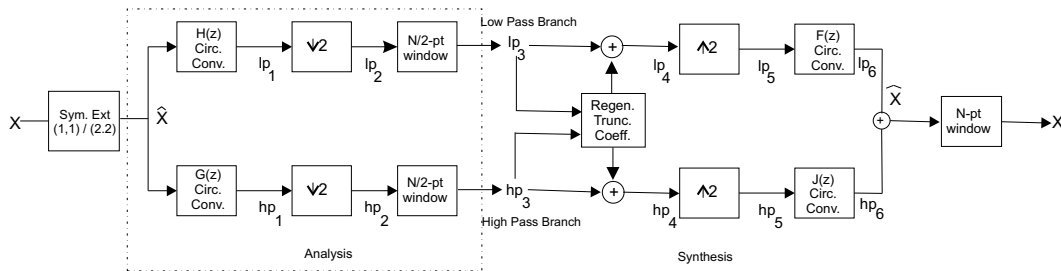


Figure 2.19: Block diagram of TDM method with symmetric extension

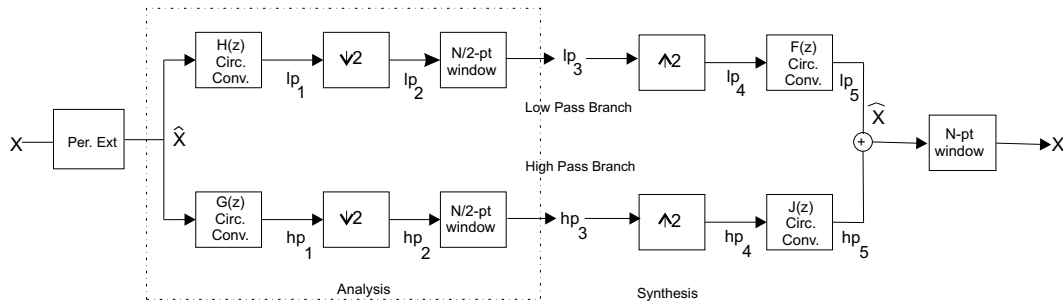


Figure 2.20: Block diagram of TDM method with periodic extension

#### 2.4.4 Comparison of FFT, TDC and TDM methods

- **Wavelet/extension type:**

Periodic extension for both orthogonal and biorthogonal wavelets can be implemented by all DWT computation methods. In the case of FFT and TDC methods, symmetric extension can only be implemented with biorthogonal filters that have symmetric filters. The extension type  $((1,1)/(2,2))$  to be followed for the input signal is decided by whether the filters are even or odd. In the case of TDM method, symmetric extension can be implemented for both orthogonal and biorthogonal wavelets. The extension type for the input does not depend on the filter length and can be either  $(1,1)$  or  $(2,2)$ .

- **Computation requirements:**

In the case TDC method, we observe that the length of the extended signal at the boundaries depend on the filter length ( $M/2 - 1$  for  $M$  even and  $(M - 1)/2$  for  $M$  odd). This differs from the FFT method where for symmetric extension, the entire signal is symmetrically extended resulting in an input signal length of  $2N - 2$  (odd length filters) or  $2N$  (even length filters). For an input of length  $N$  (assumed to be power of 2) and filter of length  $M$  (even), the number of multiplication and addition operations for performing a single filtering operation in TDC and TDM are as described below.

- TDC:  $M \times N$  real multiplications and  $(M - 1) \times N$  real additions.

- FFT:  $\frac{2N}{2}\log 2N$  (for obtaining the  $2N$ -point DFT of the input) +  $2N$  (multiplication of DFTs of input and filter) +  $\frac{2N}{2}\log 2N$  ( $2N$ -point IDFT of the result obtained from the multiplication of the input and the filter) complex multiplications and  $2 \times 2N\log 2N$  (for obtaining the  $2N$ -point DFT of the input) +  $2N - 1$  (multiplication of FFTs) +  $2N\log 2N$  ( $2N$ -point IDFT) complex additions. Therefore, we have  $2N\log 4N$  number of complex multiplications and  $4N\log 2\sqrt{2}N$  number of complex additions in total. We have assumed that the one-time computation of the DFT of the filter for a particular image size can be neglected.

It is to be noted that 1 complex multiplication is equivalent to 4 real multiplications and 1 complex addition is equivalent to 2 real addition operations. Thus, FFT method is computationally more intensive than the TDC method. The TDM method is equivalent to the TDC method in terms of computation. The TDM method also requires the computation of a matrix inverse for regenerating the discarded coefficients. However, the matrix inverse computation is an one-time calculation for a particular image size and hence can be neglected.

- **Symmetric extension:** It is not possible to implement symmetric extension with orthogonal wavelets using the FFT and TDC based methods. This is because the DWT coefficients for orthogonal wavelets do not show redundancy as in the case of linear phase filters. Thus, some (depends on filter length) DWT coefficients corresponding to the boundaries of the signals are discarded at the analysis stage to keep the process non-expansive. Recovering these discarded coefficients from the received coefficients is non trivial for TDC or FFT methods.

One drawback of the TDM method is that it requires the regenerating matrix,  $(\mathbf{A}_2 + \mathbf{A}_3\mathbf{E})(\mathbf{A}_0 + \mathbf{A}_1\mathbf{E})^{-1}$  to possess a low condition number for accurate signal reconstruction. Fortunately, this condition number constraint is satisfied by several combinations of wavelets and extension type. The condition numbers for symmetric extension for  $\text{LA}\perp$ ,  $\text{A}\perp$  and  $\text{bi}\perp$  wavelets is shown below. It can be observed that all  $\text{A}\perp$  and  $\text{D}_{7\text{LA}}$

have poor condition numbers. For periodic extension, the regenerating matrix for all the wavelets is perfectly conditioned (condition number is equal to 1).

Wavelet	Condition No.
D <sub>4LA</sub>	1.30
D <sub>5LA</sub>	1.59
D <sub>6LA</sub>	1.33
D <sub>7LA</sub>	9.62
D <sub>8LA</sub>	1.36
D <sub>9LA</sub>	1.66
D <sub>10LA</sub>	1.39
B <sub>9/7</sub>	1.11
D <sub>22/14</sub>	2.11

(a)LA $\perp$  and bi $\perp$ .

Wavelet	Condition No.
D <sub>4A</sub>	24.43
D <sub>5A</sub>	797.31
D <sub>6A</sub>	6237.92
D <sub>7A</sub>	1.26e+03
D <sub>8A</sub>	1.22e+06
D <sub>9A</sub>	1.12e+06
D <sub>10A</sub>	4.34e+07

(b)A $\perp$ .Table 2.2: Condition numbers for LA $\perp$ , bi $\perp$  and A $\perp$  filters.

## 2.5 Quantization

The set partitioning in hierarchical trees (SPIHT) [19] quantization scheme is used to generate all of the results in this thesis. SPIHT is an extension of the embedded zero tree wavelet (EZW) image coding technique introduced by Shapiro [20]. SPIHT achieves good performance by exploiting the spatial dependencies of the DWT coefficients in different subbands. The next two sections discuss the wavelet decomposition structure and the SPIHT coder.

### 2.5.1 SPIHT coder

The interband spatial dependencies are captured in the form of parent-child relationships; this is illustrated in Figure 2.21. The arrows in Figure 2.21 point from the parent node to its four children. With the exception of the coarsest subband and the finest subbands,

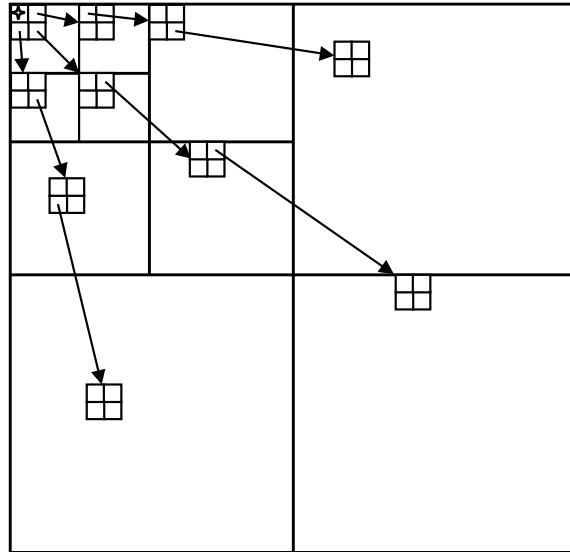


Figure 2.21: Parent-child relationships for a 3-level wavelet decomposition.

each DWT coefficient (parent) at the  $i^{\text{th}}$  level of decomposition is spatially correlated to 4 child coefficients at level  $i-1$  in the form of a  $2 \times 2$  block of adjacent pixels. These 4 child coefficients are at the same relative location in the subband decomposition structure. This relationship is utilized during SPIHT quantization: if a parent coefficient is insignificant with respect to a particular threshold, then all of its children would most likely be insignificant and similarly, significant coefficients in the finer subbands most likely correspond to a significant parent in the coarser subband. This results in significant savings: only the parent's position information needs to be coded since the children's coordinates can be inferred from the parent's position information.

SPIHT captures the current bit-plane information of all the DWT coefficients and organizes them into three ordered lists:

1. List of significant coefficients (LSC).
2. List of insignificant coefficients (LIC).
3. List of insignificant sets of coefficients (LIS).

LSC constitutes the coordinates of all coefficients that are significant. LIS contains the roots of insignificant sets of coefficient. They can be of two different types; the first type known as TYPE A has all the descendants insignificant within a given bit-plane, the second type known as TYPE B excludes the four children of the root node. Finally, LIC contains a list of all the coefficients that do not belong to either LIS or LSC and are insignificant. The operation of SPIHT can be grouped into three sequential steps: initialization, sorting pass (SP) and refinement pass (RP) & threshold update.

1. **Initialization:** The initial threshold is set to  $2^{\log_2(\max(|C_{i,j}|))}$ , where  $\max(|C_{i,j}|)$  is the largest DWT coefficient. The algorithm starts at the coarsest band in the subband pyramid. All the coefficients in the subband are added to the LIC and the coefficients with descendants (tree roots) are added as to LIS as TYPE A. Thus, during initialization, every coefficient is initialized to an insignificant state.
2. **Sorting pass:** At each threshold level, the LIC is coded first, followed by the entries in LIS. A given entry in LIC is tested and moved to LSC if found significant. The sign bit of the significant coefficient is also immediately coded. The LIS entries are coded differently. For a TYPE A LIS entries, if any member in the hierarchical tree is found significant, the immediate children are tested and are added to either LIC or LSC. The parent is added to the end of LIS as a TYPE B entry or removed from the LIS if it does not have any grandchildren. For TYPE B entries, if any member in the hierarchical tree is found significant, the immediate children are removed and added as TYPE A entries to the end of LIS. Processing continues till the end of LIS is reached. SP also records the position of the coefficients that are found significant during the current pass.
3. **Refinement pass and threshold update:** RP adds precision to the LSP entries obtained before the current sorting pass by outputting the most significant bit corresponding to the existing threshold. On completion of the refinement, the threshold is halved and the cycle is repeated starting from step 2.

# Chapter 3

## Wavelet properties

Wavelet properties important to image compression have been discussed in [5, 13, 15, 16, 24, 26]. In this section, we analyze six such properties: orthonormality, filter length, vanishing order, smoothness, filter magnitude response and group delay difference. We evaluate these properties for three types of wavelets: least asymmetric (LA) Daubechies orthogonal wavelets ( $D_{4LA}$  -  $D_{10LA}$ ), asymmetric (A) Daubechies orthogonal wavelets ( $D_{4A}$  -  $D_{10A}$ ), and biorthogonal wavelets ( $B_{9/7}$  and  $B_{22/14}$ ). It is to be noted that, in the discrete domain, wavelet characteristics correspond to the filter properties in the filter bank.

### 3.1 Orthonormality

Orthogonal filters lead to orthogonal wavelet basis functions; hence, the resulting wavelet transform is energy preserving. This implies that the mean square error (MSE) introduced during the quantization of the DWT coefficients is equal to the MSE in the reconstructed signal. This is desirable since it implies that the quantizer can be designed in the transform domain to take advantage of the wavelet decomposition structure. For orthogonal filter banks, the synthesis filters are transposes of analysis filters. However, in the case of

biorthogonal wavelets, the basis functions are not orthogonal and thus not energy preserving. Hence, we use the orthonormality parameter (OP) to measure the wavelet's deviation from orthonormality [13]. It is given by:

$$OP = \int_0^\pi (2 - O(\omega))^2 d\omega \quad (3.1)$$

where  $O(\omega)$  is the frequency response of the allpass filter defined by  $O(z) = H(z)H(z^{-1}) + G(z)G(z^{-1})$  ( $H$  and  $G$  are  $z$ -transforms of the lowpass and highpass analysis filters).

Table 4.7 presents the filter properties of 7 least asymmetric (LA) orthogonal Daubechies wavelets ( $D_{4LA}$  -  $D_{10LA}$ ) [3], corresponding asymmetric(A) orthogonal Daubechies wavelets ( $D_{4A}$  -  $D_{10A}$ ) [3] and 2 biorthogonal wavelets ( $B_{9/7}$ [3],  $B_{22/14}$ [27]). As expected, the orthonormality measure is zero for the orthogonal wavelets (LA and A), but greater than zero for the two biorthogonal wavelets ( $B_{9/7}$  and  $B_{22/14}$ ). However, both  $B_{9/7}$  and  $B_{22/14}$  are 'close' to orthonormal; thus, they preserve energy reasonably well in the DWT.

## 3.2 Filter length

Shorter synthesis basis functions are desired for minimizing distortion that affect the subjective quality of the image. Longer filters (that correspond to longer basis functions) are responsible for ringing noise in the reconstructed image at low bit rates. Table 4.7 depicts that  $D_{8A}$  -  $D_{10A}$ ,  $D_{8LA}$  -  $D_{10LA}$ ,  $B_{22/14}$  have the longer length synthesis filters while  $D_{4A}$  -  $D_{6A}$ ,  $D_{4LA}$  -  $D_{6LA}$ ,  $B_{9/7}$  have the shorter synthesis filters.

Table 3.1: Properties of the biorthogonal and orthogonal wavelets: orthonormality, filter length (analysis, synthesis), vanishing order (analysis), smoothness (synthesis), and group delay difference parameter.

Wavelets	Properties				
	OP	Length (A,S)	VO (A)	$S_{max}$	GDD
D <sub>4A</sub>	0	8,8	4	1.77	4.46
D <sub>4LA</sub>	0	8,8	4	1.77	0.46
D <sub>5A</sub>	0	10,10	5	2.10	8.05
D <sub>5LA</sub>	0	10,10	5	2.10	0.11
D <sub>6A</sub>	0	12,12	6	2.39	12.73
D <sub>6LA</sub>	0	12,12	6	2.39	0.48
D <sub>7A</sub>	0	14,14	7	2.66	18.50
D <sub>7LA</sub>	0	14,14	7	2.66	1.97
D <sub>8A</sub>	0	16,16	8	2.91	25.38
D <sub>8LA</sub>	0	16,16	8	2.91	0.50
D <sub>9A</sub>	0	18,18	9	3.16	33.45
D <sub>9LA</sub>	0	18,18	9	3.16	0.48
D <sub>10A</sub>	0	20,20	10	3.40	42.56
D <sub>10LA</sub>	0	20,20	10	3.40	0.53
B <sub>9/7</sub>	0.015	9,7	4	2.12	0
B <sub>22/14</sub>	0.011	22,14	5	3.16	0

### 3.3 Vanishing order, smoothness and magnitude response

#### 3.3.1 Vanishing order

Vanishing order (VO) is a measure of the compaction property of the wavelets [24]. It corresponds to the number of zeros ( $p$ ) at  $w = \pi$  for  $H(w)$ , the frequency response of the analysis lowpass filter. This means that the synthesis wavelet,  $\psi(t)$ , that is orthogonal to the analysis scaling functions has  $p$  vanishing moments. A VO of  $p$  means that polynomial

inputs  $1, \dots, t^{p-1}$  are preserved by the analysis lowpass filters and annihilated by the synthesis highpass filters.

$$\int t^m \psi(t) dt = 0, \quad 0 \leq m \leq p - 1. \quad (3.2)$$

In the case of orthogonal wavelets, the analysis wavelet function is same as the synthesis wavelet function ( $\tilde{\psi}(t) = \psi(t)$ ). Thus, the synthesis as well as the analysis wavelets have the same vanishing moment. However, for biorthogonal wavelets, the analysis wavelet function  $\tilde{\psi}(t)$  is different from the synthesis wavelet  $\psi(t)$ . Thus, the VO corresponds to  $p$  vanishing moments for synthesis wavelet  $\psi(t)$  only. A higher vanishing moment corresponds to better accuracy of approximation at a particular resolution [24]. Thus, the lowest frequency subband captures the input signal more accurately by concentrating a larger percentage of the image's energy in the LL subband. Table 4.7 shows the VO for LA $\perp$ , A $\perp$  and bi $\perp$  wavelets. It can be observed that the longer wavelets D<sub>8A</sub> - D<sub>10A</sub>, D<sub>8LA</sub> - D<sub>10LA</sub>, B<sub>22/14</sub> have higher VO than the shorter wavelets D<sub>4A</sub> - D<sub>6A</sub>, D<sub>4LA</sub> - D<sub>6LA</sub>, B<sub>9/7</sub>.

### 3.3.2 Smoothness

Non-smooth basis functions introduce artificial discontinuities under quantization [16]. These discontinuities are reflected as spurious artifacts in the reconstructed images. Smoothness of the synthesis scaling function is measured by the *Sobolev* exponent,  $S_{max}$  [24] and corresponds to the number of derivatives for  $\phi(t)$ . The asymptotic relation between  $S_{max}$  and VO ( $p$ ) for Daubechies filters is shown in equation (3.3) [6]. We observe from Table 4.7 that  $S_{max}$  increases as VO increases. It can be observed from Figures 3.1 - 3.4 that the scaling and wavelet functions for D<sub>10LA</sub> ( $S_{max} = 3.40$ ) are visually more smooth than D<sub>4LA</sub> ( $S_{max} = 1.77$ ).

$$S_{max} \approx 0.2075p + constant \quad (3.3)$$

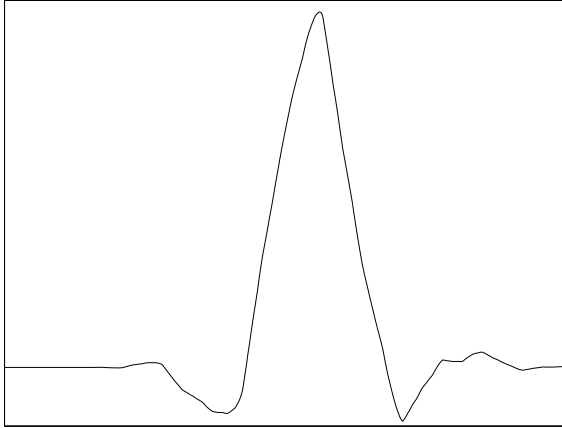


Figure 3.1: Scaling Function,  $\phi(t)$ ,  $D_{4LA}$ ,  
 $VO = 4$ ,  $S_{max} = 1.77$

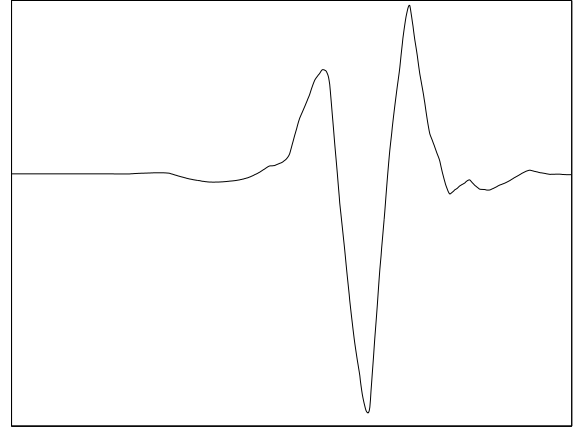


Figure 3.2: Wavelet Function,  $\psi(t)$ ,  $D_{4LA}$ ,  
 $VO = 4$ ,  $S_{max} = 1.77$

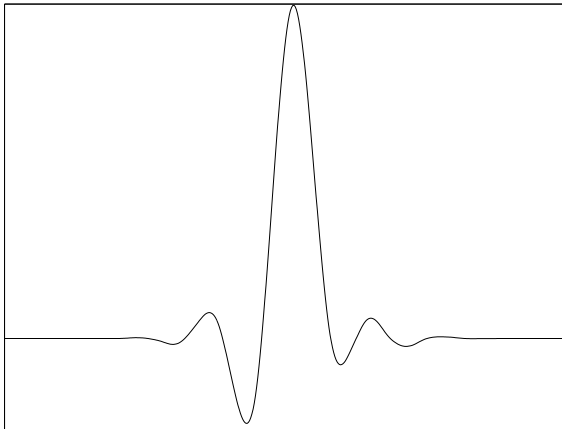


Figure 3.3: Scaling Function,  $\phi(t)$ ,  $D_{10LA}$ ,  
 $VO = 10$ ,  $S_{max} = 3.40$

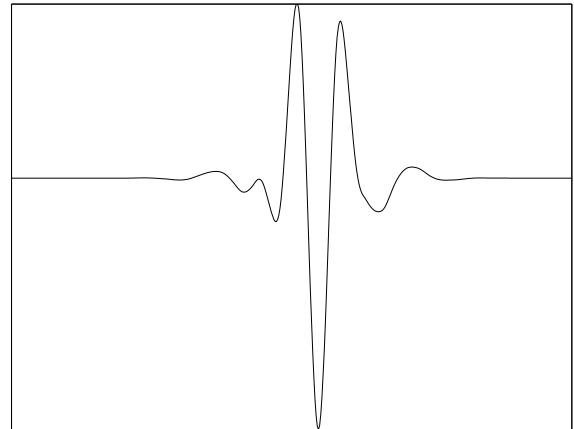


Figure 3.4: Wavelet Function,  $\psi(t)$ ,  $D_{10LA}$ ,  
 $VO = 10$ ,  $S_{max} = 3.40$

### 3.3.3 Magnitude response

Filter response is another critical property that affects the subjective quality of the reconstructed image. Wavelet filter bank characteristics important to image compression are discussed in [24]. Ideally, the lowpass filter response should decay smoothly to zero at  $\omega = \pi$  and the highpass filter response should decay smoothly to zero at  $\omega = 0$ . The filter responses approach the ideal (transition band width = 0 and more flat at  $\omega = \pi$  (lowpass) or  $\omega = 0$  (highpass)) rectangular response with the increase in the number of zeros. It is also to be noted that the number of zeros also correspond to the VO of the wavelet as discussed in section 3.3.1. A non-zero magnitude response at  $\omega = \pi$  for the lowpass filter ( $\omega = 0$  for the highpass filter) result in scaling (wavelet) functions that have sharp peaks and transitions. Reconstructed images for such scaling and wavelet functions depict checker boarding and tiling artifacts.

It can be observed from Table 4.7 that all the wavelets have VO of 4 or more; this indicates that there are at least four zeros at  $\omega = \pi$  ( $\omega = 0$ ) for the lowpass (highpass) filters. Figure 3.5 compares the magnitude response of  $D_{10LA}$  (solid lines) and  $D_{4LA}$  (dashed lines) filters. It can be observed that the passband edge (refer equation (3.4)) is at  $f_p = 0.25$  for both  $D_{10LA}$  and  $D_{4LA}$ . Although  $D_{10LA}$  and  $D_{4LA}$  share the same passband edge,  $D_{10LA}$  has a steeper transition band. The  $D_{10LA}$  lowpass and highpass magnitude responses are also more *flat* at  $\omega = \pi$  and  $\omega = 0$  due to their higher VOs. (Note: The magnitude responses of the  $LA \perp$  wavelets are identical to the corresponding  $A \perp$  wavelets.)

$$\begin{aligned} \frac{|H(\omega_p)|}{|H(\omega_0)|} &= \frac{1}{\sqrt{2}} \quad \text{lowpass, where } f_p \text{ is the passband edge frequency,} \\ \frac{|H(\omega_p)|}{|H(\omega_\pi)|} &= \frac{1}{\sqrt{2}} \quad \text{highpass, where } f_p \text{ is the passband edge frequency.} \end{aligned} \quad (3.4)$$

where  $H(\omega_p)$ ,  $H(\omega_0)$ , and  $H(\omega_\pi)$  correspond to the magnitude responses at passband edge frequency ( $\omega = p$ ),  $\omega = 0$  and  $\omega = \pi$  respectively. Figures 3.6 and 3.7 compare the magnitude

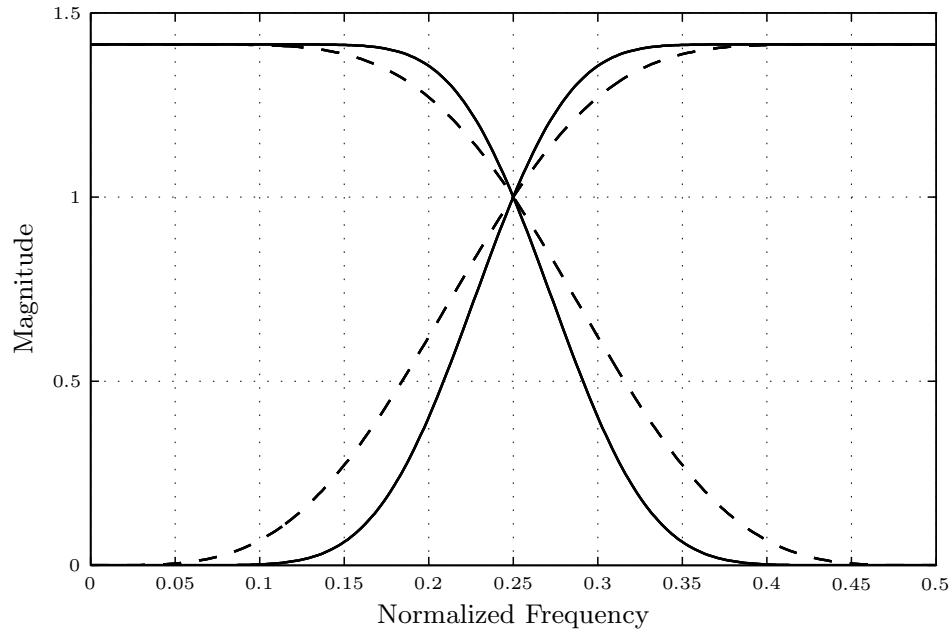


Figure 3.5: Magnitude response of the lowpass and highpass  $D_{10LA}$  (solid lines) and  $D_{4LA}$  (dashed lines) filters.

responses of orthogonal and biorthogonal filters that have similar length and  $S_{max}$  ( $B_{9/7}$  (solid lines) and  $D_{5LA}$  (dashed lines),  $B_{22/14}$  (solid lines) and  $D_{9LA}$  (dashed lines)). The passband edges of the lowpass biorthogonal filters ( $f = 0.272$  for both  $B_{9/7}$  and  $B_{22/14}$ ) extend beyond that of the lowpass orthogonal filters ( $f = 0.250$  for both  $D_{5LA}$  and  $D_{9LA}$ ). Thus, the biorthogonal wavelets will concentrate more energy in the lower frequency subbands than the orthogonal wavelets; this is especially true for low frequency images.

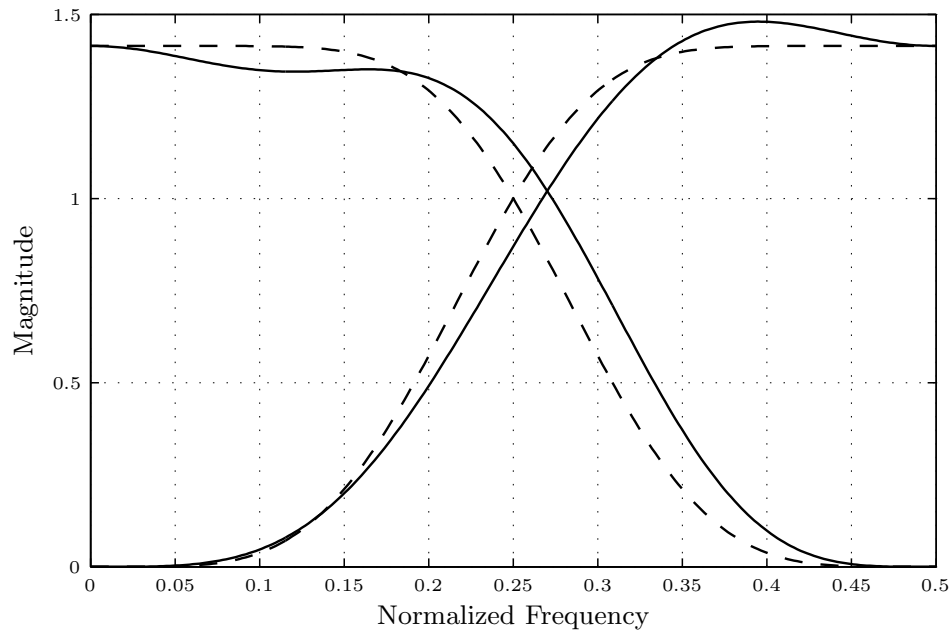


Figure 3.6: Magnitude response of the lowpass and highpass  $B_{9/7}$  (solid lines) and  $D_{5LA}$  (dashed lines) filters.

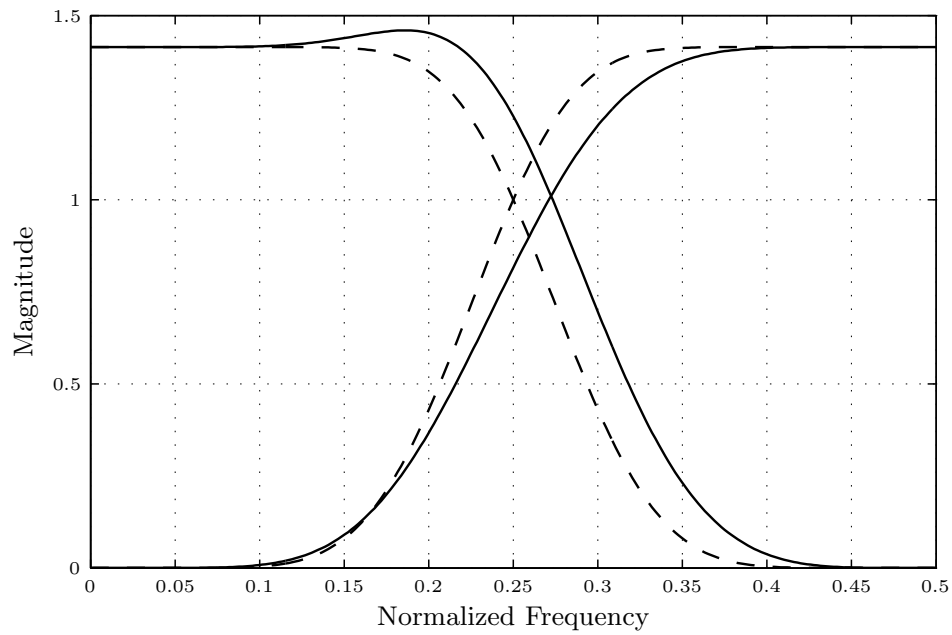


Figure 3.7: Magnitude response of the lowpass and highpass  $B_{22/14}$  (solid lines) and  $D_{9LA}$  (dashed lines) filters.

### 3.4 Group delay difference

Group delay difference (GDD) measures the deviation in group delay of the orthogonal wavelets from the linear phase group delay. GDD is calculated as the mean-squared-error of the filter's actual group delay from the ideal group delay in the passband defined as in equation (3.4). The ideal group delay for filter of length  $M$  is  $\frac{M-1}{2}$ . For orthogonal wavelets, GDD is the same for both lowpass and highpass filters. As expected, the symmetric biorthogonal wavelets have zero GDD while the LA orthogonal wavelets exhibit small GDD.

Non-zero GDD introduces a phase distortion that impacts encoding and decoding by altering the DWT subband structure. Figures 3.8 - 3.11 show an original image and its 2-level decomposition using  $D_{9LA}$ ,  $D_{9A}$  and  $B_{22/14}$ . As discussed in Section 2.2.5, the DWT results in a self-similar, hierarchical subband structure: the location of significant coefficients in the finer subbands correspond to the same relative position of the significant coefficients in coarser subbands. This is true only when the filters have constant group delay (GDD = 0) as observed in the case of biorthogonal wavelets (Figure 3.11). It is to be noted that the color gray corresponds to zero in Figures 3.8-3.11 while black and white correspond to high negative or positive values. For orthogonal wavelets, GDD > 0 results in different delays for different subbands. Figures 3.12 and 3.13 compare the passband group delay for the low and highpass filters of  $D_{9LA}$  (solid) and  $D_{9A}$  (dashed) with the ideal group delay (dotted). For the asymmetric wavelet  $D_{9A}$ , with a large GDD of 33.45, the significant coefficients in finer subbands suffer large offsets (Figure 3.10) unlike the significant coefficients for biorthogonal wavelet that has GDD = 0 (Figure 3.11).

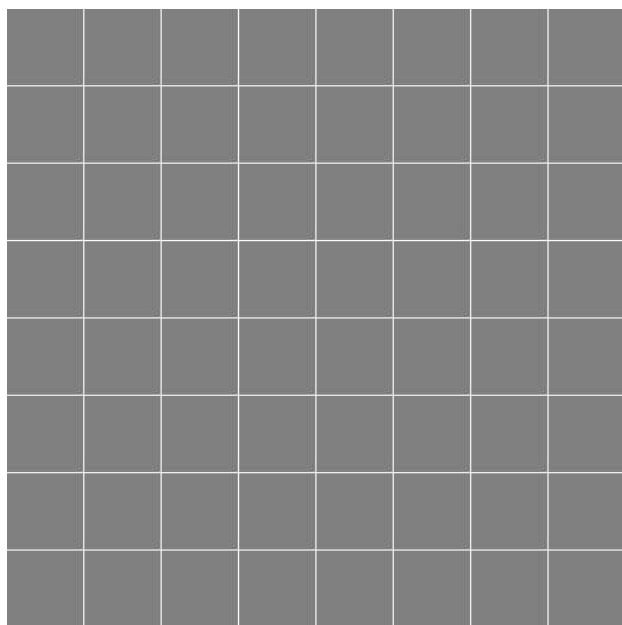


Figure 3.8: Original Image

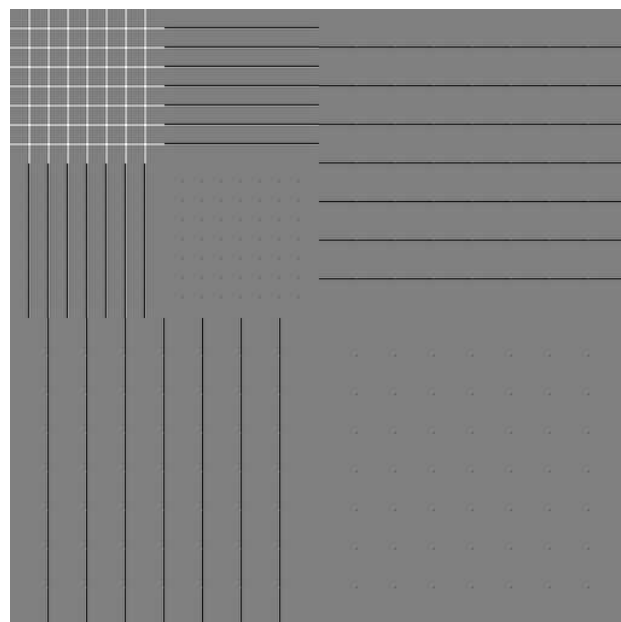


Figure 3.9: 1-level, 2D DWT of original image using  $D_{9LA}$ .

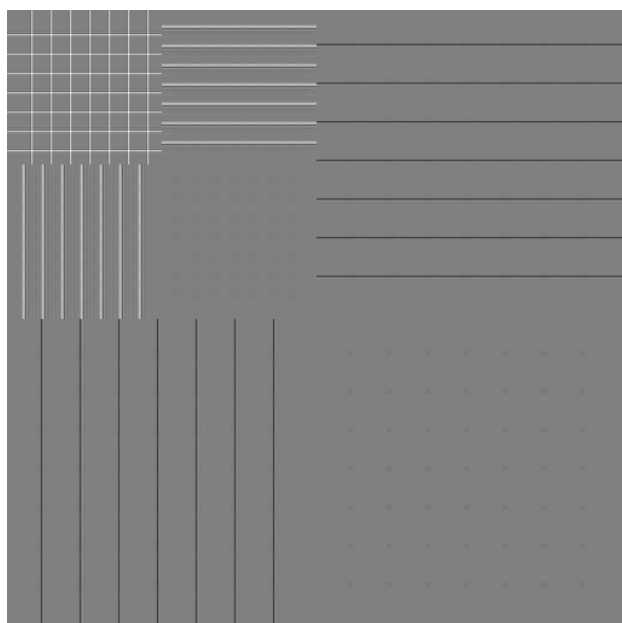


Figure 3.10: 1-level, 2D DWT of original image using  $D_A$ .

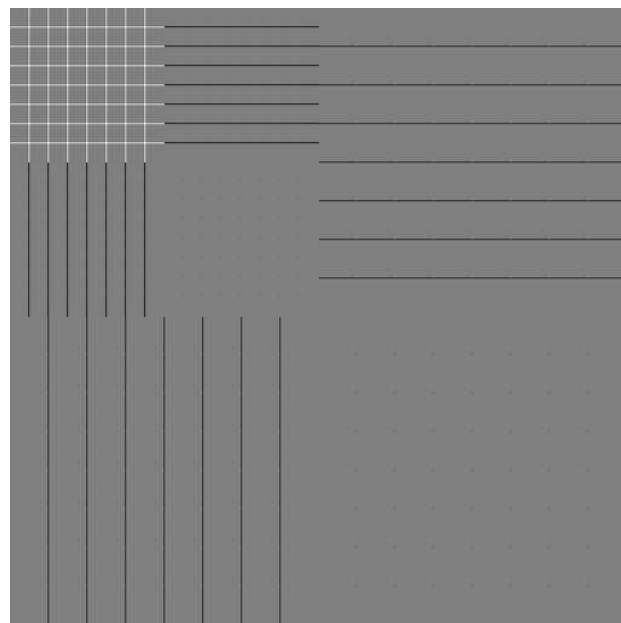


Figure 3.11: 1-level, 2D DWT of original image using  $B_{22/14}$ .

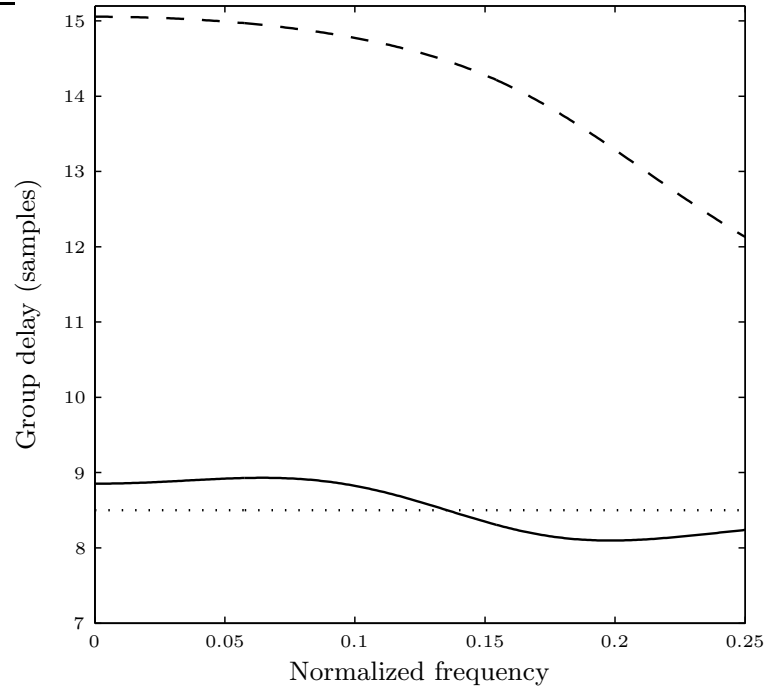


Figure 3.12: Group delay for LP filters:  $D_{9LA}$  (solid),  $D_{9A}$  (dashed) and ideal (dotted) in the passband.

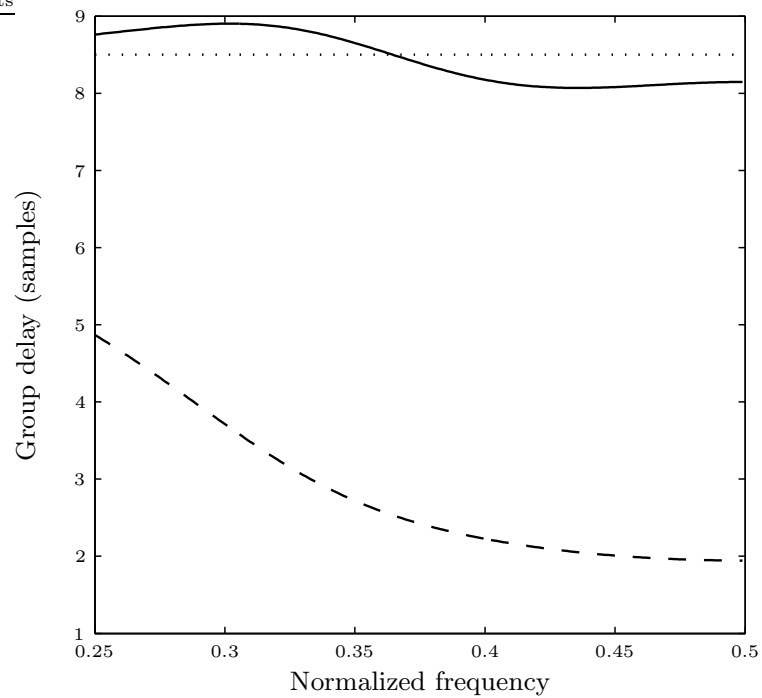


Figure 3.13: Group delay plots for HP filters:  $D_{9LA}$  (solid),  $D_{9A}$  (dashed) and ideal (dotted) in the passband.

# Chapter 4

## Performance analysis and results

The results presented in this thesis compare the image compression performance of periodic and symmetric extension techniques using the TDM non-expansive DWT method. A 5-level DWT decomposition is followed by SPIHT quantization. Both objective as well as subjective performance of the compressed images are evaluated. The objective performance is measured by peak signal-to-noise-ratio (PSNR) of the reconstructed image  $\tilde{x}$ . PSNR measured in decibels (dB) is given by:

$$PSNR = 10 \log_{10} \left( \frac{255^2}{MSE} \right), \quad (4.1)$$

where the value 255 is the maximum possible value that can be attained by the image signal. Mean square error (MSE) is defined as

$$MSE = \frac{1}{MN} \sum_{m=0}^{M-1} \sum_{n=0}^{N-1} |x(m, n) - \tilde{x}(m, n)|^2, \text{ where } M \times N \text{ is the size of the original image.} \quad (4.2)$$

PSNR is measured in decibels(dB). It has been shown that PSNR is not always a indicator of the subjective quality of the reconstructed image [24]. We also evaluate the subjective performance by visible artifacts in the reconstructed image.

## 4.1 Choice of wavelets and images

We employ 7 LA orthogonal Daubechies wavelets ( $D_{4LA}$  -  $D_{10LA}$ ) [3], 7 (A) orthogonal Daubechies wavelets ( $D_{4A}$  -  $D_{10A}$ ) [3] and 2 biorthogonal wavelets ( $B_{9/7}$  [3],  $B_{22/14}$  [27]). It has been shown in Chapter 3 (Table 4.7) that the least asymmetric wavelets and the corresponding asymmetric wavelets differ only in the GDD parameter. Hence, by performance comparison of LA and A wavelets, we illustrate the importance of linear phase on compression performance. We then chose the best performing orthogonal wavelets and compare their compression performance against similar biorthogonal wavelets when both use symmetric extension.

The compression performance is evaluated for twelve grayscale images that can be grouped into three image types: four low frequency (LF) (*Lena*, *Peppers*, *Boat*, *Goldhill*), four medium frequency (MF) (*Barbara*, *Lighthouse*, *Nitf7*, *House*), four high frequency (HF) (*Satellite*, *Mandrill*, *Grass*, *SanDiego*) images. The frequency type groups are based on the percentage of total image energy (96% - 100% LF, 92% - 96% MF and  $\leq 92\%$  HF) in the LL subband obtained after one level of decomposition using the  $B_{9/7}$  wavelet. The distribution of energy for the twelve images is given in Table 4.1.

## 4.2 Test conditions

The results are organized as follows. Section 4.3.1 presents the PSNR results for LA  $\perp$ , A $\perp$ , and bi $\perp$  wavelets using the periodic extension technique. This is done for all three image types at four compression ratios (8:1, 16:1, 32:1, and 64:1). Section 4.3.2 presents the symmetric extension PSNR results for LA  $\perp$  and bi $\perp$  wavelets that have low condition numbers. Section 4.4.1 compares the performance of near-linear phase wavelets (LA  $\perp$ ) to non-linear phase wavelets (A  $\perp$ ) using periodic extension technique. In Section 4.4.3, extensive analysis of symmetric and periodic extension for biorthogonal (bi $\perp$ ) and  $\perp$  wavelets. Section 4.4.4

Table 4.1: Percentage energy distribution after 1-level of decomposition using the  $B_{9/7}$  wavelet.

Image Type	Image	Subbands			
		LL	LH	HL	HH
Low frequency	<i>Lena</i>	99.2402	0.4734	0.1901	0.0964
	<i>Peppers</i>	99.2582	0.3347	0.2787	0.1284
	<i>Boat</i>	98.6573	1.0110	0.2495	0.0822
	<i>Goldhill</i>	98.6162	0.7221	0.5290	0.1328
Medium frequency	<i>Barbara</i>	95.1036	4.1602	0.3308	0.4054
	<i>Lighthouse</i>	95.8747	2.2305	1.7046	0.1902
	<i>House</i>	94.7955	2.4787	2.4906	0.2352
	<i>Nitf7</i>	94.0581	2.5215	2.5581	0.8623
High frequency	<i>Satellite</i>	87.8758	5.1434	4.8395	2.1413
	<i>Mandrill</i>	86.4593	2.8193	9.1289	1.5925
	<i>Grass</i>	87.9973	7.1446	3.9735	0.8846
	<i>SanDiego</i>	90.5299	3.7452	4.5237	1.2011

compares the performance of the least asymmetric  $\perp$  wavelets and similar bi $\perp$  wavelets when they both employ symmetric extension. We perform subjective evaluation of reconstructed images in Section 4.5. Comparison with previous work in Section 4.6.

## 4.3 PSNR results

### 4.3.1 Results for periodic extension

This section presents the image compression performance of orthogonal as well as biorthogonal wavelets for periodic extension. The PSNR results are computed for three image types (LF, MF, and HF) at four CRs (8:1, 16:1, 32:1, and 64:1). The PSNRs for an image at each CR is shown relative to the PSNR value of  $D_{4LA}$  at that CR. “+” indicates that the PSNR for the wavelet/CR combination is more than the PSNR value of the  $D_{4LA}$  while “-” sign indicate that the PSNR for the wavelet/CR combination is lower than the PSNR value of

Table 4.2: MSE introduced by SPIHT for 2-level decomposition for the test image shown in Figure 3.8

CR	$D_{9A}$	$D_{9LA}$	$B_{22/14}$
8:1	0.361	0.364	0.214
16:1	6.880	6.624	3.215
32:1	47.069	45.686	33.923
64:1	223.235	183.831	198.788

the  $D_{4LA}$  at that particular CR.

#### 4.3.1.1 Low frequency images

Tables A.1 and A.2 in Appendix A show the PSNR results for four LF images (*Lena*, *Peppers*, *Boat* and *Goldhill*). Longer wavelets ( $D_9$ s and  $B_{22/14}$ ) as expected perform better than the shorter wavelets ( $D_4$ s and  $D_5$ s) due to their VOs. However, the performance gain for longer wavelets over shorter wavelets varies with wavelet type. The gain is high for  $LA\perp$  ( $\approx 0.20dB$ ) and  $bi\perp$  ( $\approx 0.10dB$ ) wavelets while it is negligible for  $A\perp$  wavelets. We also observe that the  $LA\perp$  wavelets, in general, perform better than the corresponding asymmetric( $A\perp$ ). This can be attributed to the lower GDD for  $LA\perp$  wavelets. Note that higher GDD corresponds to larger offsets suffered by significant coefficients in the finer subbands; this affects SPIHT encoding since significant children now correspond to insignificant parents. Thus, SPIHT requires more bits to achieve the same mean square error (MSE) for an  $A\perp$  wavelet compared to the  $LA\perp$  and  $bi\perp$  wavelets. This can be observed in Table 4.2 which presents MSE for the test image of Figure 3.8 (for  $LA\perp$  ( $D_{9LA}$ ),  $A\perp$  ( $D_{9A}$ ) and  $bi\perp$  ( $B_{22/14}$ )) for a 2-level decomposition.  $B_{22/14}$  and  $D_{9LA}$  are the best performing wavelets among biorthogonal and orthogonal wavelets.

### 4.3.1.2 Medium frequency images

PSNR results for the four MF (*Barbara*, *Lighthouse*, *House* and *Nitf7*) images are shown in Tables A.3 and A.4 in Appendix A. Similar to LF images, longer wavelets outperform shorter wavelets for LA $\perp$  and bi $\perp$  wavelets. In the case of A $\perp$  wavelets, PSNR decreases for longer wavelets for all images except *Barbara*. The bi $\perp$  wavelets, in general, perform better than the  $\perp$  wavelets.

### 4.3.1.3 High frequency images

Tables A.5 and A.6 show the PSNR results for the four HF images (*Satellite*, *Mandrill*, *Grass* and *SanDiego*) in Appendix A. For HF images, shorter wavelets perform nearly as well as longer wavelets (PSNR difference  $\leq 0.1$  dB). The bi $\perp$  wavelets and the  $\perp$  wavelets deliver similar PSNR performance at high CRs.

## 4.3.2 Results for symmetric extension

This section presents the PSNR results for both LA $\perp$  and bi $\perp$  wavelets with symmetric extension. It is to be noted that symmetric extension cannot be implemented for A $\perp$  wavelets using the TDM method due to the poor condition number of the regenerating matrix (equation (2.20)). Six LA $\perp$  wavelets ( $D_{4LA}$ ,  $D_{5LA}$ ,  $D_{6LA}$ ,  $D_{8LA}$ ,  $D_{9LA}$ ,  $D_{10LA}$ ) and two bi $\perp$  wavelets ( $B_{9/7}$  and  $B_{22/14}$ ) have been used for the results. The PSNR results at four CRs (8:1, 16:1, 32:1, and 64:1) are grouped based on the image type. For an image, the PSNRs for different wavelets are shown relative to the PSNR value of  $D_{4LA}$  at each CR. “+” indicates that the PSNR for the wavelet/CR combination is greater than the PSNR value of the  $D_{4LA}$  while “-” sign indicate that the PSNR for the wavelet/CR combination is smaller than the PSNR value of the  $D_{4LA}$  at that particular CR. The highest PSNR value for a given CR and image is boldfaced.

#### 4.3.2.1 Low frequency images

Tables B.1 in Appendix B shows the PSNR results for four LF images (*Lena*, *Peppers*, *Boat* and *Goldhill*). It can be observed that  $B_{22/14}$  is the best performing wavelets for all CRs and all images.  $D_{9LA}$  /  $D_{10LA}$  is the best performing  $LA\perp$  wavelet. It is also observed that the PSNR gain increases with increase in the length of the wavelet. This can be attributed to their higher VOs (Table 4.7). The difference in PSNR between the best performing  $bi\perp$  wavelet and  $LA\perp$  is 0.1~0.25dB for *Lena* and *Goldhill* and 0.2~0.34dB for *Peppers* and *Boat*.

#### 4.3.2.2 Medium frequency images

Table B.2 in Appendix B shows the PSNR results for MF images (*Barbara*, *Lighthouse*, *House* and *Nitf7*). It is observed that  $D_{8LA}$  and  $D_{9LA}$  are the best performing wavelets.  $B_{22/14}$  performs better than  $B_{9/7}$ . The PSNR gain increases with increase in length of wavelets for both  $LA\perp$  and  $bi\perp$  wavelets. The best performing  $\perp$  wavelet outperforms the best  $bi\perp$  wavelet by about 0~0.1dB.

#### 4.3.2.3 High frequency images

Table B.3 in Appendix B shows the PSNR results for HF images (*Satellite*, *Mandrill*, *Grass* and *SanDiego*). It can be observed that  $D_{9LA}$  and  $D_{10LA}$  are the best performing  $\perp$  wavelets.  $B_{22/14}$  is the best performing  $bi\perp$  wavelet. The  $bi\perp$  wavelets give better PSNR performance than  $\perp$  wavelet in general; the average gain being between -0.02~0.1dB. The same trend of longer wavelets outperforming shorter wavelets as in LF and MF images is also observed.

## 4.4 Analysis of PSNR results

A detailed analysis of the results presented in Appendix A and Appendix B is the subject of this section; it is divided into three subsections. For periodic extension, Section 4.4.1 demonstrates the importance of linear phase and explains why  $LA\perp$  wavelets perform better than the  $A\perp$  wavelets. Section 4.4.2 compares the periodic and the symmetric extension techniques. Lastly, for symmetric extension, Section 4.4.3 compares the compression performance of orthogonal wavelets with biorthogonal wavelets that have similar properties.

### 4.4.1 Least asymmetric wavelets vs. asymmetric wavelets

This section compares the performance of the least asymmetric ( $LA$ )  $\perp$  Daubechies wavelets and asymmetric ( $A$ )  $\perp$  Daubechies wavelets for periodic extension. This comparison isolates the impact of linear phase filters on image compression performance. Although perfect reconstruction can be achieved with either linear or non-linear phase filters, the effect of phase distortion becomes critical under quantization. It is to be noted that previous literature [7, 8, 12, 13, 23] comparing the image compression performance for different wavelets have not compared the performance of  $LA\perp$  wavelets with  $A\perp$  wavelets.

The PSNR results shown in Table 4.3 have been extracted from the Tables A.1 - A.6 by averaging the data for an image type, for a given wavelet. Seven  $LA\perp$  wavelets,  $D_{4LA}$  -  $D_{10LA}$  and the corresponding seven  $A\perp$  wavelets,  $D_{4A}$  -  $D_{10A}$  are compared. The compression performance at four CRs (8:1, 16:1, 32:1 and 64:1) for twelve grayscale images was computed: four LF (*Lena*, *Peppers*, *Boat*, *Goldhill*), four MF (*Barbara*, *Lighthouse*, *Nitf7*, *House*) and four HF (*SanDiego*, *Mandrill*, *Satellite*, *Grass*).

Table 4.3 shows the average PSNR improvement for  $LA\perp$  wavelets over the  $A\perp$  wavelets for an image type. The results indicate that  $LA\perp$  wavelets significantly outperform  $A\perp$  wavelets for LF and MF images at all compression ratios (PSNR differences  $\geq 0.1$ dB are considered significant). A significant improvement is also realized for high frequency (HF) images at

most compression ratios with the longer filters. It is also interesting to note that, in general, the PSNR gain increases for the longer filters ( $D_{9LA} - D_{9A}$ ,  $D_{10LA} - D_{10A}$ ). Moreover, for LF images, the performance improvement increases as the amount of compression increases.

Table 4.7 depicts that the  $A_{\perp}$  wavelets differ from the  $LA_{\perp}$  wavelets only in their group delay difference (GDD) parameter; all other filter properties critical to compression (orthogonality, filter length, VO, smoothness) are identical. Table 4.4 shows the difference ( $A_{\perp} - LA_{\perp}$ ) in MSE introduced by SPIHT for 1 LF image (*Lena*), 1 MF image (*Barbara*) and 1 HF image (*Mandrill*); this illustrates the effect of phase distortion on MSE introduced by SPIHT after five levels of decomposition. MSE is computed from the DWT coefficients before and after SPIHT quantization. Positive entries indicate that MSE for  $LA_{\perp}$  is lower than the corresponding  $A_{\perp}$  wavelet. The column corresponding to “Compaction gain” computes the percentage difference in image energy ( $A_{\perp} - LA_{\perp}$ ) for the lowest frequency subband after five levels of decomposition. Positive entries indicate that  $A_{\perp}$  wavelets have higher compaction ability than the corresponding  $LA_{\perp}$  wavelet. It is observed that, although  $A_{\perp}$  wavelets possess higher compaction ability,  $LA_{\perp}$  introduce lower MSE at the end of SPIHT encoding. Since the wavelets vary only in their GDD parameter, it can be inferred that variable group delay results in different delays for different frequency subbands. This variable delay shifts the spatial position of the children with respect to its parent coefficients thereby adversely affecting the hierarchical wavelet decomposition structure (Section 2.5). As a result of the spatial shift, significant coefficients (children) at higher resolutions correspond to insignificant parents at coarser resolution. This leads to the addition of more number of coefficients into the list-of-insignificant-coefficients during SPIHT encoding that require allocation of extra bits during the next sorting pass. Thus, fewer bits are available to code significant coefficients there by increasing the MSE. It can also be noted that, in general, MSE gain for  $LA_{\perp}$  wavelets increase with filter length and with increase in compression which explains why PSNR gain increases for longer filters.

Table 4.3: PSNR difference (in dB) between LA $\perp$  and the corresponding A $\perp$  wavelet. A positive entry indicates LA $\perp$  perform better than A $\perp$  wavelets. A negative entry indicates LA $\perp$  perform worse than A $\perp$  wavelets.

Image Type	Wavelets	Compression Ratios			
		8:1	16:1	32:1	64:1
LF Images	D <sub>4LA</sub> -D <sub>4A</sub>	0.045	0.048	0.092	0.085
	D <sub>5LA</sub> -D <sub>5A</sub>	0.137	0.150	0.217	0.285
	D <sub>6LA</sub> -D <sub>6A</sub>	0.162	0.203	0.252	0.238
	D <sub>7LA</sub> -D <sub>7A</sub>	0.172	0.208	0.282	0.320
	D <sub>8LA</sub> -D <sub>8A</sub>	0.235	0.315	0.377	0.343
	D <sub>9LA</sub> -D <sub>9A</sub>	0.310	0.385	0.513	0.517
	D <sub>10LA</sub> -D <sub>10A</sub>	0.308	0.358	0.425	0.413
MF Images	D <sub>4LA</sub> -D <sub>4A</sub>	0.168	0.138	0.072	0.027
	D <sub>5LA</sub> -D <sub>5A</sub>	0.170	0.163	0.208	0.180
	D <sub>6LA</sub> -D <sub>6A</sub>	0.285	0.223	0.168	0.130
	D <sub>7LA</sub> -D <sub>7A</sub>	0.322	0.275	0.230	0.153
	D <sub>8LA</sub> -D <sub>8A</sub>	0.378	0.310	0.253	0.192
	D <sub>9LA</sub> -D <sub>9A</sub>	0.393	0.372	0.340	0.275
	D <sub>10LA</sub> -D <sub>10A</sub>	0.440	0.380	0.303	0.173
HF Images	D <sub>4LA</sub> -D <sub>4A</sub>	0.008	-0.013	-0.005	-0.007
	D <sub>5LA</sub> -D <sub>5A</sub>	0.087	0.065	0.065	0.045
	D <sub>6LA</sub> -D <sub>6A</sub>	0.060	0.043	0.040	0.020
	D <sub>7LA</sub> -D <sub>7A</sub>	0.075	0.060	0.057	0.030
	D <sub>8LA</sub> -D <sub>8A</sub>	0.097	0.080	0.072	0.045
	D <sub>9LA</sub> -D <sub>9A</sub>	0.128	0.110	0.100	0.077
	D <sub>10LA</sub> -D <sub>10A</sub>	0.125	0.087	0.070	0.032

Table 4.4: SPIHT MSE Comparison

Image	Wavelets	Compaction gain ( $A_{\perp} - LA_{\perp}$ )	MSE ( $A_{\perp} - LA_{\perp}$ ) at CA			
			8:1	16:1	32:1	64:1
Lena	$D_{4LA}/D_{4A}$	4.207	-0.001	-0.002	0.335	0.794
	$D_{5LA}/D_{5A}$	1.401	0.126	0.553	2.053	5.106
	$D_{6LA}/D_{6A}$	-0.166	0.182	0.621	1.496	1.838
	$D_{7LA}/D_{7A}$	-2.984	0.176	0.627	2.078	4.751
	$D_{8LA}/D_{8A}$	4.374	0.308	1.188	3.281	6.280
	$D_{9LA}/D_{9A}$	-0.794	0.388	1.473	3.914	7.426
	$D_{10LA}/D_{10A}$	-0.146	0.308	1.060	3.319	6.036
Barbara	$D_{4LA}/D_{4A}$	1.729	-0.014	0.011	-1.651	-1.526
	$D_{5LA}/D_{5A}$	0.406	0.700	2.293	8.626	9.156
	$D_{6LA}/D_{6A}$	0.796	0.653	1.884	1.695	1.624
	$D_{7LA}/D_{7A}$	-1.322	0.726	2.329	3.588	1.250
	$D_{8LA}/D_{8A}$	1.425	1.135	3.440	5.080	5.267
	$D_{9LA}/D_{9A}$	1.005	1.141	4.824	9.111	9.593
	$D_{10LA}/D_{10A}$	0.609	0.917	3.694	4.378	0.484
Mandrill	$D_{4LA}/D_{4A}$	0.384	0.292	-0.264	1.453	0.442
	$D_{5LA}/D_{5A}$	-0.113	2.328	4.775	3.432	3.961
	$D_{6LA}/D_{6A}$	-0.012	1.583	2.829	4.037	4.683
	$D_{7LA}/D_{7A}$	-0.050	1.660	5.671	9.492	5.691
	$D_{8LA}/D_{8A}$	0.052	2.217	3.289	7.695	8.120
	$D_{9LA}/D_{9A}$	-0.061	2.767	6.692	7.982	9.973
	$D_{10LA}/D_{10A}$	0.124	2.752	6.802	10.462	7.550

#### 4.4.2 Periodic extension vs. symmetric extension

This section discusses why symmetric extension performs better than periodic extension for both orthogonal and biorthogonal wavelets. The TDM method provides a common platform for comparison of both extension techniques. We have selected six LA  $\perp$  wavelets and two bi $\perp$  wavelets that possess low condition numbers for the synthesis regenerating matrix for comparison. The compression performance at four compression ratios of twelve grayscale images is shown in Table 4.5. The results shown in Table 4.5 are obtained by averaging the results for a wavelet and image type to produce one overall bi $\perp$  and one overall  $\perp$  result for a given CR.

Table 4.5 depicts that symmetric extension performs significantly better than periodic extension for both bi $\perp$  and  $\perp$  wavelets for LF and MF images at all CRs. Further examination of these results leads to four important insights.



Figure 4.1: Original image *House256*.



Figure 4.2: *House256* , Symmetric extension, 32:1, PSNR = 27.37 dB.



Figure 4.3: *House256* , Periodic extension, 32:1, PSNR = 26.89 dB.

First, the performance gain of symmetric extension over periodic extension is proportional to the degree of discontinuity introduced at the border when the image is extended. To illustrate this effect, one MF image *house256* with dissimilar borders is considered (CR: 32:1). Figures 4.1 - 4.3 show the original and compressed *house256* images for both type of extension techniques using  $D_{9LA}$ . For images with similar borders, symmetric extension and periodic extension will generate similar border extensions; thus, the PSNR gain for symmetric extension is expected to be less than the average gain for such images at a particular CR. However, for images with dissimilar borders, the symmetric extension advantage is expected to be larger than average. For example, the PSNR improvement (0.48dB) of symmetric over periodic extension for House (dissimilar borders) is higher than the average PSNR gain ( $\sim 0.14$ dB) for MF images at 32:1. This effect is seen for both  $bi\perp$  and  $\perp$  wavelets. Moreover, subjectively, the reconstructed image using periodic extension shows a lot of ringing at the boundaries compared to the reconstructed image using symmetric extension.

Table 4.5: Average PSNR improvement (in dB) of symmetric extension over periodic extension for  $bi\perp$  and  $\perp$  wavelets.

Image Type	Wavelet	Compression Ratio			
		8:1	16:1	32:1	64:1
Low Frequency	Biorthogonal	0.1638	0.2188	0.3163	0.3475
	Orthogonal	0.1721	0.2346	0.3146	0.3525
Medium Frequency	Biorthogonal	0.1150	0.1550	0.1450	0.1525
	Orthogonal	0.1158	0.1388	0.1442	0.1496
High Frequency	Biorthogonal	0.0088	0.0163	0.0188	0.0125
	Orthogonal	0.0133	0.0162	0.0125	0.0104

Second, the average performance improvement of symmetric extension varies with image type (for both  $bi\perp$  and  $\perp$  wavelets). Table 4.5 illustrates that the performance gain is highest for LF images ( $\sim 0.3$ dB at 32:1) and decreases for MF ( $\sim 0.14$ dB at 32:1) and HF images ( $\sim 0.02$ dB at 32:1). For HF images, it is more likely that adjacent pixels are different; thus, symmetric extension and periodic extension typically result in similar border extensions. However, for LF images, it is more likely that adjacent pixels are similar; thus,

periodic extension, in general, introduces more discontinuities at the borders than symmetric extension.

Third, the performance gain of symmetric extension over periodic extension increases with increasing compression for LF images (for both  $\text{bi}\perp$  and  $\perp$  wavelets). This is because border discontinuities introduced by periodic extension generate high frequency artifacts that artificially increase the energy in the high frequency subbands; consequently, the energy in the low frequency subbands is decreased. The image energy in the low frequency subband for symmetric extension and periodic extension for three image types (LF, MF and HF) are shown in Table 4.6. For a given wavelet, the entries in Table 4.6 are generated by averaging the values for a particular image type after 5-level decomposition. In all cases, but one (HF -  $\text{D}_{9LA}$ ), periodic extension results in less energy in the lowest frequency subband compared to symmetric extension. Higher number of significant coefficients in the finer subbands deteriorates compression performance by degrading the efficiency of the SPIHT coder.

Table 4.6: Percentage of energy in the lowest frequency subband after a 5-level decomposition.

Wavelet	Low Frequency		Medium Frequency		High Frequency	
	SymEx	PerEx	SymEx	PerEx	SymEx	PerEx
$\text{D}_{4LA}$	72.47	69.96	61.15	58.02	35.68	33.91
$\text{D}_{5LA}$	73.77	72.20	60.87	58.97	34.67	34.07
$\text{D}_{6LA}$	72.89	70.37	61.08	58.10	35.38	34.06
$\text{D}_{8LA}$	73.97	70.75	59.73	58.16	34.27	34.14
$\text{D}_{9LA}$	73.64	72.32	59.72	59.42	33.62	34.09
$\text{D}_{10LA}$	73.34	70.96	60.92	58.25	35.02	34.16
$\text{B}_{9/7}$	75.46	72.58	60.47	59.33	34.87	34.63
$\text{B}_{22/14}$	74.68	73.09	60.73	59.38	33.89	33.40

When a wavelet/extension combination concentrates more energy in the lower frequency subbands, SPIHT requires fewer bits to capture the same amount of information (i.e. same mean square error(MSE)) than a wavelet/extension combination that concentrates less en-

ergy in the same low frequency subbands. There are two reasons for this. (i) In SPIHT, a greater concentration of energy in the low frequency subbands means significant coefficients occur higher in the subband pyramid; in other words, fewer bits are required to encode the position of the significant coefficient during the sorting pass. This is because SPIHT encoding starts at the top with the coarsest subband. The position and magnitude of the insignificant coefficients are encoded by only encoding the root node that occurs higher (requires fewer bits) in the subband pyramid. (ii) When energy is spread throughout the higher frequency subbands, the significant coefficients (at each threshold level) occur ‘deep’ in the subband pyramid requiring more bits to encode the position information. Deeper trees also lead to the addition of more number of coefficients corresponding to the parent nodes to the LIC set that require allocation of extra bits in the next SP. This is illustrated in Figures 4.4 and 4.6. The plots show the mean-squared-error (MSE) introduced by SPIHT, as a function of bit rate (bits per pixel, bpp), for periodic and symmetric extension, for all the  $LA_{\perp}$  and  $bi_{\perp}$  wavelets being compared. The bit rate shown corresponds to CRs from 8:1 (1 bpp) to 64:1 (0.125 bpp). For LF and MF images, the same MSE is achieved at a lower bit rate for symmetric extension than periodic extension. In other words, symmetric extension requires fewer bits to attain the same MSE as periodic extension. So for a given CR, symmetric extension encodes more DWT coefficients which in turn generates superior PSNR results. Moreover, this MSE difference is largest for LF images; the difference decreases for MF images and is negligible for HF images.

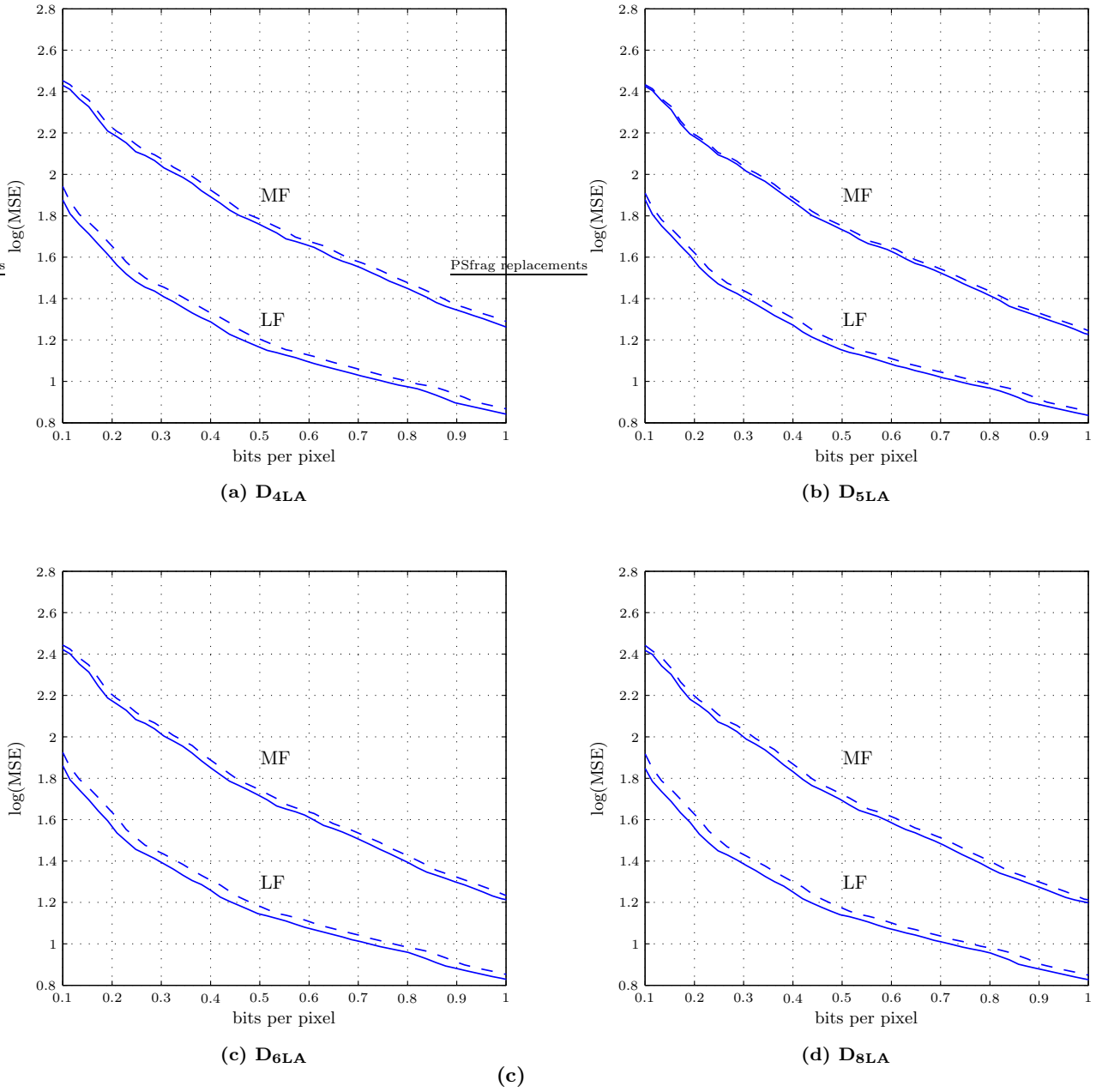


Figure 4.4: Mean-squared-error (MSE) introduced by SPIHT as a function of bit rate (bits per pixel, bpp) for LF and MF images. Symmetric and periodic extensions are represented by solid and dashes lines respectively.

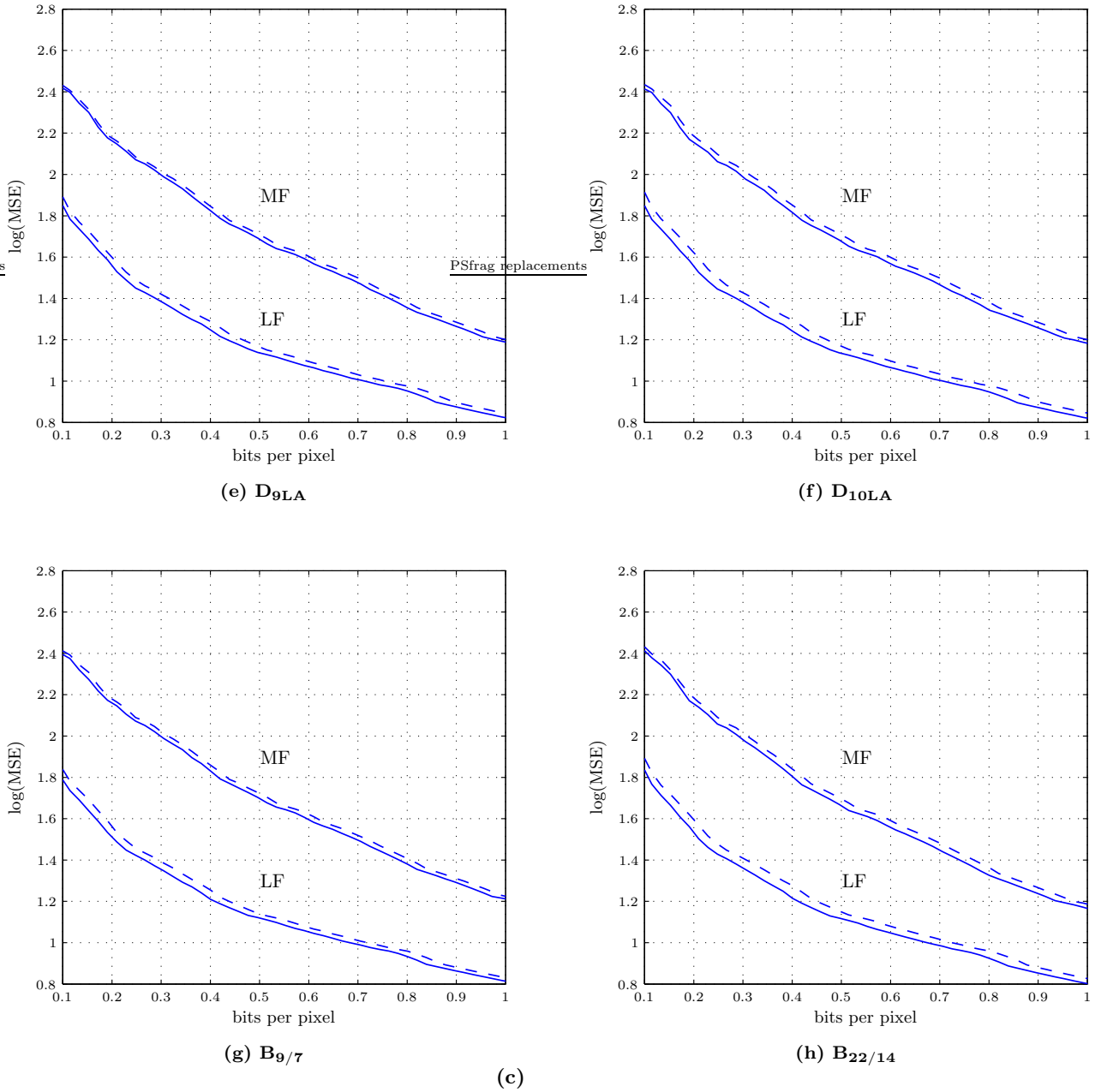


Figure 4.5: Mean-squared-error (MSE) introduced by SPIHT as a function of bit rate (bits per pixel, bpp) for LF and MF images. Symmetric and periodic extensions are represented by solid and dashes lines respectively.

Fourth, the superior performance of symmetric extension over periodic extension occurs throughout an image and not just at the borders (for both  $\text{bi}\perp$  and  $\perp$  wavelets). The PSNR of the compressed images were computed after cropping the borders (the number of cropped rows and columns was half the filter length). It was observed that the PSNRs of the cropped images were very similar to the PSNRs of the uncropped images. Thus, the discontinuities introduced by periodic extension at the borders decrease the PSNR throughout a compressed image. This is expected since the discontinuities generate spurious high frequencies that modify the hierarchical subband structure which, in turn, decreases the efficiency of the SPIHT coder.

#### 4.4.3 Orthogonal vs. biorthogonal

The FFT and TDC methods exclude the use of symmetric extension with orthogonal wavelets for computing the non-expansive DWT. The TDM method allows to implement symmetric extension technique for both orthogonal and biorthogonal wavelets. Hence, we can now compare the compression performance of orthogonal wavelets with biorthogonal wavelets when both use symmetric extension. We perform the comparison by choosing two sets of  $\text{LA}\perp$  and  $\text{bi}\perp$  wavelets ( $\text{D}_{5\text{LA}}$  and  $\text{B}_{9/7}$ ,  $\text{D}_{9\text{LA}}$  and  $\text{B}_{22/14}$ ) that have similar filter properties (VO, filter length and smoothness). Although the wavelets being compared do not have similar GDD or ON values, it is to be noted that  $\text{LA}\perp$  wavelets have near linear phase (low GDD) and biorthogonal wavelets have nearly orthonormal (low ON) properties. The impact of these two filter properties are described in Chapter 3 of this thesis. The results are presented in Table 4.8 and are obtained from PSNR data for symmetric extension in Tables B.1 - B.3. The entries shown in Table 4.8 are obtained by averaging PSNR difference between  $\text{bi}\perp$  wavelet and the corresponding  $\text{LA}\perp$  wavelet for an image type at a given CR. The results indicate that there are almost no significant differences in performance between the  $\text{bi}\perp$  and  $\perp$  wavelets. Only four comparisons result in significant differences ( $\geq 0.1\text{dB}$ )—and three of these cases are for LF images.

Properties	Wavelets			
	$B_{9/7}$	$D_{5LA}$	$B_{22/14}$	$D_{9LA}$
O.N	0.015	0	0.011	0
Length(A,S)	9,7	10,10	22,14	18,18
V.O (A)	4	5	5	9
Regular. (S)	2.12	2.10	3.14	3.16
GDD	0	0.11	0	0.11

Table 4.7: Properties of the biorthogonal and orthogonal wavelets: orthonormality, filter length (analysis, synthesis), vanishing order (analysis), regularity (synthesis), and group delay difference parameter.

Table 4.8: Average PSNR improvement (in dB) of the  $bi_{\perp}$  wavelets over the  $LA_{\perp}$  wavelets; symmetric extension is used in all cases.

Image Type	Wavelet	Compression Ratio			
		8:1	16:1	32:1	64:1
Low Frequency	$B_{9/7}-D_{5LA}$	0.080	0.135	0.210	0.170
	$B_{22/14}-D_{9LA}$	0.095	0.087	0.085	0.072
Medium Frequency	$B_{9/7}-D_{5LA}$	0.062	0.095	-0.015	0.070
	$B_{22/14}-D_{9LA}$	0.112	0.075	0.002	0.040
High Frequency	$B_{9/7}-D_{5LA}$	0.035	0.007	0.027	-0.030
	$B_{22/14}-D_{9LA}$	0.037	0.020	0.042	-0.005

The slight performance advantage of the  $bi_{\perp}$  wavelets for LF images can be associated with the extended passband for lowpass filters as shown in Figures 3.6 and 3.7 in chapter 3. The extended response of  $bi_{\perp}$  wavelets aids in higher energy compaction in the lower frequency subbands as compared to  $\perp$  wavelets. Table 4.6 shows the energy compaction for symmetric extension. It is observed that  $bi_{\perp}$  wavelets have higher energy compaction than the corresponding  $LA_{\perp}$  wavelets although they possess lower VO. Consequently, as explained in the Section 4.4.3, the  $bi_{\perp}$  wavelets will require fewer bits than the  $\perp$  wavelets to capture the same amount of information. Figure 4.6 compares the MSE introduced by SPIHT for  $bi_{\perp}$  wavelets ( $B_{9/7}$  and  $B_{22/14}$ ) and the corresponding  $LA_{\perp}$  wavelet ( $D_{5LA}$  and  $D_{9LA}$ ) when both employ symmetric extension. *Lena* image is used for the LF plot; *Barbara*

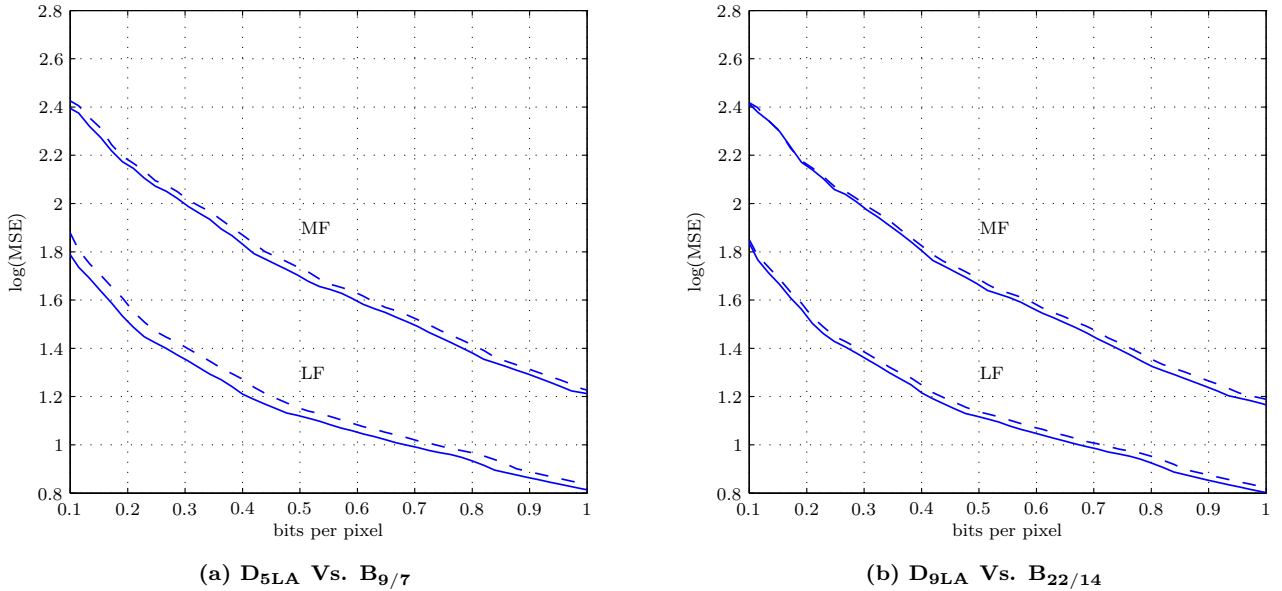


Figure 4.6: Mean-squared-error (MSE) introduced by SPIHT as a function of bit rate (bits per pixel, bpp) for LF and MF images. Symmetric extensions are represented by solid lines. Periodic extensions are in dashed lines.

image is used for the MF plot. It is observed that  $bi_{\perp}$  wavelets require fewer bits than  $LA_{\perp}$  wavelets for the same MSE; not surprisingly, this difference is larger for LF images and decreases for MF and HF images. The differences decrease for the longer length filters. This is because  $D_{9LA}$  has a substantially larger vanishing order than  $B_{22/14}$ ; this advantage of the  $\perp$  wavelet may be significant enough to compensate for the advantage of the  $bi_{\perp}$  wavelet's lowpass magnitude response.

Also, as shown in section 3.4, the  $bi_{\perp}$  wavelets have  $GDD = 0$ ; this does not affect the hierarchical subband structure as in  $LA_{\perp}$  wavelets ( $D_{5LA} = 0.11$ ,  $D_{9LA} = 0.48$ ).

## 4.5 Subjective results and analysis

At lower compression ratios (8:1, 16:1) there is a strong correlation between PSNR and image quality of the reconstructed image. However, at higher compression ratios (32:1, 64:1), visible artifacts like ringing, tiling, boundary noise and blurring are introduced in the reconstructed images. These artifacts depend on the choice of wavelets and the bit allocation algorithm (in our case SPIHT). A subjective analysis of reconstructed image quality allows us to better understand the effect of the various filter properties.

We present the results for periodic as well as symmetric extension for each image type. We use both biorthogonal and orthogonal wavelets for each extension type. Section 4.5.1 compares the subjective quality of the reconstructed images for periodic extension. Subsection 4.5.2 presents the results for symmetric extension.

### 4.5.1 Periodic extension

We have chosen one image from each of the three image types: LF (*Lena*), MF (*Barbara*) and HF (*Mandrill*). Each image is compressed at 32:1 using three shorter ( $D_{4LA}$ ,  $D_{4A}$  and  $B_{9/7}$ ) and three longer ( $D_{10LA}$ ,  $D_{10A}$  and  $B_{22/14}$ ) wavelets. Figures C.1 and Figures C.2-C.7 show the uncompressed and compressed *Lena* image respectively. Similarly, Figures C.9-C.14 and Figures C.16 - C.21 show the image *Lighthouse* and *Mandrill* respectively. The PSNR of the compressed image as well as the wavelet used are displayed.

For LF images, all reconstructed images show border distortion associated with periodic extension. The boundary distortions are more prominent for longer wavelets due to their longer filters. It can also be observed that smooth regions in the image (the face and the background for *Lena*) are better represented by the shorter wavelets than the longer wavelets. However, details like line edges and the hat are better preserved by longer length wavelets. Higher ringing at the edges for longer wavelets can be attributed to their longer synthesis filters. Higher vanishing order of the longer wavelets allows them to preserve the

high frequency details. The reconstructed images of  $A\perp$  wavelets in Figures C.2 and C.4 also show a lot of blocking artifacts at high frequency edges. The blocking is more pronounced in the case of  $D_{10A}$ . However, the blocking artifact is negligible in the reconstructed images for  $LA\perp$  wavelets (Figures C.3 and C.5) and absent in  $bi\perp$  wavelets (Figures C.6 and C.7). This suggests that the blocking artifact in the reconstructed image is due to the non-linear phase of  $A\perp$  wavelets that affects SPIHT encoding and decoding.

For MF and HF images, more blocking is observed near the high frequency edges for  $A\perp$  wavelets; this is especially true in the case of  $D_{10A}$  wavelets. The  $bi\perp$  wavelets suffer less from blocking and the overall image quality is better than  $LA\perp$  wavelets although the PSNRs are nearly the same.

### 4.5.2 Symmetric extension

In this section, we compare the perceived quality of reconstructed images of  $bi\perp$  wavelets with the corresponding  $LA\perp$  wavelets ( $D_{5LA}$  and  $B_{9/7}$ ,  $D_{9LA}$  and  $B_{22/14}$ ). We choose one image from each of the three image types: LF (*Lena*), MF (*Barbara*) and HF (*SanDiego*). The captions below the images give the PSNR of the compressed image as well as the wavelet used. Figures D.1-D.4 show the reconstructed images for *Lena* image at 64:1. Similarly, Figures D.5-D.8 and Figures D.9-D.12 show images of *Barbara* and *SanDiego* reconstructed at a compression ratio of 64:1 and 32:1 respectively.

We observe higher amount of ringing in the reconstructed images of  $LA\perp$  wavelets. However, no border distortion as present in the reconstructed images for periodic extension is observed. Figure D.1 and D.2 show the LF image (*Lena*) compressed at CR of 64:1 by  $D_{5LA}$  and  $B_{9/7}$  respectively. Although the images differ in PSNR by 0.07dB, the  $D_{5LA}$  image shows more ringing, especially on the face and at the edges. Some amount of tiling artifact is also present near the eyes. However,  $D_{5LA}$  captures high frequency content better as evident on the hat portion of the image. Similar trend is observed for the  $D_{9LA}$  (Figure D.3) and  $B_{22/14}$  (Figure D.4) images. Figures D.8 and D.7 compare the reconstructed images of  $B_{22/14}$  and

$D_{9LA}$  for a MF image (Barbara) at CR of 64:1. The substantial amount of ringing present in  $D_{9LA}$  overshadows the high frequency component present in the pants, scarf and table cloth. The face also appears more clear in  $B_{22/14}$  image. The same phenomenon is observed in reconstructed images for  $D_{5LA}$  and  $B_{9/7}$ . It is to be noted that the PSNR difference between the  $LA\perp$  wavelets and the corresponding  $bi\perp$  wavelets is negligible for *Barbara* image. Figures D.12 and D.11 compare  $B_{22/14}$  and  $D_{9LA}$  for a HF image (San Diego) at CR of 32:1. The orthogonal wavelets preserve high frequency better than the corresponding biorthogonal wavelets.

The higher amount of ringing and tiling in orthogonal wavelets can be attributed to their slightly non-linear phase that alters the hierarchical subband structure. Orthogonal wavelets also have longer synthesis filters:  $B_{9/7}(7)$  vs.  $D_{5LA}(10)$  and  $B_{22/14}(14)$  vs.  $D_{9LA}(18)$ . Orthogonal wavelets preserve high frequency better because they have higher vanishing orders (see Table 4.7).

# Chapter 5

## Conclusions and future work

### 5.1 Conclusions

We present several conclusions based on our evaluations of the wavelet filter properties developed in chapter 3, analysis of the DWT computation methods described in Chapter 2 and our results presented in chapter 4. Our conclusions are described below.

1. Signal extension is used to overcome the finite signal length problem in image compression. Widely used FFT and TDC based techniques do not allow the implementation of the symmetric extension technique with orthogonal wavelets. However, contrary to popular belief, recently developed matrix methods have made it feasible for orthogonal wavelets to employ the superior symmetric extension technique at an image's borders. This is reflected in our results; the PSNR improvement for symmetric extension is around 0.25dB for LF images and 0.1 for MF images for both  $bi\perp$  and  $\perp$  wavelets. The primary reason for this is the symmetric extension's ability to concentrate more energy in the lower frequency subbands.
2. Previously published results have shown that biorthogonal wavelets outperform orthogonal wavelets. The comparison was made for orthogonal wavelets with periodic

extension against biorthogonal wavelets with symmetric extension. Now, by employing the TDM method,  $\perp$  wavelets can be compared to  $\text{bi}\perp$  wavelets on an equal footing with regard to the type of extension. Our results indicate that  $\text{bi}\perp$  and  $\perp$  wavelets generate similar PSNR performance when they have similar filter properties and both employ symmetric extension. Although the  $\text{bi}\perp$  wavelets indicate a small performance gain over the  $\perp$  wavelets for low frequency images (about 0.1dB), this advantage is significantly smaller than previously published results and has been explained here in terms of the magnitude response passband edge frequency.

3. This thesis has demonstrated that linear (or near-linear) phase filters are critical to compression performance—particularly for low and medium frequency images where PSNR improvements up to  $\sim 0.5\text{dB}$  are realized for the near-linear phase filters. This is because non-linear phase filters adversely affect the hierarchical wavelet decomposition structure decreasing the efficiency of SPIHT encoding and decoding.
4. Subjectively, the  $\text{LA}\perp$  wavelets perform better than the  $\text{A}\perp$  wavelets (which suffer from severe blocking artifacts). Although the PSNR of  $\text{LA}\perp$  wavelets are similar to  $\text{bi}\perp$  wavelets,  $\text{La}\perp$  wavelets suffer from more ringing as a result of their non-linear phase.

## 5.2 Future work

This thesis has identified and explained new parameters and techniques that are critical to high quality image compression performance. Although this thesis illustrates improved image compression performance for orthogonal wavelets by using symmetric extension, opportunities for further improvement remain.

1. Ideally, a constant group delay is desired since it does not alter the hierarchical subband structure. SPIHT encoding and decoding is optimized to take advantage of the in-

formation in the wavelet hierarchical structure. However, recent encoders and decoders like EBCOT (Embedded Block Coding with Optimal Truncation) in JPEG2000 are not necessarily dependent on the wavelet structure for coding into bitstreams. Hence, the subjective and objective performance of LA $\perp$  wavelets may be improved (relative to the bi $\perp$  wavelets) under quantization with EBCOT. A $\perp$  wavelet performance may also be improved.

2. Symmetric extension using the TDM method has been demonstrated for only a few LA $\perp$  and bi $\perp$  wavelets due to the requirement of a low condition number for the regenerating matrix. It appears that the regenerating matrix is better conditioned for wavelets that have linear phase. Hence, techniques to improve the condition number of the matrix along with the design of near linear phase wavelets would be beneficial in the use of the TDM method to compute the DWT.

# Bibliography

- [1] Jonathan N. Bradley and Vance Faber. Perfect reconstruction with critically sampled filter banks and linear boundary conditions. *IEEE Trans. on Signal Proc.*, 43(4):994–997, April 1995.
- [2] Christopher M. Brislawn. Preservation of subband symmetry in multirate signal coding. *IEEE Trans. on Signal Proc.*, 43(12):3046–2050, December 1995.
- [3] I. Daubechies. *Ten Lectures on Wavelets*. SIAM, Philadelphia PA, first edition, 1992.
- [4] Ricardo L. de Queiroz. Subband processing of finite length signals without border distortions. *Proceedings of the International Conference on Acoustics, Speech and Signal Processing*, 4:613–617, 1992.
- [5] John D. Villasenor, Benjamin Belzer, and Judy Liao. Wavelet filter evaluation for image compression. *IEEE Trans. on Image Processing*, 4(8):1053–1060, August 1995.
- [6] Timo Eirola. Sobolev characterization of solutions of dilation equations. *SIAM J. Math. Anal.*, 23:1015–1030, 1992.
- [7] Mislav Grgic, Mario Ravnjak, and Branka Zovko-Cihlar. Filter comparison in wavelet transform of still images. *Industrial Electronics, 1999. ISIE '99. Proceedings of the IEEE International Symposium*, 1:105–110, 1999.

- [8] Sonja Grgic, Mislav Grgic, and Branka Zovko-Cihlar. Performance analysis of image compression using wavelets. *IEEE Trans. on Industrial Electronics*, 48(3):682–695, June 1994.
- [9] Kiyoshi Nishikawa Hitoshi Kiya and Masahiro Iwahashi. A development of symmetric extension method for subband image coding. *IEEE Trans. on Image Proc.*, 3(1):78–81, January 1994.
- [10] L. R. Iyer and A. E. Bell. Improving image compression performance with balanced multiwavelets. *Proc. of 35th Asilomar Conference on Signals, Systems and Computers*, November 2001, (Invited Paper).
- [11] Jérôme Lebrun and Martin Vetterli. Balanced multiwavelets theory and design. *IEEE Transactions on Signal Processing*, 46(4):1119–1125, April 1998.
- [12] Michael Lightstone and Eric Majani. Low bit-rate design considerations for wavelet-based image coding. *Proc. of SPIE Symp. on Visual Comm. and Image Proc.*, 2308:501–512, 1994.
- [13] Michael Lightstone, Eric Majani, and Sanjit K. Mitra. Low bit-rate design considerations for wavelet-based image coding. *Multidimensional systems and signal processing*, 8(1-2):111–128, January 1997.
- [14] S. Mallat. *A Wavelet Tour of Signal Processing*. Academic Press, San Diego CA, 1998.
- [15] J. E. Odegard and C. S. Burrus. Discrete finite variation: a new measure of smoothness for the design of wavelet basis. *Proceedings of the International Conference on Acoustics, Speech and Signal Processing*, 3:1467–70, 1996.
- [16] Olivier Rioul. Regular wavelets: a discrete-time approach. *IEEE Trans. on Signal Processing*, 41(12):3572 – 3579, Dec. 1993.

- [17] Steven L. Eddins Roberto H. Bamberger and Veyis Nuri. Genralized symmetric extension for size-limited multirate filter banks. *IEEE Trans. on Image Proc.*, 3(1):82–87, January 1994.
- [18] S. Rout and A. E. Bell. Color image compression: multiwavelets vs. scalar wavelets. *Proceedings of International Conference on Acoustics, Speech, and Signal Processing*, 4:3501 – 3504, 2002.
- [19] A. Said and W. A. Pearlman. A new, fast, and efficient image codec based on set partitioning in hierarchical trees. *IEEE Trans. on Circ. and Syst. for Video Tech.*, 6(3):243–250, June 1996.
- [20] J. M. Shapiro. Embedded image coding using zerotrees of wavelet coefficients. *IEEE Trans. on Image Proc.*, 41(12):3445–3462, December 1993.
- [21] Yun Q. Shi and Huifang Sun. *Image and Video Compression for Multimedia Engineering: Fundamentals, Algorithms, and Standards*. CRC Press LLC, Boca Raton FL, first edition, 2000.
- [22] Vitor Silva and Luis de Sa. General method for perfect reconstruction : Subband processing of finite length signals using linear extensions. *IEEE Trans. on Signal Proc.*, 47(9):2572–2575, September 1999.
- [23] Mark J. T. Smith and Steven L. Eddins. Analysis/synthesis techniques for subband image coding. *IEEE Trans. on Acoustics, Speech, and Signal Proc.*, 38(8):1446–1456, August 1990.
- [24] Gilbert Strang and Truong Nguyen. *Wavelets and Filter Banks*. Wellesley-Cambridge Press, Wellesley MA, first edition, 1996.
- [25] Michael Unser. Approximation power of biorthogonal wavelet expansions. *IEEE Trans. on Signal Processing*, 44(3):519–527, 1996.

- [26] Michael Unser and Thierry Blu. Mathematical properties of the jpeg2000 wavelet filters. *IEEE Trans. on Image Processing*, to appear in 2003.
- [27] D. Wei, H. Pai, and A. C. Bovik. Antisymmetric biorthogonal coiflets for image coding. *Proceedings of the IEEE International Conference on Image Processing (ICIP)*, October 1998.
- [28] Ian H. Witten, Radford M. Neal, and John G. Cleary. Arithmetic coding for data compression. *Communications of the ACM*, 30(6):520–540, June 1987.

# Appendix A

## Periodic extension results

Table A.1: PSNR values relative to the corresponding PSNR value of  $D_{4LA}$  for LF images: *Lena* and *Peppers*. A positive entry corresponds to PSNR value higher than that of  $D_{4LA}$ . A negative entry corresponds to PSNR value lower than that of  $D_{4LA}$ .

Image	Wavelet	TDM Method			
		CR			
		08:1	16:1	32:1	64:1
<i>Lena</i>	$D_{4LA}$	<b>39.42</b>	<b>36.08</b>	<b>32.81</b>	<b>29.80</b>
	$D_{4A}$	+0.00	+0.00	-0.04	-0.06
	$D_{5LA}$	<b>+0.12</b>	<b>+0.22</b>	<b>+0.27</b>	<b>+0.32</b>
	$D_{5A}$	+0.04	+0.07	+0.00	-0.02
	$D_{6LA}$	<b>+0.16</b>	<b>+0.23</b>	<b>+0.22</b>	<b>+0.14</b>
	$D_{6A}$	+0.05	+0.05	+0.03	+0.02
	$D_{7LA}$	<b>+0.18</b>	<b>+0.29</b>	<b>+0.35</b>	<b>+0.33</b>
	$D_{7A}$	+0.07	+0.11	+0.07	+0.01
	$D_{8LA}$	<b>+0.18</b>	<b>+0.32</b>	<b>+0.31</b>	<b>+0.23</b>
	$D_{8A}$	+0.00	-0.02	-0.12	-0.17
	$D_{9LA}$	<b>+0.25</b>	<b>+0.39</b>	<b>+0.47</b>	<b>+0.47</b>
	$D_{9A}$	+0.01	-0.03	-0.06	-0.03
	$D_{10LA}$	<b>+0.22</b>	<b>+0.35</b>	<b>+0.35</b>	<b>+0.28</b>
	$D_{10A}$	+0.04	+0.05	-0.09	-0.11
$B_{9/7}$	+0.24	+0.46	+0.46	+0.33	
$B_{22/14}$	<b>+0.29</b>	<b>+0.50</b>	<b>+0.56</b>	<b>+0.57</b>	
<i>Peppers</i>	$D_{4LA}$	<b>37.46</b>	<b>35.21</b>	<b>32.54</b>	<b>29.55</b>
	$D_{4A}$	-0.07	-0.10	-0.21	-0.20
	$D_{5LA}$	<b>+0.06</b>	<b>+0.08</b>	<b>+0.11</b>	<b>+0.18</b>
	$D_{5A}$	-0.07	-0.10	-0.18	-0.20
	$D_{6LA}$	<b>+0.04</b>	<b>+0.06</b>	<b>+0.10</b>	<b>+0.10</b>
	$D_{6A}$	-0.12	-0.17	-0.27	-0.28
	$D_{7LA}$	<b>+0.02</b>	<b>+0.04</b>	<b>+0.11</b>	<b>+0.15</b>
	$D_{7A}$	-0.15	-0.23	-0.35	-0.37
	$D_{8LA}$	<b>+0.00</b>	<b>+0.02</b>	<b>+0.00</b>	<b>+0.01</b>
	$D_{8A}$	-0.17	-0.29	-0.41	-0.39
	$D_{9LA}$	<b>+0.03</b>	<b>+0.02</b>	<b>+0.05</b>	<b>+0.10</b>
	$D_{9A}$	-0.24	-0.39	-0.60	-0.61
	$D_{10LA}$	<b>+0.03</b>	<b>+0.06</b>	<b>+0.08</b>	<b>+0.11</b>
	$D_{10A}$	-0.27	-0.41	-0.59	-0.62
$B_{9/7}$	+0.06	+0.19	+0.25	+0.25	
$B_{22/14}$	<b>+0.20</b>	<b>+0.24</b>	<b>+0.30</b>	<b>+0.42</b>	

Table A.2: PSNR values relative to the corresponding PSNR value of  $D_{4LA}$  for LF images: *Boat* and *Goldhill*. A positive entry corresponds to PSNR value higher than that of  $D_{4LA}$ . A negative entry corresponds to PSNR value lower than that of  $D_{4LA}$ .

Image	Wavelet	TDM Method			
		CR			
		08:1	16:1	32:1	64:1
<i>Boat</i>	$D_{4LA}$	<b>37.69</b>	<b>33.17</b>	<b>29.70</b>	<b>27.15</b>
	$D_{4A}$	-0.03	-0.06	-0.10	-0.09
	$D_{5LA}$	<b>+0.18</b>	<b>+0.14</b>	<b>+0.12</b>	<b>+0.07</b>
	$D_{5A}$	-0.05	-0.04	+0.01	-0.08
	$D_{6LA}$	<b>+0.18</b>	<b>+0.16</b>	<b>+0.13</b>	<b>+0.08</b>
	$D_{6A}$	-0.04	-0.06	-0.17	-0.25
	$D_{7LA}$	<b>+0.20</b>	<b>+0.22</b>	<b>+0.13</b>	<b>+0.07</b>
	$D_{7A}$	-0.08	-0.05	-0.11	-0.18
	$D_{8LA}$	<b>+0.18</b>	<b>+0.17</b>	<b>+0.18</b>	<b>+0.08</b>
	$D_{8A}$	-0.20	-0.18	-0.23	-0.30
	$D_{9LA}$	<b>+0.33</b>	<b>+0.30</b>	<b>+0.24</b>	<b>+0.19</b>
	$D_{9A}$	-0.17	-0.17	-0.28	-0.30
	$D_{10LA}$	<b>+0.26</b>	<b>+0.24</b>	<b>+0.14</b>	<b>+0.08</b>
	$D_{10A}$	-0.26	-0.20	-0.29	-0.32
$B_{9/7}$	+0.39	+0.34	+0.38	+0.32	
$B_{22/14}$	<b>+0.62</b>	<b>+0.49</b>	<b>+0.40</b>	<b>+0.33</b>	
<i>Goldhill</i>	$D_{4LA}$	<b>35.46</b>	<b>32.00</b>	<b>29.48</b>	27.59
	$D_{4A}$	-0.08	-0.03	-0.02	<b>+0.01</b>
	$D_{5LA}$	<b>+0.04</b>	<b>+0.07</b>	<b>+0.18</b>	<b>+0.25</b>
	$D_{5A}$	-0.07	-0.02	-0.02	-0.02
	$D_{6LA}$	<b>+0.09</b>	<b>+0.10</b>	<b>+0.06</b>	<b>+0.05</b>
	$D_{6A}$	-0.07	-0.08	-0.09	-0.07
	$D_{7LA}$	<b>+0.05</b>	<b>+0.07</b>	<b>+0.10</b>	<b>+0.14</b>
	$D_{7A}$	-0.08	-0.04	-0.05	-0.05
	$D_{8LA}$	<b>+0.09</b>	<b>+0.14</b>	<b>+0.10</b>	<b>+0.07</b>
	$D_{8A}$	-0.12	-0.12	-0.16	-0.12
	$D_{9LA}$	<b>+0.09</b>	<b>+0.12</b>	<b>+0.20</b>	<b>+0.21</b>
	$D_{9A}$	-0.14	-0.12	-0.15	-0.16
	$D_{10LA}$	<b>+0.11</b>	<b>+0.14</b>	<b>+0.09</b>	<b>+0.07</b>
	$D_{10A}$	-0.12	-0.08	-0.07	-0.06
$B_{9/7}$	+0.12	<b>+0.21</b>	<b>+0.27</b>	+0.21	
$B_{22/14}$	<b>+0.14</b>	+0.16	+0.22	<b>+0.24</b>	

Table A.3: PSNR values relative to the corresponding PSNR value of  $D_{4LA}$  for MF images: *Barbara* and *Lighthouse*. A positive entry corresponds to PSNR value higher than that of  $D_{4LA}$ . A negative entry corresponds to PSNR value lower than that of  $D_{4LA}$ .

Image	Wavelet	TDM Method			
		CR			
		08:1	16:1	32:1	64:1
<i>Barbara</i>	$D_{4LA}$	<b>35.22</b>	<b>30.30</b>	26.72	23.96
	$D_{4A}$	<b>+0.00</b>	<b>+0.00</b>	<b>+0.05</b>	<b>+0.02</b>
	$D_{5LA}$	<b>+0.44</b>	<b>+0.32</b>	<b>+0.37</b>	<b>+0.21</b>
	$D_{5A}$	+0.28	+0.15	+0.08	+0.06
	$D_{6LA}$	<b>+0.56</b>	<b>+0.39</b>	<b>+0.28</b>	<b>+0.09</b>
	$D_{6A}$	+0.39	+0.24	+0.22	+0.06
	$D_{7LA}$	<b>+0.72</b>	<b>+0.55</b>	<b>+0.40</b>	<b>+0.13</b>
	$D_{7A}$	+0.53	+0.37	+0.28	+0.11
	$D_{8LA}$	<b>+0.77</b>	<b>+0.61</b>	<b>+0.36</b>	<b>+0.14</b>
	$D_{8A}$	+0.47	+0.33	+0.19	+0.05
	$D_{9LA}$	<b>+0.87</b>	<b>+0.74</b>	<b>+0.59</b>	<b>+0.26</b>
	$D_{9A}$	+0.58	+0.35	+0.27	+0.09
	$D_{10LA}$	<b>+0.88</b>	<b>+0.76</b>	<b>+0.49</b>	<b>+0.17</b>
	$D_{10A}$	+0.63	+0.45	+0.34	+0.16
$B_{9/7}$	+0.43	+0.29	+0.15	+0.14	
$B_{22/14}$	<b>+0.80</b>	<b>+0.64</b>	<b>+0.36</b>	<b>+0.30</b>	
<i>Lighthouse</i>	$D_{4LA}$	<b>33.03</b>	<b>29.47</b>	<b>26.62</b>	24.05
	$D_{4A}$	-0.07	-0.08	<b>+0.00</b>	<b>+0.04</b>
	$D_{5LA}$	<b>+0.16</b>	<b>+0.09</b>	<b>+0.15</b>	<b>+0.24</b>
	$D_{5A}$	-0.15	-0.14	-0.11	+0.00
	$D_{6LA}$	<b>+0.11</b>	<b>+0.05</b>	<b>+0.00</b>	<b>+0.10</b>
	$D_{6A}$	-0.20	-0.18	-0.13	-0.01
	$D_{7LA}$	<b>+0.11</b>	<b>+0.03</b>	<b>+0.05</b>	<b>+0.19</b>
	$D_{7A}$	-0.18	-0.19	-0.17	+0.10
	$D_{8LA}$	<b>+0.13</b>	<b>+0.02</b>	<b>+0.00</b>	<b>+0.19</b>
	$D_{8A}$	-0.31	-0.28	-0.26	-0.02
	$D_{9LA}$	<b>+0.15</b>	<b>+0.11</b>	<b>+0.10</b>	<b>+0.32</b>
	$D_{9A}$	-0.34	-0.28	-0.25	+0.01
	$D_{10LA}$	<b>+0.12</b>	<b>+0.05</b>	<b>+0.00</b>	<b>+0.18</b>
	$D_{10A}$	-0.31	-0.28	-0.28	+0.10
$B_{9/7}$	+0.25	+0.13	+0.02	+0.20	
$B_{22/14}$	<b>+0.32</b>	<b>+0.14</b>	<b>+0.06</b>	<b>+0.36</b>	

Table A.4: PSNR values relative to the corresponding PSNR value of  $D_{4LA}$  for MF images: *House* and *Nitf7*. A positive entry corresponds to PSNR value higher than that of  $D_{4LA}$ . A negative entry corresponds to PSNR value lower than that of  $D_{4LA}$ .

Image	Wavelet	TDM Method			
		CR			
		08:1	16:1	32:1	64:1
<i>House</i>	$D_{4LA}$	<b>29.91</b>	<b>25.27</b>	<b>22.45</b>	<b>20.59</b>
	$D_{4A}$	-0.17	-0.09	-0.10	-0.08
	$D_{5LA}$	<b>-0.02</b>	<b>+0.06</b>	<b>+0.05</b>	<b>+0.06</b>
	$D_{5A}$	-0.34	-0.22	-0.15	-0.19
	$D_{6LA}$	<b>-0.02</b>	<b>+0.02</b>	<b>+0.06</b>	<b>+0.06</b>
	$D_{6A}$	-0.40	-0.20	-0.16	-0.16
	$D_{7LA}$	<b>-0.10</b>	<b>-0.01</b>	<b>+0.08</b>	<b>+0.10</b>
	$D_{7A}$	-0.45	-0.25	-0.18	-0.16
	$D_{8LA}$	<b>-0.08</b>	<b>+0.01</b>	<b>+0.10</b>	<b>+0.05</b>
	$D_{8A}$	-0.60	-0.36	-0.20	-0.25
	$D_{9LA}$	<b>-0.07</b>	<b>+0.07</b>	<b>+0.16</b>	<b>+0.09</b>
	$D_{9A}$	-0.60	-0.31	-0.21	-0.23
	$D_{10LA}$	<b>-0.07</b>	<b>+0.03</b>	<b>+0.11</b>	<b>+0.08</b>
	$D_{10A}$	-0.69	-0.37	-0.26	-0.28
$B_{9/7}$	+0.01	+0.11	+0.10	+0.10	
$B_{22/14}$	<b>+0.05</b>	<b>+0.12</b>	<b>+0.20</b>	<b>+0.15</b>	
<i>Nitf7</i>	$D_{4LA}$	<b>25.00</b>	<b>21.92</b>	<b>19.59</b>	<b>17.60</b>
	$D_{4A}$	-0.43	-0.38	-0.24	-0.09
	$D_{5LA}$	-0.22	-0.18	<b>-0.04</b>	<b>+0.05</b>
	$D_{5A}$	<b>-0.11</b>	<b>-0.15</b>	-0.12	-0.03
	$D_{6LA}$	<b>+0.04</b>	<b>+0.03</b>	<b>+0.07</b>	<b>+0.05</b>
	$D_{6A}$	-0.24	-0.26	-0.19	-0.11
	$D_{7LA}$	<b>+0.04</b>	<b>+0.04</b>	<b>+0.07</b>	<b>+0.13</b>
	$D_{7A}$	-0.42	-0.42	-0.25	-0.11
	$D_{8LA}$	<b>+0.04</b>	<b>+0.05</b>	<b>+0.09</b>	<b>+0.08</b>
	$D_{8A}$	-0.21	-0.24	-0.19	-0.09
	$D_{9LA}$	<b>-0.16</b>	<b>-0.11</b>	<b>+0.04</b>	<b>+0.15</b>
	$D_{9A}$	-0.42	-0.44	-0.28	-0.15
	$D_{10LA}$	<b>+0.01</b>	<b>+0.02</b>	<b>+0.08</b>	<b>+0.09</b>
	$D_{10A}$	-0.45	-0.46	-0.33	-0.15
$B_{9/7}$	<b>+0.02</b>	+0.05	<b>+0.07</b>	+0.09	
$B_{22/14}$	-0.02	<b>+0.08</b>	<b>+0.07</b>	<b>+0.13</b>	

Table A.5: PSNR values relative to the corresponding PSNR value of  $D_{4LA}$  for HF images: *Satellite* and *Mandrill*. A positive entry corresponds to PSNR value higher than that of  $D_{4LA}$ . A negative entry corresponds to PSNR value lower than that of  $D_{4LA}$ .

Image	Wavelet	TDM Method			
		CR			
		08:1	16:1	32:1	64:1
<i>Satellite</i>	$D_{4LA}$	<b>27.41</b>	<b>24.75</b>	<b>23.26</b>	21.94
	$D_{4A}$	-0.05	-0.02	<b>+0.00</b>	<b>+0.02</b>
	$D_{5LA}$	<b>+0.06</b>	<b>+0.07</b>	<b>+0.08</b>	<b>+0.09</b>
	$D_{5A}$	-0.02	-0.01	+0.00	+0.02
	$D_{6LA}$	<b>+0.06</b>	<b>+0.07</b>	<b>+0.05</b>	<b>+0.05</b>
	$D_{6A}$	-0.02	-0.01	-0.01	+0.02
	$D_{7LA}$	<b>+0.06</b>	<b>+0.06</b>	<b>+0.06</b>	<b>+0.08</b>
	$D_{7A}$	-0.01	+0.03	+0.02	+0.04
	$D_{8LA}$	<b>+0.07</b>	<b>+0.10</b>	<b>+0.09</b>	<b>+0.07</b>
	$D_{8A}$	-0.04	+0.01	+0.00	+0.03
	$D_{9LA}$	<b>+0.10</b>	<b>+0.13</b>	<b>+0.12</b>	<b>+0.12</b>
	$D_{9A}$	-0.05	+0.01	+0.00	+0.03
	$D_{10LA}$	<b>+0.10</b>	<b>+0.11</b>	<b>+0.08</b>	<b>+0.08</b>
	$D_{10A}$	-0.04	+0.02	+0.02	+0.06
$B_{9/7}$	+0.04	+0.07	+0.08	+0.05	
$B_{22/14}$	<b>+0.09</b>	<b>+0.14</b>	<b>+0.13</b>	<b>+0.14</b>	
<i>Mandrill</i>	$D_{4LA}$	<b>28.37</b>	24.83	<b>22.70</b>	<b>21.32</b>
	$D_{4A}$	-0.01	<b>+0.01</b>	-0.01	<b>+0.00</b>
	$D_{5LA}$	<b>+0.12</b>	<b>+0.10</b>	<b>+0.04</b>	<b>+0.05</b>
	$D_{5A}$	+0.01	+0.00	-0.01	+0.01
	$D_{6LA}$	<b>+0.12</b>	<b>+0.10</b>	<b>+0.07</b>	<b>+0.04</b>
	$D_{6A}$	+0.04	+0.04	+0.01	+0.00
	$D_{7LA}$	<b>+0.15</b>	<b>+0.16</b>	<b>+0.11</b>	<b>+0.07</b>
	$D_{7A}$	+0.07	+0.04	-0.01	+0.02
	$D_{8LA}$	<b>+0.17</b>	<b>+0.13</b>	<b>+0.09</b>	<b>+0.07</b>
	$D_{8A}$	+0.07	+0.06	-0.01	-0.01
	$D_{9LA}$	<b>+0.19</b>	<b>+0.19</b>	<b>+0.10</b>	<b>+0.08</b>
	$D_{9A}$	+0.06	+0.05	+0.00	-0.01
	$D_{10LA}$	<b>+0.18</b>	<b>+0.17</b>	<b>+0.10</b>	<b>+0.06</b>
	$D_{10A}$	+0.05	+0.03	-0.03	-0.01
$B_{9/7}$	+0.11	+0.09	+0.07	+0.02	
$B_{22/14}$	<b>+0.17</b>	<b>+0.16</b>	<b>+0.16</b>	<b>+0.10</b>	

Table A.6: PSNR values relative to the corresponding PSNR value of  $D_{4LA}$  for HF images: *Grass* and *SanDiego*. A positive entry corresponds to PSNR value higher than that of  $D_{4LA}$ . A negative entry corresponds to PSNR value lower than that of  $D_{4LA}$ .

Image	Wavelet	TDM Method			
		CR			
		08:1	16:1	32:1	64:1
<i>Grass</i>	$D_{4LA}$	23.13	20.05	17.97	16.44
	$D_{4A}$	<b>+0.03</b>	<b>+0.04</b>	<b>+0.04</b>	<b>+0.01</b>
	$D_{5LA}$	<b>+0.17</b>	<b>+0.13</b>	<b>+0.10</b>	<b>+0.06</b>
	$D_{5A}$	+0.12	+0.11	+0.04	+0.01
	$D_{6LA}$	<b>+0.24</b>	+0.13	+0.07	+0.03
	$D_{6A}$	<b>+0.24</b>	<b>+0.15</b>	<b>+0.10</b>	<b>+0.05</b>
	$D_{7LA}$	<b>+0.32</b>	<b>+0.21</b>	<b>+0.12</b>	<b>+0.05</b>
	$D_{7A}$	+0.30	+0.19	<b>+0.12</b>	<b>+0.05</b>
	$D_{8LA}$	<b>+0.34</b>	<b>+0.24</b>	<b>+0.11</b>	+0.05
	$D_{8A}$	+0.33	+0.20	<b>+0.11</b>	<b>+0.07</b>
	$D_{9LA}$	<b>+0.41</b>	<b>+0.26</b>	<b>+0.17</b>	<b>+0.08</b>
	$D_{9A}$	+0.36	+0.21	+0.10	+0.04
	$D_{10LA}$	<b>+0.44</b>	<b>+0.26</b>	<b>+0.14</b>	+0.06
	$D_{10A}$	+0.39	+0.23	<b>+0.14</b>	<b>+0.08</b>
$B_{9/7}$	+0.25	+0.21	+0.12	-0.01	
$B_{22/14}$	<b>+0.46</b>	<b>+0.30</b>	<b>+0.20</b>	<b>+0.07</b>	
<i>SanDiego</i>	$D_{4LA}$	<b>+26.50</b>	+23.34	<b>+21.46</b>	<b>+20.32</b>
	$D_{4A}$	<b>+0.00</b>	<b>+0.02</b>	-0.01	<b>+0.00</b>
	$D_{5LA}$	<b>+0.12</b>	<b>+0.10</b>	<b>+0.08</b>	<b>+0.05</b>
	$D_{5A}$	+0.01	+0.04	+0.01	+0.03
	$D_{6LA}$	<b>+0.12</b>	<b>+0.11</b>	<b>+0.08</b>	<b>+0.05</b>
	$D_{6A}$	+0.04	+0.06	+0.01	+0.02
	$D_{7LA}$	<b>+0.17</b>	<b>+0.14</b>	<b>+0.10</b>	<b>+0.07</b>
	$D_{7A}$	+0.04	+0.07	+0.03	+0.04
	$D_{8LA}$	<b>+0.18</b>	<b>+0.17</b>	<b>+0.12</b>	<b>+0.10</b>
	$D_{8A}$	+0.01	+0.05	+0.02	+0.02
	$D_{9LA}$	<b>+0.22</b>	<b>+0.21</b>	<b>+0.16</b>	<b>+0.12</b>
	$D_{9A}$	+0.04	+0.08	+0.05	+0.03
	$D_{10LA}$	<b>+0.19</b>	<b>+0.17</b>	<b>+0.13</b>	<b>+0.09</b>
	$D_{10A}$	+0.01	+0.08	+0.04	+0.03
$B_{9/7}$	+0.21	+0.09	+0.09	+0.02	
$B_{22/14}$	<b>+0.30</b>	<b>+0.22</b>	<b>+0.16</b>	<b>+0.10</b>	

# Appendix B

## Symmetric extension results

Table B.1: PSNR values relative to the corresponding PSNR value of  $D_{4LA}$  for LF images. A positive entry corresponds to PSNR value higher than that of  $D_{4LA}$ . A negative entry corresponds to PSNR value lower than that of  $D_{4LA}$ .

Image	CR	Wavelets							
		$D_{4LA}$	$B_{9/7}$	$D_{5LA}$	$D_{6LA}$	$D_{8LA}$	$D_{9LA}$	$B_{22/14}$	$D_{10LA}$
<i>Lena</i>	08:1	39.64	+0.19	+0.10	+0.14	+0.17	+0.24	<b>+0.31</b>	+0.23
	16:1	36.45	+0.26	+0.18	+0.23	+0.27	+0.32	<b>+0.43</b>	+0.30
	32:1	33.31	+0.28	+0.15	+0.26	+0.31	+0.35	<b>+0.49</b>	+0.35
	64:1	30.34	+0.20	+0.13	+0.15	+0.20	+0.26	<b>+0.47</b>	+0.22
<i>Peppers</i>	08:1	37.53	+0.08	+0.07	+0.04	+0.05	+0.06	<b>+0.24</b>	+0.03
	16:1	35.33	+0.21	+0.05	+0.06	+0.09	+0.04	<b>+0.27</b>	+0.07
	32:1	32.73	+0.30	+0.09	+0.10	+0.17	+0.09	<b>+0.40</b>	+0.09
	64:1	29.8	+0.37	+0.10	+0.10	+0.19	+0.15	<b>+0.47</b>	+0.13
<i>Goldhill</i>	08:1	35.65	+0.08	+0.02	+0.08	+0.08	+0.07	<b>+0.17</b>	+0.13
	16:1	32.28	+0.18	+0.05	+0.10	+0.13	+0.12	<b>+0.22</b>	+0.15
	32:1	29.87	+0.26	+0.06	+0.08	+0.09	+0.10	<b>+0.27</b>	+0.10
	64:1	28.09	+0.07	+0.07	+0.08	+0.10	+0.08	<b>+0.18</b>	+0.09
<i>Boat</i>	08:1	37.91	+0.30	+0.14	+0.19	+0.16	+0.29	<b>+0.60</b>	+0.28
	16:1	33.37	+0.29	+0.12	+0.16	+0.16	+0.27	<b>+0.54</b>	+0.27
	32:1	29.94	+0.34	+0.04	+0.10	+0.15	+0.19	<b>+0.39</b>	+0.16
	64:1	27.36	+0.34	+0.00	+0.10	+0.10	+0.14	<b>+0.35</b>	+0.16

Table B.2: PSNR values relative to the corresponding PSNR value of  $D_{4LA}$  for MF images. A positive entry corresponds to PSNR value higher than that of  $D_{4LA}$ . A negative entry corresponds to PSNR value lower than that of  $D_{4LA}$ .

Image	CR	Wavelets							
		$D_{4LA}$	$B_{9/7}$	$D_{5LA}$	$D_{6LA}$	$D_{8LA}$	$D_{9LA}$	$B_{22/14}$	$D_{10LA}$
<i>Barbara</i>	08:1	35.45	+0.00	+0.00	+0.00	<b>+0.02</b>	+0.01	<b>+0.02</b>	+0.00
	16:1	30.51	<b>+0.03</b>	+0.02	<b>+0.03</b>	+0.02	<b>+0.03</b>	+0.01	+0.00
	32:1	27.00	+0.05	+0.00	+0.01	<b>+0.14</b>	+0.11	+0.10	+0.05
	64:1	24.24	+0.06	+0.04	+0.02	+0.03	<b>+0.05</b>	+0.03	+0.03
<i>Lighthouse</i>	08:1	33.26	+0.07	+0.05	+0.03	<b>+0.14</b>	+0.12	+0.10	+0.05
	16:1	29.69	+0.06	+0.05	+0.02	+0.06	<b>+0.07</b>	+0.03	+0.02
	32:1	26.84	+0.12	+0.06	+0.04	<b>+0.19</b>	+0.15	+0.12	+0.07
	64:1	24.32	+0.04	+0.02	+0.02	+0.06	<b>+0.08</b>	+0.05	+0.04
<i>Nitf7</i>	08:1	25.12	+0.15	+0.08	+0.05	<b>+0.20</b>	+0.18	+0.14	+0.10
	16:1	22.04	+0.06	+0.02	+0.03	+0.03	<b>+0.06</b>	+0.04	+0.02
	32:1	19.76	+0.12	+0.03	+0.05	<b>+0.24</b>	+0.22	+0.18	+0.12
	64:1	17.77	+0.08	+0.06	+0.03	+0.06	<b>+0.09</b>	+0.07	+0.03
<i>House</i>	08:1	29.89	+0.11	+0.04	+0.03	<b>+0.21</b>	+0.18	+0.15	+0.09
	16:1	25.24	+0.08	+0.04	+0.02	+0.03	<b>+0.09</b>	+0.06	+0.03
	32:1	22.40	+0.08	+0.08	+0.01	<b>+0.23</b>	+0.10	+0.11	+0.02
	64:1	20.52	+0.18	+0.06	+0.04	<b>+0.32</b>	+0.23	+0.18	+0.10

Table B.3: PSNR values relative to the corresponding PSNR value of  $D_{4LA}$  for HF images. A positive entry corresponds to PSNR value higher than that of  $D_{4LA}$ . A negative entry corresponds to PSNR value lower than that of  $D_{4LA}$ .

Image	CR	Wavelets							
		$D_{4LA}$	$B_{9/7}$	$D_{5LA}$	$D_{6LA}$	$D_{8LA}$	$D_{9LA}$	$B_{22/14}$	$D_{10LA}$
<i>Mandrill</i>	08:1	28.43	+0.09	+0.09	+0.11	+0.14	<b>+0.16</b>	<b>+0.16</b>	<b>+0.16</b>
	16:1	24.88	+0.08	+0.09	+0.10	+0.14	<b>+0.17</b>	+0.16	<b>+0.17</b>
	32:1	22.72	+0.08	+0.05	+0.05	+0.09	+0.11	<b>+0.20</b>	+0.11
	64:1	21.27	+0.09	+0.14	+0.03	+0.15	<b>+0.17</b>	<b>+0.17</b>	+0.13
<i>Satellite</i>	08:1	27.43	+0.03	+0.06	+0.06	+0.07	<b>+0.10</b>	+0.09	+0.09
	16:1	24.77	+0.08	+0.08	+0.07	+0.11	+0.14	<b>+0.17</b>	+0.12
	32:1	23.29	+0.11	+0.08	+0.06	+0.12	+0.12	<b>+0.15</b>	+0.10
	64:1	21.99	+0.08	+0.07	+0.06	+0.08	+0.11	<b>+0.13</b>	+0.11
<i>Grass</i>	08:1	23.12	+0.26	+0.18	+0.25	+0.33	+0.42	<b>+0.48</b>	+0.45
	16:1	20.06	+0.19	+0.13	+0.13	+0.20	+0.26	<b>+0.31</b>	+0.25
	32:1	17.98	+0.12	+0.08	+0.08	+0.11	+0.15	<b>+0.20</b>	+0.13
	64:1	16.46	-0.01	+0.04	+0.02	+0.04	<b>+0.07</b>	+0.05	+0.04
<i>SanDiego</i>	08:1	26.51	+0.21	+0.12	+0.13	+0.18	+0.22	<b>+0.32</b>	+0.18
	16:1	23.34	+0.10	+0.12	+0.11	+0.17	+0.23	<b>+0.24</b>	+0.17
	32:1	21.47	+0.09	+0.08	+0.08	+0.11	<b>+0.17</b>	<b>+0.17</b>	+0.12
	64:1	20.32	+0.04	+0.07	+0.05	+0.10	<b>+0.14</b>	+0.12	+0.09

# Appendix C

## Subjective results for periodic extension



Figure C.1: Original image *Lena* .



Figure C.2: *Lena*, Periodic extension,  $D_{4A}$ , 32:1, PSNR = 32.77 dB.



Figure C.3: *Lena*, Periodic extension,  $D_{4LA}$ , 32:1, PSNR = 32.81 dB.



Figure C.4: *Lena*, Periodic extension,  $D_{10A}$ , 32:1, PSNR = 32.72 dB.



Figure C.5: *Lena*, Periodic extension,  $D_{10LA}$ , 32:1, PSNR = 33.16 dB.



Figure C.6: *Lena*, Periodic extension,  $B_{9/7}$ , 32:1, PSNR = 33.27 dB.



Figure C.7: *Lena*, Periodic extension,  $B_{22/14}$ , 32:1, PSNR = 33.37 dB.



Figure C.8: Original image, *Lighthouse* .



Figure C.9: *Lighthouse*, Periodic extension,  $D_{4A}$ , 32:1, PSNR = 26.62 dB.



Figure C.10: *Lighthouse*, Periodic extension,  $D_{4LA}$ , 32:1, PSNR = 26.62 dB.



Figure C.11: *Lighthouse*, Periodic extension,  $D_{10A}$ , 32:1, PSNR = 26.34 dB.



Figure C.12: *Lighthouse*, Periodic extension,  $D_{10LA}$ , 32:1, PSNR = 26.62 dB.



Figure C.13: *Lighthouse*, Periodic extension,  $B_{9/7}$ , 32:1, PSNR = 26.64 dB.



Figure C.14: *Lighthouse*, Periodic extension,  $B_{22/14}$ , 32:1, PSNR = 26.68 dB.

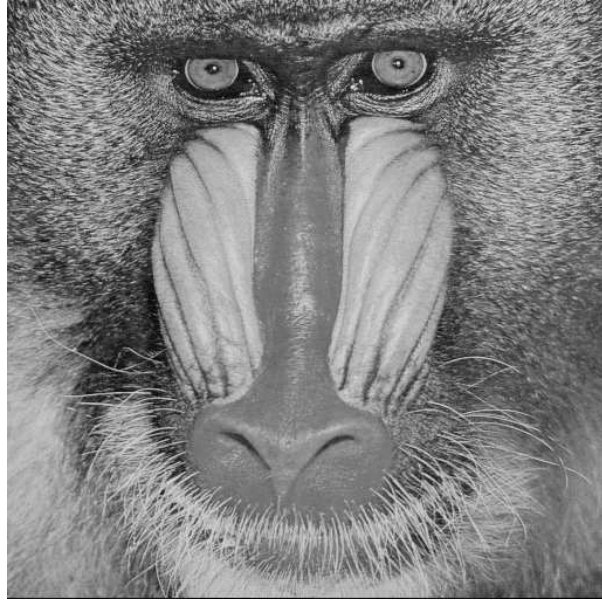


Figure C.15: Original image, *Mandrill* .

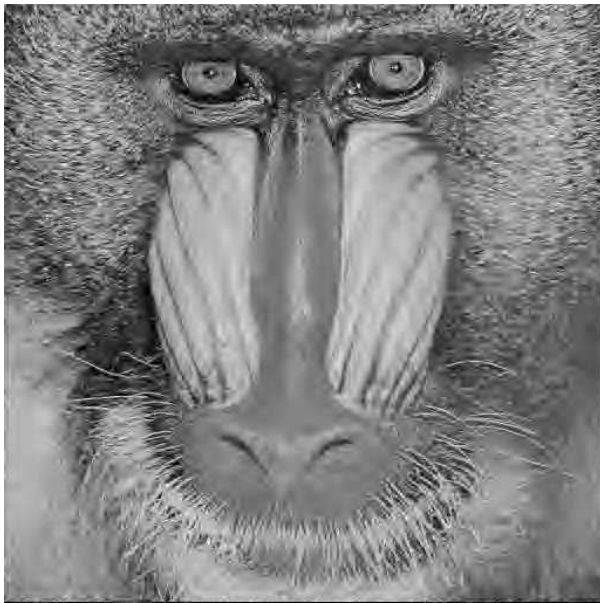


Figure C.16: *Mandrill*, Periodic extension,  $D_{4A}$ , 32:1, PSNR = 22.69 dB.

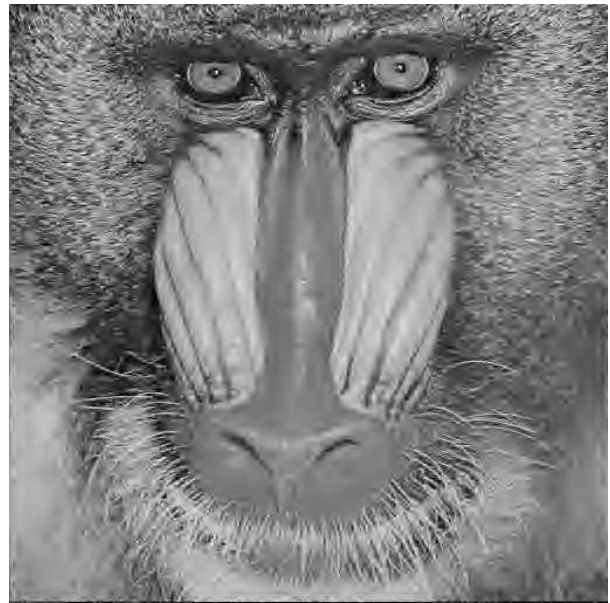


Figure C.17: *Mandrill*, Periodic extension,  $D_{4LA}$ , 32:1, PSNR = 22.70 dB.

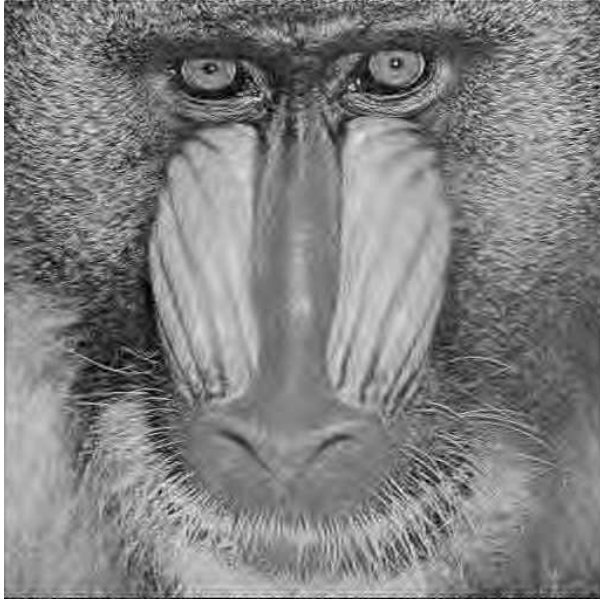


Figure C.18: *Mandrill*, Periodic extension,  $D_{10A}$ , 32:1, PSNR = 22.66 dB.

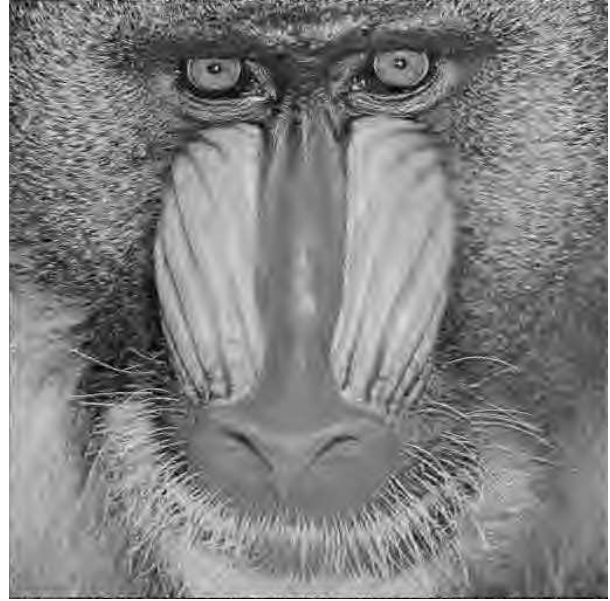


Figure C.19: *Mandrill*, Periodic extension,  $D_{10LA}$ , 32:1, PSNR = 22.80 dB.

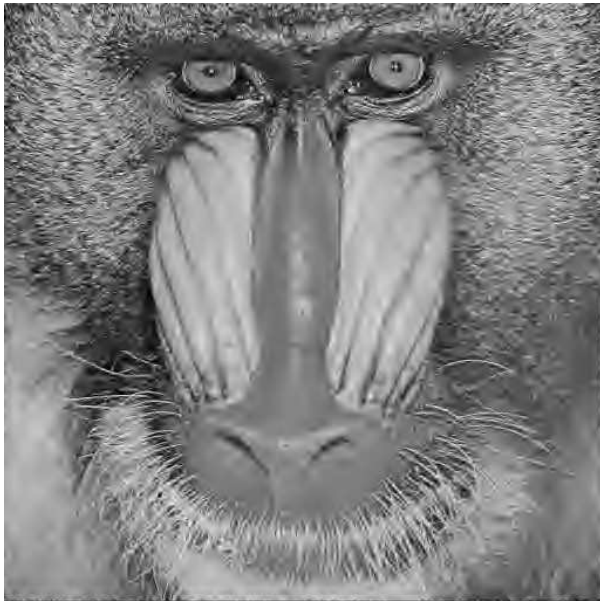


Figure C.20: *Mandrill*, Periodic extension,  $B_{9/7}$ , 32:1, PSNR = 22.77 dB.

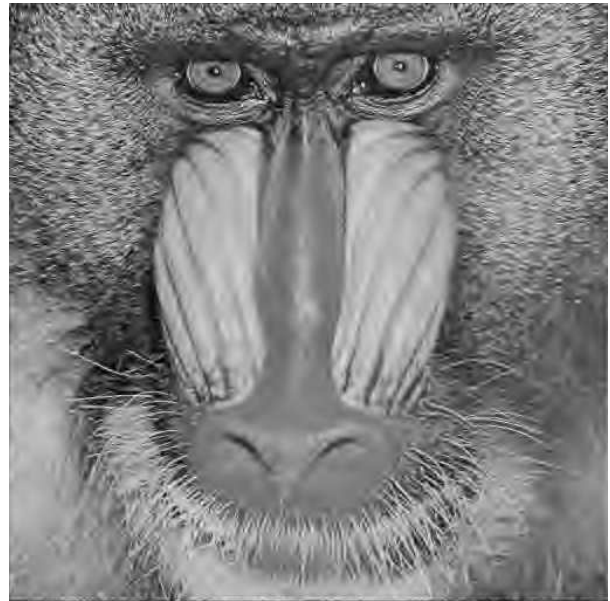


Figure C.21: *Mandrill*, Periodic extension,  $B_{22/14}$ , 32:1, PSNR = 22.86 dB.

# Appendix D

## Subjective results for symmetric extension



Figure D.1: *Lena*, Symmetric extension,  $D_{5LA}$ , 64:1, PSNR = 30.54 dB.



Figure D.2: *Lena*, Symmetric extension,  $B_{9/7}$ , 64:1, PSNR = 30.47 dB.



Figure D.3: *Lena*, Symmetric extension,  $D_{9LA}$ , 64:1, PSNR = 30.60 dB.



Figure D.4: *Lena*, Symmetric extension,  $B_{22/14}$ , 64:1, PSNR = 30.81 dB.



Figure D.5: *Barbara*, Symmetric extension,  $D_{5LA}$ , 64:1, PSNR = 24.29 dB.



Figure D.6: *Barbara*, Symmetric extension,  $B_{9/7}$ , 64:1, PSNR = 24.30 dB.



Figure D.7: *Barbara*, Symmetric extension,  $D_{9LA}$ , 64:1, PSNR = 24.27 dB.



Figure D.8: *Barbara*, Symmetric extension,  $B_{22/14}$ , 64:1, PSNR = 24.29 dB.



Figure D.9: *SanDiego*, Symmetric extension,  $D_{5LA}$ , 32:1, PSNR = 21.55 dB.



Figure D.10: *SanDiego*, Symmetric extension,  $B_{9/7}$ , 32:1, PSNR = 21.56 dB.



Figure D.11: *SanDiego*, Symmetric extension,  $B_{9/7}$ , 32:1, PSNR = 21.64 dB.



Figure D.12: *SanDiego*, Symmetric extension,  $B_{22/14}$ , 32:1, PSNR = 21.64 dB.

# Appendix E

## Test images



Figure E.1: *Lena.*



Figure E.2: *Peppers.*



Figure E.3: *Boat.*



Figure E.4: *Goldhill.*



Figure E.5: *Barbara.*



Figure E.6: *Lighthouse.*



Figure E.7: *House.*



Figure E.8: *Nitf7.*

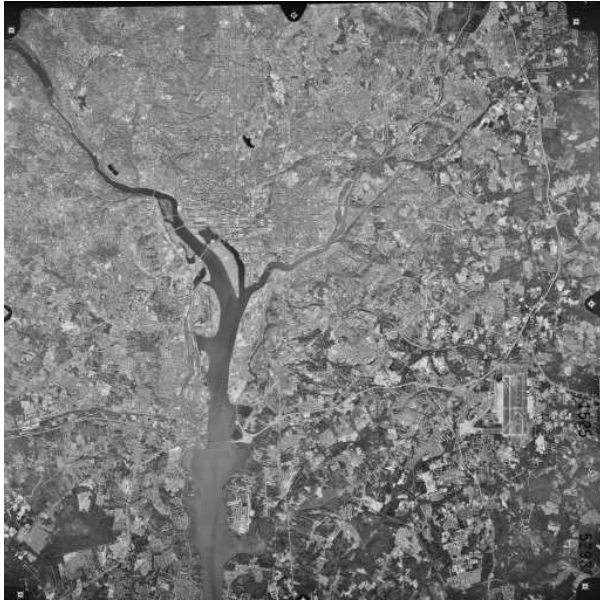


Figure E.9: *Satellite.*

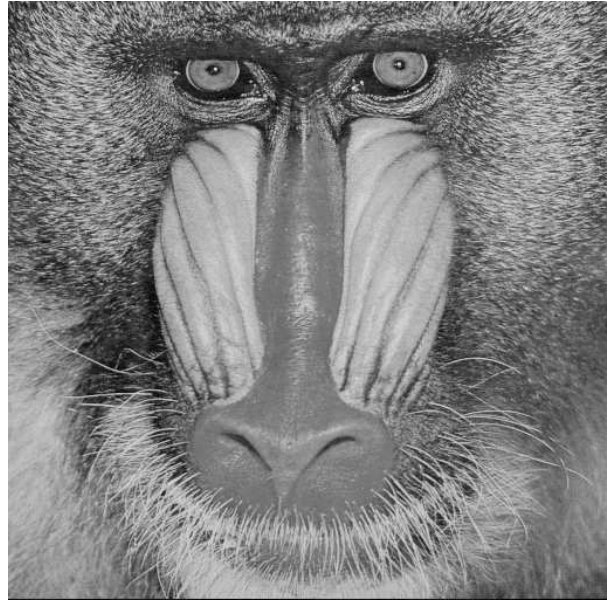


Figure E.10: *Mandrill.*

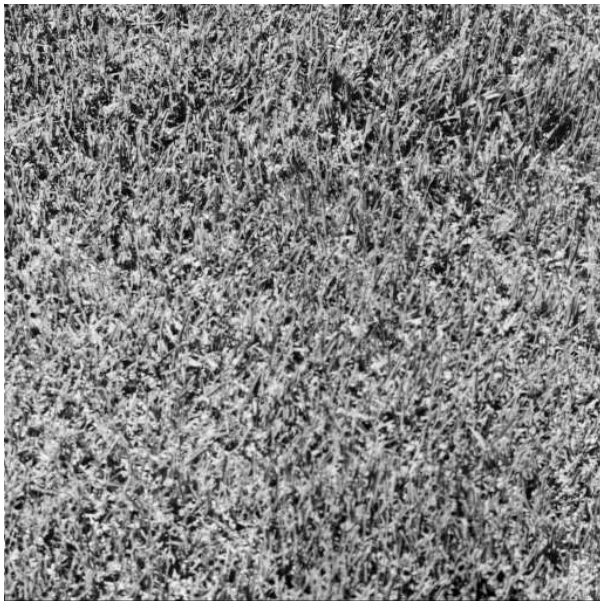


Figure E.11: *Grass.*



Figure E.12: *San Diego.*

# Vita

Satyabrata Rout was born January 1973 in Bhubaneswar, India. He received his Bachelor's degree in Electronics and Telecommunication engineering from the University college of engineering, Sambalpur university in June 1995. After completing his Bachelor's degree he worked as a design engineer for Bharat Heavy Electricals Limited and GE Transportation Systems, Bangalore for a period of four years. His desire for higher education led him to join Virginia Tech in August 2000 to start his graduate study. He worked as a research assistant in Digital signal processing and communication laboratory and Virginia bioinformatics institute during his tenure at Virginia Tech.

His academic interests are in the areas of signal processing, communication and biomedical image processing. He is a sports freak who also loves to cook.